Chern–Simons correlations on (2+1)D lattice

L. A. Abramyan and A. P. Protogenov*[)]

Institute of Applied Physics, Russian Academy of Sciences, 603600 Nizhniĭ Novgorod, Russia

V. A. Verbus

Institute for Physics of Microstructures, Russian Academy of Sciences, 603600 Nizhniĭ Novgorod, Russia

The contribution of zero modes to the value of the number of particles in a discrete model of the $(2+1)$-dimensional nonlinear Schrödinger equation is computed. It is shown for the first time that in the region of small values of the Chern–Simons coefficient k there exists a universal attraction between field configurations. For $k=2$ this phenomenon may be a dynamic origin of the semion pairing in the high-temperature superconducting state of planar systems. The preliminary results of this paper were presented in the proceedings of the XI International Conference on Problems of Quantum Field Theory (Dubna, 13–17 July 1998). © *1999 American Institute of Physics.*
[S0021-3640(99)00112-7]

Cooperative behavior based on universal topological features of planar systems has been the subject of a number of papers.[1,2] The topological properties of $(2+1)$-dimensional (D) systems are described by a Chern–Simons (CS) term in the Lagrangian of the model. This term displays the phenomenon of the chiral invariance violation in such systems. The magnetic CS field usually[3–8] leads to an effective repulsion between field configurations. This property was described in detail in Refs. 9 and 10, where the structure of zero modes in continuous[9] and spatially discrete[10] models of the $(2+1)$D nonlinear Schrödinger equation was studied. The competition of the basic nonlinearity corresponding to attraction, diffraction, and the additional nonlinearity describing the repulsion caused by the CS interaction resulted in an increase of the critical value of the number of particles N in the region of small values of the coefficient k. This increase of N represents the existence of additional repulsion.

We argue in this paper that on the $(2+1)$D lattice there is universal attraction due to CS correlations between field configurations, and we show the conditions under which this phenomenon takes place. We shall show that consideration of the complete contribution of the statistical CS fields in the form of holonomies causes additional (to the bare) attraction at small numbers of links k. The necessary condition for that is naturally the existence of bare attraction between field configurations. This result is the first indication

that there exists a universal attraction due to CS correlation. A comparison with the results of our previous papers[9,10] shows that the condition for obtaining the attraction is that the Wilson and Polyakov exponents be included in the consideration on an equal footing. In other words, we consider a model which takes into account the conditions of compactness for the temporal component of the gauge potential as well as for its spatial component. The gauge invariance requirements imply immediately that discrete evolution should be considered (for detail see Ref. 10). We want to emphasize that the gauged discrete $(2+1)$D nonlinear Schrödinger equation gives us a convenient tool to display this $(2+1)$D system phenomenon of additional attraction, which has a general and universal character.

The equation of motion in the model of the gauged discrete $(2+1)$D nonlinear Schrödinger equation has the form

$$(\hat{t}_x+\hat{t}_y+\text{h.c.}-4)\rho_{m,n}=-2C\rho_{m,n}^3-\rho_{m,n}\sin(w_{m,n}-1),\tag{1}$$

$$\hat{t}_x\rho_{m,n}\equiv e^{iA_{\hat{m},n}}\rho_{m+1,n}.$$

Here $\hat{t}_x$ is the operator of so-called magnetic translations. The parameter $C=g|k|$ in Eq. (1) contains the coupling constant g of the classical nonlinear Schrödinger equation and CS coefficient k. Besides the consideration of the model on a 2D lattice[10] we included the discrete time $t\in\mathbb{Z}$ in the description. This leads for the stationary states $\Psi(m,n,t)=\rho_{m,n}e^{it}$ to the existence of nonlinearity expressed by the sine function in Eq. (1). The multiconnection of the 2D manifold has been taken into account by the gauge field $A^\mu(m,n)=(w_{m,n},A_{\hat{m},n},A_{m,\hat{n}})$, where

$$w_{m,n}=\sum_{m',n'}[(\Delta_2 G(m-m',n-n'))(\rho_{m',n'}^2+\rho_{m',n'+1}^2)A_{m',\hat{n}'}$$
$$-(\Delta_1 G(m-m',n-n'))(\rho_{m',n'}^2+\rho_{m'+1,n'}^2)A_{\hat{m}',n'}]\tag{2}$$

is the temporal component of the CS potential, and

$$A_{\hat{m},n}=\sum_{m',n'}\Delta_2 G(m-m',n-n')\rho_{m',n'}^2\tag{3}$$

is the x component of the vector potential. The notation $A_{\hat{m},n}$ denotes that the components $A_x(m,n)$ are defined on the links connecting the sites $(m,n),(m+1,n)$. In Eqs. (2) and (3) $\Delta_{1,2}f(\mathbf{r})\equiv f(\mathbf{r}+\mathbf{e}_{1,2})-f(\mathbf{r})$ is the gradient on the lattice with coordinates $\mathbf{r}=(m,n)\in\mathbb{Z}^2$; $\mathbf{e}_i$ is the unit vector. The Green function on the lattice in Eqs. (2) and (3) has the form:

$$G(m-m',n-n')=\int_{-\pi}^{\pi}\frac{d^2k}{(2\pi)^2}\frac{e^{i\{k_x(m-m')+k_y(n-n')\}}-1}{4-2\cos k_x-2\cos k_y}.\tag{4}$$

The main purpose of this paper is to study the dependence of the critical number of particles $N=\Sigma_{m',n'}\rho_{m',n'}^2$ on the parameter $C=g|k|$, considering the arbitrarily large contribution of the temporal component of the gauge potential as well as of its spatial component. To solve the problem we compute this dependence using the zero modes found for various values of the CS coefficient k.
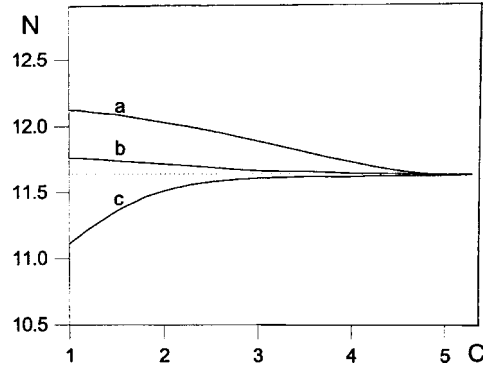
FIG. 1. Dependence of the critical number of the particles on the parameter C for the three types of the nonlinearity in Eq. (1) (see for details the text). The dashed line shows the value $N^{\text{lat}}(A_\mu=0)=11.605$.

We performed the simulation of the problem (1)–(4) on a lattice with linear size $L\leqslant 20$ using the method of the stabilizing Petviashvili multiplier.[11] The block diagram of the method and the details of the calculations are described in Refs. 9 and 10. In accordance with the rules of gauge field theory on a lattice, we assumed that while the gauge field is defined on the lattice links, the curl of the field $A_\mu(\mathbf{r})$ and the density ρ^2 are defined on the sites of the dual lattice.

We used the function $\rho_{m,n}$ for calculation of the $N(C)$ curves shown in Fig. 1. The form of the functions $\rho_{m,n}, A_{\hat{m},n}, w_{m,n}$ found numerically is displayed in Ref. 10. The form of these functions in the present paper is qualitatively the same. Note that the limit $k\to\infty$ is equivalent to the zero contribution of the gauge fields $\mathbf{A}_{m,n}, w_{m,n}$, when in the continuous limit $N_{\text{cr}}=11.703$. This number of particles separates the regime of 2D collapse at $N>N_{\text{cr}}$ and its absence at $N<N_{\text{cr}}$. On a lattice the values $N_{\text{cr}}^{\text{lat}}$ are always less[12] than the critical number of particles in the continuous limit even if the CS fields are neglected. Therefore the main problem of interest is whether $N_{\text{cr}}^{\text{lat}}(A_\mu\neq 0)$ is smaller than or greater than $N_{\text{cr}}^{\text{lat}}(A_\mu=0)$ if the CS gauge fields are taken into account.

Curve a in Fig. 1 shows the result of Ref. 10 when we considered only the part $4-2\cos A_x-2\cos A_y$ of the contribution to Eq. (1) of the spatial gauge field components and did not consider the discrete time. Case b in Fig. 1 corresponds to complete consideration of the spatial gauge field contribution to the left-hand side of Eq. (1) with the same properties of the time as above. The $N(C)$ curve for case c in Fig. 1 presents the result of computations on the $(2+1)$D lattice, with consideration of the complete contribution of all (arbitrarily large) gauge field components A_μ and with the discrete time taken into account.

From the $N(C)$ curve for case c in Fig. 1 one can infer that the decrease of the critical number of particles N with decreasing parameter C is equivalent to an increase of the attraction in comparison with the case when the contribution of the CS fields is not taken into account.

It is known[1,2] that in CS systems there arises an induced angular momentum proportional to $1/k$. The calculated lines of equal value of the field $\rho_{m,n}$ for $C=1$ are shown in Fig. 2. Here we would like to call attention to the fact that the field $\rho_{m,n}$ has
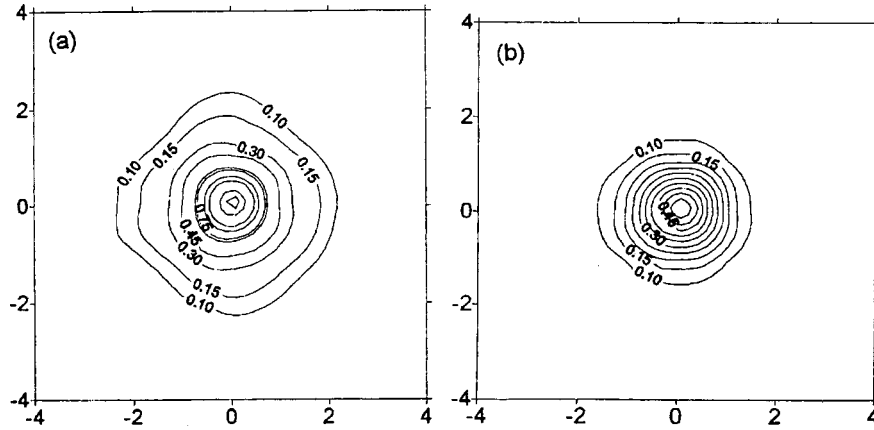
FIG. 2. Lines of equal value of the field $\rho_{m,n}$ for $C=1$ (a) and $C=5$ (b).

d symmetry for a small value of the parameter $C=1$ at great distances from the origin. We found weak display of this phenomenon (see Fig. 2). The accuracy of the calculations, according to our estimates, is several percent. A comparison of the results in Fig. 2 for the different values of the parameter C shows that the display of d-wave symmetry increases with decrease of parameter C.

The origin of the phenomena under discussion is as follows. We consider the nonlinear, nonlocal dependence of the components $A_\mu(m,n)$ of the CS gauge field via the field $\rho_{m,n}$ in its complete form presented in Eq. (1) for the Laplacian. In particular, if we extract[10] a part of this contribution to nonlinearity, specifically taking into account the compact version $\rho(4-2\cos A_x - 2\cos A_y)$ of the nonlinearity $\rho(A_x^2 + A_y^2)$ (Ref. 9), the remaining part of the discrete Laplacian in the continuous limit has the form

$$\cos A_x \frac{\partial^2}{\partial x^2} + \cos A_y \frac{\partial^2}{\partial y^2}.$$

The decrease of the coefficients in this expression in comparison with the value $A_{m,n} = 1$ in the region of small coefficients k leads to a decrease of diffraction. It is seen that the origin of the additional attraction due to the CS fields is a decrease of the diffraction. If this this effect is neglected, we observe[10] only repulsion due to the CS fields. The anisotropy of this operator is the reason for the d symmetry of the ground state.

As was pointed out above, the phenomenon under consideration exists on a lattice under the condition that the gauge field is completely taken into account by the holonomies e^{iA_μ}. The physical interpretation is clear: because the zero component of the gauge potential plays the role of the chemical potential, an arbitrarily large value of the one corresponds to an arbitrarily large value of the energy added to the system when we add a particle.

Note that discrete models are characterized by features which are absent in the continuous limit. In particular, localized states can exist in the $(1+1)$D discrete nonlinear Schrödinger equation.[13] In our case the dimensionality of the problem as well as the discrete character of the space and the time are important. Using the arguments in inverse

order, we have to include discrete space and time in the model on an equal footing in order to consider the large magnitude of the gauge field in the form of the Wilson exponent as well as the Polyakov exponent, having in mind the gauge invariance. Our simulation shows, for example, that without the condition of the discretization of the time we cannot obtain the attraction due to the CS fields.

Finally, we should like to make a general remark. The attraction between particles in the systems with the CS interaction has been a subject of extensive studies during the last ten years. Attention has focused[14-16] on analyzing the symmetry of the state (*s*-, *p*- or *d*-wave states) with a nonzero value of the superconducting gap in the framework of perturbation theory when the parameter $\alpha = 4\pi/|k|$ is small, i.e., in the limit $|k| \gg 1$. The discovery[17] of the time-reversal symmetry-breaking *p*-wave superconductivity in Sr_2RuO_4 (see also Refs.18–20) stimulated a recent paper[21] in which a search for the induced CS term in *P*- and *T*-violating superconductors was performed.

The picture of the Chern–Simons correlations in the present paper in some sense goes beyond the above-mentioned approaches. We have found the attraction due to the CS gauge field in the essentially nonperturbative region of *small* values of the coefficient k, irrespectively of the symmetry of the ground state. In other words, this phenomenon takes place for *d*-wave as well as for *p*-wave field configurations. Another distinction from the above-mentioned papers is that the choice of the coefficient k itself determines the symmetry of the state considered. In this respect, Fig. 2 presents only one of the possible ground-state symmetries characterized by the specific value of the parameter C.

Let us suppose that $C = 0$ in Eq. (1). We obtain in this case a model describing the nonlocal interaction of CS vortices. This case corresponds in the continuous limit to universal nonlinearity of the ρ^5 kind and differs from the Gross–Pitaevskii model,[22] where the nonlinearity in the equation of motion is a local one and is proportional to ρ^3. We plan to study this interesting limit in a separate paper.

In conclusion, we have studied the dependence of the critical particle number on the link numbers of the field configurations. Using the model of the discrete $(2+1)$D nonlinear Schrödinger equation, we have found for the first time the existence of attraction due to the CS fields. We have shown that the origin of this phenomenon is the suppression of free propagation by the CS fields at small link numbers. Note that for $g = 1$ the semion value $k = 2$, which is of topical interest, lies inside this region. Therefore the attraction found may be a dynamic cause of the semion pairing and phase transition to a superconducting state.

*)e-mail: alprot@appl.sci-nnov.ru

[1] F. Wilczek (Ed.), *Fractional Statistics and Anyon Superconductivity*, World Scientific, Singapore, 1990.
[2] A. P. Protogenov, Usp. Fiz. Nauk **162**, 1 (1992) [Sov. Phys. Usp. **35**, 535 (1992)].
[3] R. Jackiw and S. Y. Pi, Phys. Rev. Lett. **64**, 2969 (1990); C **66**, 2682 (1991); Phys. Rev. D **42**, 3500 (1990); Prog. Theor. Phys. Suppl. **107**, 1 (1992).
[4] J. Hong, Y. Kim, and P. Y. Pac, Phys. Rev. Lett. **64**, 2230 (1990).

[5] R. Jackiw and E. Weinberg, Phys. Rev. Lett. **64**, 2234 (1990); R. Jackiw, K. Lee, and E. Weinberg, Phys. Rev. D **42**, 3488 (1990).

[6] I. V. Barashenkov and A. O. Harin, Phys. Rev. Lett. **72**, 1575 (1994); Phys. Rev. D **52**, 2471 (1995).

[7] L. Bergé, A. de Bouard, and J. C. Saut, Phys. Rev. Lett. **74**, 3907 (1995).

[8] M. Knecht, R. Pasquier, and J. Y. Pasquier, J. Math. Phys. **36**, 4181 (1995).

[9] L. A. Abramyan, V. I. Berezhiani, and A. P. Protogenov, Phys. Rev. E **56**, 6026 (1997).

[10] L. A. Abramyan, A. P. Protogenov, and V. A. Verbus, Zh. Eksp. Teor. Fiz. **114**, 747 (1998) [JETP **87**, 408 (1998)].

[11] V. I. Petviashvili, Fiz. Plazmy **2**, 469 (1976) [Sov. J. Plasma Phys. **2**, 257 (1976)].

[12] E. W. Laedke, K. H. Spatschek, V. K. Mezentsev *et al.*, JETP Lett. **62**, 677 (1995).

[13] D. Cai, A. R. Bishop, and N. Grønbech-Jensen, Phys. Rev. Lett. **72**, 591 (1994).

[14] Ya. I. Kogan, JETP Lett. **49**, 225 (1989).

[15] Ya. I. Kogan and I. V. Polubin, JETP Lett. **51**, 560 (1990).

[16] Ya. I. Kogan and D. V. Khveshchenko, JETP Lett. **50**, 152 (1989); D. V. Khveshchenko and Ya. I. Kogan, Mod. Phys. Lett. B **4**, 95 (1990).

[17] G. M. Luke *et al.*, Nature (London) **394**, 558 (1998).

[18] K. Krishana *et al.*, Science **277**, 83 (1997).

[19] R. B. Laughlin, Phys. Rev. Lett. **80**, 5188 (1998).

[20] G. E. Volovik, JETP Lett. **66**, 522 (1997).

[21] J. Goryo and K. Ishikawa, http://xxx.lanl.gov/abs/cond-mat/9812412.

[22] L. D. Landau and E. M. Lifshitz, *Statistical Physics*, 3rd ed., rev. and enl., with L. P. Pitaevskii, Vol. 2 (by E. M. Lifshitz and L. P. Pitaevskii), Pergamon Press, Oxford, 1980 [Russ. original, Vol. 2, Nauka, Moscow, 1978, p. 145].

Current tensor with heavy photon for double hard photon emission by a longitudinally polarized electron

M. Konchatnij and N. P. Merenkov

Kharkov Institute of Physics and Technology National Science Center, 310108 Kharkov, Ukraine

The electron current tensor for the scattering of a heavy photon on a longitudinally polarized electron with the emission of two hard real photons is considered. The contributions of collinear and semicollinear kinematics are computed. The result allows one to calculate the corresponding contribution to the second-order radiative correction to the deep inelastic scattering or electron–positron annihilation cross sections with next-to-leading-order accuracy. © *1999 American Institute of Physics.* [S0021-3640(99)00212-1]

PACS numbers: 12.20.Ds, 13.40.Ks

1. The recent polarized experiments on deep inelastic scattering (DIS)[1,2] cover the kinematical region $y \simeq 0.9$, where the electromagnetic corrections to the cross section are extremely large. The first-order QED correction has been computed in Refs. 3 and 4, and it is of the order of the Born cross section in this region. For this reason the calculation of the second-order QED correction has become very important for interpretation of these experiments. The first step in such calculation was made in Ref. 5, where the one-loop-corrected Compton tensor with a heavy photon was considered. That is one of the contributions to the polarized electron current tensor which appear in the second order of perturbation theory. Other contributions arise due to double hard photon emission and pair production.

Here we calculate the contribution to the polarized electron current tensor from the emission of two hard photons. We investigate the double collinear and semicollinear kinematics. This allows us to compute the corresponding second-order radiative correction to various observables with next-to-leading-order accuracy, in the same manner as has been done, for example, for small-angle Bhabha scattering,[6] tagged photon cross sections in DIS,[7] and electron–positron annihilation[8] in the unpolarized case.

In the Born approximation the electron current tensor for a longitudinally polarized electron has the form

$$L^B_{\mu\nu} = Q_{\mu\nu} + i\lambda E_{\mu\nu}, \quad Q_{\mu\nu} = -4(p_1 p_2)g_{\mu\nu} + 4p_{1\mu}p_{2\nu} + 4p_{1\nu}p_{2\mu},$$

$$E_{\mu\nu} = 4\epsilon_{\mu\nu\rho\sigma}p_{1\rho}p_{2\sigma}, \tag{1}$$

where $p_1(p_2)$ is the 4-momentum of the initial (final) electron, and $\lambda = 1(-1)$ if the initial electron is polarized along (against) its 3-momentum direction.

In the case of single collinear photon emission the corresponding contribution to the electron current tensor conserves the Born structure for radiation along the scattered electron momentum direction,

$$L_{\mu\nu}^{(1)f} = \frac{\alpha}{2\pi}\left[\frac{1+(1+y)^2}{y}\tilde{L}_0 - \frac{2(1+y)}{y}\right]dyL_{\mu\nu}^B, \quad y = \frac{\omega}{\varepsilon_2}, \quad \tilde{L}_0 = \ln\frac{\varepsilon_2^2\theta_0^2}{m^2}, \tag{2}$$

and acquires an additional part (which is proportional to $i\lambda E\mu\nu$) for radiation along the initial electron momentum direction,[9]

$$L_{\mu\nu}^{(1)i} = \frac{\alpha}{2\pi}\left\{\left[\frac{1+(1-x)^2}{x}L_0 - \frac{2(1-x)}{x}\right]L_{\mu\nu}^B - 2xi\lambda E_{\mu\nu}\right\}dx, \quad x = \frac{\omega}{\varepsilon_1},$$

$$L_0 = \ln\frac{\varepsilon_1^2\theta_0^2}{m^2}. \tag{3}$$

In Eqs. (2) and (3) ω is the photon energy, $\varepsilon_1(\varepsilon_2)$ is the energy of the initial (final) electron, m is the electron mass, and the parameter θ_0 defines the angular phase space of the hard collinear photon. The index $i(f)$ labels the initial (final) electron state.

Looking at Eq. (3), we see that the additional part does not contribute in the leading logarithmic approximation and does not have infrared divergence. In other words, the Born structure of the electron current tensor in the case of a longitudinally polarized electron is disturbed only in the next-to-leading approximation due to radiation by the initial polarized electron itself.

In general, the contribution to the current tensor $L_{\mu\nu}$ due to the emission of n collinear photons can be written as follows:

$$L_{\mu\nu}^{(n)} = \left(\frac{\alpha}{2\pi^2}\right)^n\left[I^{(n)}L_{\mu\nu}^B + K^{(n)}i\lambda E_{\mu\nu}\right]\prod_{i=1}^{n}\frac{d^3k_i}{\omega_i}, \tag{4}$$

where the quantity $K^{(n)}$ equals zero if (and only if) all n collinear photons are emitted along the scattered (unpolarized) electron momentum direction. The first term in the right-hand side of Eq. (4) was obtained in Ref. 10 with next-to-leading-order accuracy. Our goal is to find the second term with the same accuracy.

2. We use the covariant method of calculation and start from the general expression for the polarized current tensor which arises due the emission of two hard photons,

$$L_{\mu\nu}^{(2)} = \left(\frac{\alpha}{4\pi^2}\right)^2\frac{d^3k_1d^3k_2}{\omega_1\omega_2}Sp(\hat{p}_2+m)Q_\mu^{\lambda\rho}(\hat{p}_1+m)(1-\gamma_5\hat{P})(Q_\nu^{\lambda\rho})^+, \tag{5}$$

where P is the polarization 4-vector of initial electron. The quantity $Q_\mu^{\lambda\rho}$ reads

$$Q_\mu^{\lambda\rho} = \gamma_\mu \frac{\hat{\Delta}+m}{\Delta^2-m^2}\gamma_\rho \frac{\hat{p}_1-\hat{k}_1+m}{-2p_1k_1}\gamma_\lambda + \gamma_\rho \frac{\hat{p}_2+\hat{k}_2+m}{2p_2k_2}\gamma_\mu \frac{\hat{p}_1-\hat{k}_1+m}{-2p_1k_1}\gamma_\lambda$$

$$+ \gamma_\rho \frac{\hat{p}_2+\hat{k}_2+m}{2p_2k_2}\gamma_\lambda \frac{\hat{\Sigma}+m}{\Sigma^2-m^2}\gamma_\mu + (1\leftrightarrow 2), \quad \Delta = p_1-k_1-k_2, \quad \Sigma = p_2+k_1+k_2.$$

(6)

For the important case of a longitudinally polarized electron the polarization vector can be written, in the framework of the adopted accuracy, as

$$P = \frac{\lambda}{m}\left(p_1 - \frac{m^2k}{p_1k}\right),$$

(7)

where λ is the doubled electron helicity, and the 4-vector k has the components $(\varepsilon_1, -\mathbf{p}_1)$, $k^2=m^2$. It is easy to see that

$$P^2 = -1 + O(m^4/\varepsilon^4), \quad Pp_1 = 0.$$

Note that for calculations in the leading approximation we can neglect the second term in the right-hand side of Eq. (7), as was done in Ref. 5.

There are four collinear regions in the case of double photon emission: $(\mathbf{k}_1,\mathbf{k}_2\|\mathbf{p}_1)$; $(\mathbf{k}_1,\mathbf{k}_2\|\mathbf{p}_2)$; $(\mathbf{k}_1\|\mathbf{p}_1, \mathbf{k}_2\|\mathbf{p}_2)$ and $(\mathbf{k}_1\|\mathbf{p}_2, \mathbf{k}_2\|\mathbf{p}_1)$. A straightforward calculation in the region $(\mathbf{k}_1,\mathbf{k}_2\|\mathbf{p}_1)$, when both hard collinear photons are emitted by the initial-state polarized electron, gives

$$\frac{m^4}{4}I_{ii}^{(2)} = \frac{1+y^2}{2x_1x_2\eta_1\eta_2} + \frac{1}{d\eta_1}\left[-(1-x_2)+2y\left(1-\frac{x_1}{x_2}\right) + \frac{1-x_1}{x_1x_2}((1-y)(x_1-x_2)-2y)\right]$$

$$- \frac{y\eta_2}{d^2\eta_1} + \frac{2}{d\eta_1^2}\left(x_2 + \frac{2y(1-x_1)}{x_2}\right) - \frac{4y}{d^2\eta_1} + \frac{(1-y)(2y+x_1x_2)}{x_1x_2d\eta_1\eta_2}$$

$$+ \frac{4y}{d^2\eta_1}\left(\frac{1}{\eta_1} + \frac{1}{\eta_2}\right) + (1\leftrightarrow 2),$$

(8)

$$\frac{m^4}{4}K_{ii}^{(2)} = \frac{2}{d\eta_1^2}\left(1-x_2-x_1x_2 + \frac{2yx_1^2}{x_2}\right) + \frac{1}{d\eta_1\eta_2}\left(3-3y+2y^2 + \frac{4x_2^2}{x_1}\right)$$

$$+ \frac{2}{d^2\eta_1}(3y-x_1^2-x_2^2) + \frac{2y\eta_2}{d^2\eta_1^2} + \frac{4}{d^2\eta_1}\left(\frac{1}{\eta_1} + \frac{1}{\eta_2}\right)[(1-y)^2 - x_1x_2]$$

$$+ (1\leftrightarrow 2), \quad y = 1-x_1-x_2.$$

(9)

In writing Eqs. (8) and (9) we have used the following notation:

$$2p_1k_{1,2} = m^2\eta_{1,2}, \quad \Delta^2-m^2 = m^2d, \quad x_{1,2} = \omega_{1,2}/\varepsilon_1.$$

In the region $(\mathbf{k}_1,\mathbf{k}_2\|\mathbf{p}_2)$, when both hard collinear photons are emitted by the final-state unpolarized electron, we have

$$K_{ff}^{(2)} = 0, \quad I_{ff}^{(2)} = I_{ii}^{(2)}(x_{1,2}\to -y_{1,2}, \quad \eta_{1,2}\to -\sigma_{1,2}, \quad d\to\sigma, \quad \to\eta = 1+y_1+y_2),$$

(10)

where

$$y_{1,2} = \omega_{1,2}/\varepsilon_2, \quad 2p_2 k_{1,2} = m^2 \sigma_{1,2}, \quad \Sigma^2 - m^2 = m^2 \sigma.$$

In accordance with the quasireal electron method[9] we can express the electron current tensor in the region $(\mathbf{k}_1 \| \mathbf{p}_1, \mathbf{k}_2 \| \mathbf{p}_2)$ as a product of the probability of radiation of a collinear photon with energy ω_2 by the scattered electron (which is the coefficient multiplying $L^B_{\mu\nu}$ in the right-hand side of Eq. (2) with $y = y_2$) and the electron current tensor due to single photon emission by the initial electron, as given by Eq. (3) with $x = x_1$. Therefore the contribution of the regions $(\mathbf{k}_1 \| \mathbf{p}_1, \mathbf{k}_2 \| \mathbf{p}_2)$ and $(\mathbf{k}_2 \| \mathbf{p}_1, \mathbf{k}_1 \| \mathbf{p}_2)$ reads

$$L^{(2)if}_{\mu\nu} = \left(\frac{\alpha}{2\pi}\right)^2 \left[\frac{1+(1+y_2)^2}{y_2}\tilde{L}_0 - \frac{2(1+y_2)}{y_2}\right] \left\{\left[\frac{1+(1-x_1)^2}{x_1}L_0 - \frac{2(1-x_1)}{x_1}\right]\right.$$

$$\left. \times L^B_{\mu\nu} - 2x_1 i\lambda E_{\mu\nu}\right\} dy_2 dx_1 + (1\leftrightarrow 2). \tag{11}$$

In order to derive the corresponding contributions in the regions $(\mathbf{k}_1, \mathbf{k}_2 \| \mathbf{p}_1)$ and $(\mathbf{k}_1, \mathbf{k}_2 \| \mathbf{p}_2)$ we have to perform the angular integration in Eq. (4) using Eqs. (8) and (9). Moreover, we can also integrate over the energy fraction $x_1(y_1)$ in the region $(\mathbf{k}_1, \mathbf{k}_2 \| \mathbf{p}_1)$ $((\mathbf{k}_1, \mathbf{k}_2 \| \mathbf{p}_2))$ at a fixed value of the quantity $x_1 + x_2 = 1 - y(y_1 + y_2 = \eta - 1)$, because the 4-momentum of the heavy photon, which interacts with the hadronic part of the amplitude, depends on $1 - y(\eta - 1)$ in this case.

The expressions (8) and (9) for $I^{(2)}_{ii}$ and $K^{(2)}_{ii}$ are suitable for calculations with a power-law accuracy (up to terms of order m^2/ε_1^2). But here we restrict ourselves to logarithmic accuracy and can therefore omit terms proportional to $1/d\,\eta_1\eta_2, 1/d^2\,\eta_1, 1/d^2\,\eta_1^2$, and $1/d^2\,\eta_1\eta_2$ in the right-hand sides of Eqs. (8) and (9). In this approximation the integration of $I^{(2)}_{ii}$ leads to (see Ref. 10)

$$\int \frac{d^3k_1 d^3k_2}{\omega_1\omega_2} \frac{I^{(2)}_{ii}}{m^4} = \pi^2 \left[\frac{1}{2}L_0^2 A(y,\delta) + L_0 B(y,\delta)\right] dy, \tag{12}$$

$$A = 4\frac{1+y^2}{1-y}\ln\frac{1-y-\delta}{\delta} + (1+y)\ln y - 2(1-y), \tag{13}$$

$$B = 3(1-y) + \frac{3+y^2}{2(1-y)}\ln^2 y - \frac{2(1+y)^2}{1-y}\ln\frac{1-y-\delta}{\delta}, \tag{14}$$

where $\delta \ll 1$ is the infrared cutoff for the energy fraction of each photon. Analogously, the integration of $K^{(2)}_{ii}$ reads

$$\int \frac{d^3k_1 d^3k_2}{\omega_1\omega_2} \frac{K^{(2)}_{ii}}{m^4} = \pi^2 L_0 C(y,\delta) dy, \quad C = 2(1-y)\left[2 - \ln y - 2\ln\frac{1-y}{\delta}\right] dy. \tag{15}$$

Using Eqs. (12) and (15) together with Eq. (4), we obtain

$$L^{(2)ii}_{\mu\nu} = \left(\frac{\alpha}{2\pi}\right)^2 \left[\left(\frac{1}{2}L_0^2 A(y,\delta) + L_0 B(y,\delta)\right)L^B_{\mu\nu} + C(y,\delta)L_0 i\lambda E_{\mu\nu}\right] dy \tag{16}$$

for the contribution of the region $(\mathbf{k}_1, \mathbf{k}_2 \| \vec{p}_1)$ to the current tensor of the longitudinally polarized electron. In some applications the quantity y remains fixed (for example, for calculation of the tagged photon cross sections). In this case we can write $\ln((1-y)/\delta)$ instead of $\ln((1-y-\delta)/\delta)$ in the expressions for A and B.

The corresponding contribution of the region $(\mathbf{k}_1, \mathbf{k}_2 \| \mathbf{p}_2)$ can be written as follows:

$$L_{\mu\nu}^{(2)ff} = \left(\frac{\alpha}{2\pi}\right)^2 \left[\frac{1}{2}\tilde{L}_0^2 \tilde{A}(\eta, \delta') + \tilde{L}_0 \tilde{B}(\eta, \delta')\right] L_{\mu\nu}^B d\eta, \quad \delta' = \frac{\delta\varepsilon_1}{\varepsilon_2}, \tag{17}$$

where

$$\tilde{A} = 4\frac{1+\eta^2}{\eta-1}\ln\frac{\eta-1-\delta'}{\delta'} - (1+\eta)\ln\eta - 2(\eta-1), \tag{18}$$

$$\tilde{B} = 3(\eta-1) + \frac{3+\eta^2}{2(\eta-1)}\ln^2\eta - 2\frac{(1+\eta)^2}{\eta-1}\ln\frac{\eta-1-\delta'}{\delta'}. \tag{19}$$

Note that the quantities $\tilde{A}$ and $\tilde{B}$ can be reconstructed from the quantities A and B by the rule

$$\tilde{A}(\eta, \delta') = -A(\eta, -\delta'), \quad \tilde{B}(\eta, \delta') = -B(\eta, -\delta').$$

As we saw above [Eq. (3)], the additional part to the Born structure of the polarized electron current tensor due to single collinear photon emission has neither collinear (does not contain a large logarithm) nor infrared (is finite in the limit $x \to 0$) singularities. These singularities do appear, however, in the corresponding contribution due to double collinear photon emission [Eqs. (11) and (16)]. Nevertheless, the additional part never contributes in the leading approximation.

The infrared parameter δ must cancel out in any physical application if the photons are unobserved. Such cancellation takes place because of contributions due to double virtual and soft photon emission as well as virtual and soft corrections to the single hard photon emission. The last contributions have been considered recently[5] within the approximation $m^2 = 0$, which describes large-angle photon radiation. If we put $m^2 = 0$ in our calculations, then we will be left with only the Born-like structure in Eqs. (3), (11), and (16). Moreover, the quantities B and $\tilde{B}$ in Eqs. (16) and (17) will be changed in this approximation. Consequently, we see that the electron mass must be kept finite in order to be correct in the next-to-leading approximation in any physical application with unobserved photons (for example, in classical DIS). We conclude, therefore, that the results of Ref. 5 need to be improved for applications of this kind.

On the other hand, the case of the loop-corrected large-angle single photon radiation is described in Ref. 5 with a very high accuracy (only terms of order m^2/ε_1^2 are neglected). In order to reach adequate accuracy for double hard photon emission one needs to take into account the contributions of semicollinear (see paragraph 3 below) and noncollinear kinematics. The last case, when both hard photons are radiated at large angles with respect to the directions of the initial and scattered electron momenta, will be considered by us in another publication.

3. Let us consider double hard photon emission in the semicollinear regions where $\mathbf{k}_1\|\mathbf{p}_1$ or $\mathbf{p}_2$, and $\mathbf{k}_2$ is arbitrary. In this situation we can use the quasireal electron method for a longitudinally polarized initial electron.[9] In accordance with this method the contribution of the region $\mathbf{k}_1\|\mathbf{p}_2$ to the electron current tensor is defined by its Born-like structure $L_{\mu\nu}^{\gamma}$ as follows:

$$L_{\mu\nu}(\mathbf{k}_1\|\mathbf{p}_2)=\frac{\alpha^2}{8\pi^3}\frac{d^3k_2}{\omega_2}\frac{dy_1}{1+y_1}\left[\frac{1+(1+y_1)^2}{y_1}\widetilde{L}_0-\frac{2(1+y_1)}{y_1}\right]L_{\mu\nu}^{\gamma}(p_1,p_2(1+y_1),k_2),$$
(20)

where for the large-angle emission tensor $L_{\mu\nu}^{\gamma}$ we can use the approximation $m^2=0$ (Refs. 3, 5, and 11)

$$L_{\mu\nu}^{\gamma}(p_1,p_2,k_2)=4(B_{\mu\nu}+i\lambda E_{\mu\nu}^{\gamma})$$

$$B_{\mu\nu}=\frac{1}{st}[(s+u)^2+(t+u)^2]\widetilde{g}_{\mu\nu}+\frac{4q^2}{st}(\widetilde{p}_{1\mu}\widetilde{p}_{2\nu}+\widetilde{p}_{1\nu}p_{2\mu}),$$

$$E_{\mu\nu}^{\gamma}=\frac{2\epsilon_{\mu\nu\rho\sigma}}{st}[(u+t)p_{1\rho}q_\sigma+(u+s)p_{2\rho}q_\sigma],\quad \widetilde{g}_{\mu\nu}=g_{\mu\nu}-\frac{q_\mu q_\nu}{q^2},$$
(21)

$$\widetilde{p}_\mu=p-\frac{(pq)q_\mu}{q^2},\quad u=-2p_1p_2,\quad s=2p_2k_2,\quad t=-2p_1k_2,\quad q=p_2+k_2-p_1.$$

As above, the emission of a collinear photon by the initial electron disturbs the Born structure of the electron current tensor in just the same manner as in Eq. (11):

$$L_{\mu\nu}(\mathbf{k}_1\|\mathbf{p}_1)=\frac{\alpha^2}{8\pi^3}\frac{d^3k_2}{\omega_2}\frac{dx_1}{1-x_1}\left\{\left[\frac{1+(1-x_1)^2}{x_1}L_0-\frac{2(1-x_1)}{x_1}\right]\right.$$

$$\left.\times L_{\mu\nu}^{\gamma}(p_1(1-x_1),p_2,k_2)-2x_1i\lambda E_{\mu\nu}^{\gamma}(p_1(1-x_1),p_2,k_2)\right\}$$
(22)

Formulas (20) and (22) have been derived by us independently in the quasireal electron method, starting from the general expression for the current tensor as given by Eqs. (5), (6), and (7).

When calculating the radiative corrections to the polarized DIS cross section we have to integrate over all of the phase space of photons. In this case the angular cutoff parameter θ_0 is unphysical and must vanish in the sum of contributions of the double collinear and semicollinear regions. At the adopted accuracy this implies the cancellation of terms of the type $L_0\ln\theta_0^2$, and that can be verified by separation of $\ln\theta_0^2$ in the integration of $L_{\mu\nu}^{\gamma}(p_1(1-x_1),p_2,k_2)$ in the limit $\mathbf{k}_2\|\mathbf{p}_1$:

$$\int\frac{d^3k_2}{\omega_2}L_{\mu\nu}^{\gamma}(p_1(1-x_1),p_2,k_2\approx x_2p_1)=-2\pi\ln\theta_0^2dx_2\frac{y^2+(1-x_1)^2}{(1-x_1)x_2}L_{\mu\nu}^B.$$
(23)

Taking into account that at fixed $x_1+x_2=1-y$

$$\int dx_1dx_2\frac{[1+(1-x_1)^2][y^2+(1-x_1)^2]}{x_1x_2(1-x_1)^2}=A(y,\delta)dy,$$
(24)

we are convinced that the terms of the type $L_0 \ln \theta_0^2$ indeed vanish in the sum of contributions due to the collinear and semicollinear kinematics. Of course, an analogous cancellation takes place for the radiation in the final state.

We note in conclusion that the electron current tensor has a universal character. It can be used for calculation of cross sections in different processes, including the most interesting DIS and $e^+ e^-$ annihilation into hadrons. To obtain the corresponding cross sections we have to multiply the electron current tensor by the hadron one. The hadron tensor itself carries important information about the hadronic structure and fragmentation functions,[12] and the study of the radiative corrections to the electron current tensor is necessary for interpretation of experimental data in terms of these hadronic functions.

[1] SMC, D. Adams *et al.*, Phys. Rev. D **56**, 5330 (1997).

[2] HERMES, K. Acherstaff *et al.*, Phys. Lett. B **404**, 383 (1997).

[3] T. V. Kukhto and N. M. Shumeiko, Nucl. Phys. B **219**, 412 (1983).

[4] I. V. Akushevich and N. M. Shumeiko, J. Phys. G **20**, 513 (1994).

[5] I. V. Akushevich, A. B. Arbuzov, and E. A. Kuraev, Phys. Lett. B **432**, 222 (1998).

[6] A. B. Arbuzov *et al.*, Nucl. Phys. B **485**, 457 (1997); Phys. Lett. B **399**, 312 (1997); N. P. Merenkov, Zh. Éksp. Teor. Fiz. **112**, 400 (1997) [JETP **85** 217 (1997)].

[7] H. Anlauf, A. B. Arbuzov, E. A. Kuraev, and N. P. Merenkov, http://xxx.lanl.gov/abs/hep-ph/9711333.

[8] A. B. Arbuzov, E. A. Kuraev, N. P. Merenkov, and L. Trentadue (to be published in J. High Energy Phys.).

[9] V. N. Baier, V. S. Fadin, V. A. Khoze, Nucl. Phys. B **65**, 381 (1973); V. N. Baier, V. S. Fadin, V. A. Khoze, and E. A. Kuraev, Phys. Rep. **78**, 293 (1981).

[10] N. P. Merenkov, Yad. Fiz. **48**, 1782 (1988) [Sov. J. Nucl. Phys. **48**, 1073 (1988)].

[11] E. A. Kuraev, N. P. Merenkov, and V. S. Fadin, Yad. Fiz. **45**, 782 (1987) [Sov. J. Nucl. Phys. **45**, 486 (1987)].

[12] X. Ji, Phys. Rev. D **49**, 114 (1994); R. L. Jaffe and X. Ji, Phys. Rev. Lett. **67**, 552 (1991).

Collinear radiative electron–positron scattering in the leading logarithmic approximation

V. Antonelli

Dipartimento di Fisica, Università degli Studi di Milano, Milan, Italy

E. A. Kuraev and B. G. Shaikhatdenov[*)]

Joint Institute for Nuclear Research, 141980 Dubna, Moscow Region, Russia

Radiative corrections to the cross section of the radiative large-angle Bhabha scattering process at high energies are calculated. The kinematics in which a hard photon is emitted along one of the momentum directions of the charged fermions is considered. Contributions coming from the emission of virtual, soft, and hard additional photons are taken into account in the leading logarithmic approximation. © *1999 American Institute of Physics.* [S0021-3640(99)00312-6]

PACS numbers: 12.20.Ds, 13.10.+q

The problem addressed in this paper is motivated mainly by the experimental needs for measuring the cross section of the large-angle electron–positron scattering process to a *per mille* level of accuracy, as this process is used for precise determination of the main characteristic of colliding beams — the luminosity.

To reach a one *per mille* accuracy one must evaluate the radiative corrections (RC) up to third order in the leading logarithmic approximation (LLA) and up to second order in the next-to-leading approximation. Definite sources of these corrections have beem considered in detail in a series of papers.[1–4]

In a recent publication[4] the contribution due to the virtual and soft photon corrections to large–angle radiative Bhabha scattering was calculated in the kinematics in which a hard photon is emitted at large angles with respect to the momenta of all the charged particles. In the present letter we consider the particular kinematics in which the photon moves within a narrow cone of small opening angle $\theta_0 \ll 1$ together with one of the incoming or outgoing charged particles.

In an experimental setup with detection of the scattered electron and positron one cannot distinguish events with an electron alone and those with an electron accompanied by a hard photon moving at small angle $\theta < \theta_0 \ll 1$ with respect to the direction of motion of the electron. When the photon is emitted from the initial particles the back-to-back kinematics[1)] will be violated, whereas in the case of its emission along the scattered particles this kinematics does hold. In the case of emission along the final particles the quantity θ_0 may be associated with the aperture of the detectors.

Upon integration over the photon angular variables, the cross section of the process

$$e(p_1)+\bar{e}(p_2)\rightarrow e(p'_1)+\bar{e}(p'_2)+\gamma(k_1) \tag{1}$$

in the lowest order of perturbation theory takes the form

$$\left(\frac{d\sigma_0^\gamma}{dxdc}\right)_A=\frac{4\alpha^3}{s}\left[\frac{1+(1-x)^2}{x}L_0-2\frac{1-x}{x}\right]$$

$$\times\left(\frac{3-3x+x^2+2cx(2-x)+c^2(1-x+x^2)}{(1-x)(1-c)a^2}\right)^2(1+\mathcal{O}(\theta_0^2)), \tag{2}$$

$$L_0=2\ln\frac{\varepsilon\,\theta_0}{m},\quad s=4\varepsilon^2,$$

where the subscript A on the left-hand side has been used to denote the kinematics in which the hard photon is emitted along the initial electron. The quantity $x=k_1^0/\varepsilon$ is the energy fraction of the hard photon, ε is the energy of the electron in the CM frame, m is its mass, and $c=\cos\hat{\boldsymbol{p}}_1,\boldsymbol{p}'_1$ is the cosine of the scattering angle. The energy fractions of the scattered electron (y_1) and positron (y_2),

$$y_1=\frac{p_1'^0}{\varepsilon}=2(1-x)/a,\quad a=2-x+xc,$$

$$y_2=\frac{p_2'^0}{\varepsilon}=(2-2x+x^2+cx(2-x))/a,$$

and also the positron scattering angle are completely determined by the energy–momentum conservation law.

The cross section in the kinematics of case B, in which the hard photon is emitted along the scattered electron, reads

$$\left(\frac{d\sigma_0^\gamma}{dxdc}\right)_B=\frac{\alpha^3}{4s}\left[\frac{1+(1-x)^2}{x}L'_0-2\frac{1-x}{x}\right]\left(\frac{3+c^2}{1-c}\right)^2(1+\mathcal{O}(\theta_0^2)), \tag{3}$$

$$L'_0=2\ln\frac{\varepsilon'\,\theta_0}{m},\quad \varepsilon'=\varepsilon(1-x).$$

Let us consider first the radiative correction due to the one-loop Feynman diagrams (FDs), which we label as virtual photon emission. There are as many as seventy-two FDs of this type. To simplify the calculation we use the physical gauge (PG) for the real photon:

$$\sum_\lambda e_\mu^\lambda e_\nu^{\lambda*}=\begin{cases}0,&\text{if }\mu\text{ or }\nu=0\\\delta_{\mu\nu}-n_\mu n_\nu,&\mu=\nu=1,2,3\end{cases},\quad \boldsymbol{n}=\frac{\boldsymbol{k}_1}{\omega_1}.$$

As was shown in Ref. 5, this choice proved useful in quantum chromodynamics. It also fits perfectly to the case at hand. In the PG each fermion emits *independently*, contrary to the Feynman gauge, in which a leading contribution (i.e., containing the large logarithm L_0) arises from the interference amplitudes of emission from different fermions. The

contribution from interference terms in the PG is of order θ_0^2. We shall systematically omit these terms throughout, and this determines the accuracy of our approach to be $1 + \mathcal{O}(\theta_0^2 L), L = L_s = \ln(s/m^2)$.

In this letter we deal with the RC to the process (1) in the LLA. Hence the accuracy of the result will be limited to a quantity of the order of $1/L \sim 5\%$ for moderately high-energy colliders such as Φ and J/Ψ factories.

Using the crossing symmetry, we may restrict consideration to only a certain subset of FDs, namely those of the scattering type with one- (G and L types of FDs) and two-photon exchange (B and P types of FDs). For instance, in the A kinematics ($\mathbf{k}_1 \| \mathbf{p}_1$) only nine FDs become relevant. Thus we may write the matrix element squared and summed over spin states as follows:

$$\Sigma |M|_A^2 = \Re e (1 + \mathcal{Q}_1) \left[G + L + \frac{1}{s_1 t} (1 + \mathcal{Q}_2) s_1 t (B + P) \right]. \tag{4}$$

Here we use the kinematical invariants

$$s = (p_1 + p_2)^2, \quad s_1 = (p_1' + p_2')^2, \quad t_1 = (p_1 - p_1')^2,$$

$$t = (p_2 - p_2')^2, \quad u = (p_1 - p_2')^2, \quad u_1 = (p_2 - p_1')^2,$$

$$\chi_1 = 2p_1 k_1, \quad \chi_1' = 2p_1' k_1.$$

The crossing operators act as follows:

$$\mathcal{Q}_1 F(s_1, t_1, s, t) = F(t, s, t_1, s_1), \quad \mathcal{Q}_2 F(s, u, s_1, u_1) = F(u, s, u_1, s_1). \tag{5}$$

The quantities L and G denote the interference between the amplitudes corresponding to the one-loop FDs of fermion self-energy and vertex insertion, with single-photon exchange in the scattering channel, and the two Born level amplitudes, which contain the small denominator χ_1. The graphs of the B and P types describe the interference of two-photon exchange one-loop FDs with uncrossed photon legs. The action of the operator $\mathcal{Q}_1$ yields the contribution of one-loop FDs of the annihilation type, whereas $\mathcal{Q}_2$, when applied to B-type FDs with uncrossed photon legs, provides the contribution of one-loop graphs with crossed photon legs.

The total expression for the virtual RC in case B may be obtained from that for case A by means of the substitution

$$\sum |M|_B^2 = \mathcal{Q} \begin{pmatrix} p_1 \leftrightarrow -p_1' \\ p_2 \leftrightarrow -p_2' \end{pmatrix} \sum |M|_A^2. \tag{6}$$

Omitting details (results to a power-law accuracy, including next-to-leading contributions, will be published elsewhere), we present here the main results of the calculations. The virtual correction in the A kinematics is found to be

$$\left(\frac{d\sigma_V^\gamma}{dxdc} \right)_A = \left(\frac{d\sigma_0^\gamma}{dxdc} \right)_A \frac{\alpha}{\pi} \left[-4L_t \ln \frac{m}{\lambda} + L_{u_1}^2 - L_t^2 - L_{s_1}^2 + \frac{1}{2} L_0 \ln(1-x) + \frac{11}{3} L_t \right],$$

$$L_t = \ln \frac{-t}{m^2}, \quad L_{u_1} = \ln \frac{-u_1}{m^2}, \quad L_{s_1} = \ln \frac{s_1}{m^2}, \tag{7}$$

where λ is a *fictitious* photon mass, introduced to permit regularization of the infrared singularities. The contribution of the soft photon emission process accompanying emission of the hard photon reads

$$\left(\frac{d\sigma_S^\gamma}{dxdc}\right)_A = \left(\frac{d\sigma_0^\gamma}{dxdc}\right)_A \frac{\alpha}{\pi}\left[4L_t\ln\frac{m\Delta\varepsilon}{\lambda\varepsilon} + \frac{1}{2}(L_s^2 + L_{s_1}^2 + L_t^2 + L_{t_1}^2 - L_{u_1}^2 - L_u^2) - L_t\ln(y_1y_2)\right],$$
(8)

$$L_{t_1} = \ln\frac{-t_1}{m^2}, \quad L_u = \ln\frac{-u}{m^2},$$

where $\Delta\varepsilon \ll \varepsilon$ is the uppermost energy of the soft photon in the CM frame.

The emission of two hard photons along the initial electron direction with a total energy fraction x and simultaneously with the energies of each of them exceeding $\Delta\varepsilon$ gives the contribution

$$\left(\frac{d\sigma^{\gamma\gamma}}{dxdc}\right)_A = \left(\frac{d\sigma_0^\gamma}{dxdc}\right)_A \frac{\alpha L}{\pi}\left[-\ln\frac{\Delta\varepsilon}{\varepsilon} - \frac{3}{4} + \frac{1}{2}\ln(1-x) + \frac{x\mathcal{P}_\Theta^{(2)}(x)}{4(1+(1-x)^2)}\right],$$
(9)

$$\mathcal{P}_\Theta^{(2)}(x) = 2\frac{1+(1-x)^2}{x}\left[2\ln x - \ln(1-x) + \frac{3}{2}\right] + (2-x)\ln(1-x) - 2x.$$

The contributions of the kinematics in which a hard photon is emitted by the initial electron and another is emitted by a final electron or by the initial (final) positron, together with the corresponding part of the RC from virtual and soft photons,

$$\left(\frac{d\sigma_0^\gamma}{dxdc}\right)_A \frac{3\alpha L}{\pi}\left[\ln\frac{\Delta\varepsilon}{\varepsilon} + \frac{3}{4}\right],$$
(10)

may be represented in terms of the electron structure function in the spirit of the Drell-Yan formalism as

$$\left\langle\frac{d\sigma_0^\gamma}{dxdc}\right\rangle_A = \frac{\alpha}{2\pi}\frac{1+(1-x)^2}{x}L_0\int dz_2 dz_3 dz_4 \mathcal{D}(z_2)\mathcal{D}(z_3)\mathcal{D}(z_4)\frac{d\sigma_0}{dc}$$

$$\times(p_1(1-x), z_2 p_2; q_1, q_2),$$
(11)

with the nonsinglet structure function $\mathcal{D}(z)$ (Ref. 6):

$$\mathcal{D}(z) = \delta(1-z) + \sum_{n=1}^\infty \frac{1}{n!}\left(\frac{\alpha L}{2\pi}\right)^n \mathcal{P}^{(n)},$$

$$\mathcal{P}^{(n)}(z) = \lim_{\Delta\to 0}[\delta(1-z)\mathcal{P}_\Delta^{(n)} + \Theta(1-z-\Delta)P_\Theta^{(n)}(z)],$$

$$\mathcal{P}_\Delta^{(1)} = 2\ln\Delta + \frac{3}{2}, \quad \mathcal{P}_\Theta^{(1)}(z) = \frac{1+z^2}{1-z}, \dots$$

The cross section of the hard subprocess $e(p_1 z_1) + \bar{e}(p_2 z_2) \to e(q_1) + \bar{e}(q_2)$ entering Eq. (11) has the form

$$\frac{d\sigma_0}{dc}(z_1 p_1, z_2 p_2; q_1, q_2) = \frac{8\pi\alpha^2}{s} \left[\frac{z_1^2 + z_2^2 + z_1 z_2 + 2c(z_2^2 - z_1^2) + c^2(z_1^2 + z_2^2 - z_1 z_2)}{z_1(1-c)(z_1 + z_2 + c(z_2 - z_1))^2} \right]^2.$$

The energies of the scattered fermions and their scattering angles are determined by the energy–momentum conservation law

$$q_1^0 = \varepsilon \frac{2z_1 z_2}{z_1 + z_2 + c(z_2 - z_1)}, \quad q_1^0 + q_2^0 = \varepsilon(z_1 + z_2),$$

$$c = \cos \widehat{\mathbf{q}_1, \mathbf{p}_1}, \quad z_1 \sin \widehat{\mathbf{q}_1, \mathbf{p}_1} = z_2 \sin \widehat{\mathbf{q}_2, \mathbf{p}_1}.$$

Due to subsequent fragmentation, the energies of the detected fermions are

$$\varepsilon_1' = z_3 q_1^0, \quad \varepsilon_2' = z_4 q_2^0$$

and in general do not coincide with those of the scattered fermions in the hard stage, whereas the scattering angles in the LLA remain unchanged. We bring the final expressions for the RC in the LLA to the form

$$\left(\frac{d\sigma^{\gamma(SV\gamma)}}{dxdc} \right)_A = \left(\frac{d\sigma_0^\gamma}{dxdc} \right)_A (1 + \delta_A), \quad \left(\frac{d\sigma^{\gamma(SV\gamma)}}{dxdc} \right)_B = \left(\frac{d\sigma_0^\gamma}{dxdc} \right)_B (1 + \delta_B), \tag{12}$$

with

$$\delta_A = \left[\left(\left(\left\langle \frac{d\sigma_0^\gamma}{dxdc} \right\rangle - \frac{d\sigma_0^\gamma}{dxdc} \right) \left(\frac{d\sigma_0^\gamma}{dxdc} \right)^{-1} \right] \right]_A + \frac{\alpha L}{\pi} \left[\frac{2}{3} - \ln(y_1 y_2) + \frac{x \mathcal{P}_\Theta^{(2)}(x)}{4(1 + (1-x)^2)} \right],$$

$$\delta_B = \left[\left(\left(\left\langle \frac{d\sigma_0^\gamma}{dxdc} \right\rangle - \frac{d\sigma_0^\gamma}{dxdc} \right) \left(\frac{d\sigma_0^\gamma}{dxdc} \right)^{-1} \right] \right]_B + \frac{\alpha L}{\pi} \left[\frac{2}{3} + \frac{x \mathcal{P}_\Theta^{(2)}(x)}{4(1 + (1-x)^2)} \right].$$

The quantities δ_A and δ_B are smooth functions of x and c and have values of the order of a few percent.

In conclusion we note that the Born cross section is seen to factor out of the radiative cross section in the LLA. This is in agreement with a general hypothesis of factorization. Nonetheless, it is evident that the term $\ln(y_1 y_2)$ in δ_A, which stems from soft photon emission, does modify the expected form of the second-order splitting function $\mathcal{P}_\Theta^{(2)}$.

---

*)e-mail: sbg@thsun1.jinr.ru. On leave of absence from the Institute of Physics and Technology, Alma-Ata
[1)]Hereafter the center-of-mass (CM) reference frame of the initial particles is assumed.

---

[1] A. B. Arbuzov, V. A. Astakhov, E. A. Kuraev *et al.*, Nucl. Phys. B **483**, 83 (1997).
[2] A. B. Arbuzov, E. A. Kuraev, N. P. Merenkov *et al.*, Nucl. Phys. B **474**, 271 (1996); Yad. Fiz. **60**, 673 (1997) [Phys. At. Nucl. **60**, 591 (1997)].

[3] A. B. Arbuzov, E. A. Kuraev, and B. G. Shaikhatdenov, Mod. Phys. Lett. A **13**, 2305 (1998).

[4] A. B. Arbuzov, E. A. Kuraev, and B. G. Shaikhatdenov, Zh. Éksp. Teor. Fiz. **115**, 392 (1999) [JETP **88**, 213 (1999)].

[5] A. Bassetto, M. Ciafaloni, and G. Marchesini, Phys. Rep. **100**, 201 (1983).

[6] E. A. Kuraev and V. S. Fadin, Yad. Fiz. **41**, 733 (1985) [Sov. J. Nucl. Phys. **41**, 466 (1985).

Self-induced-transparency soliton laser

V. V. Kozlov

Rochester Theory Center for Optical Science and Engineering, University of Rochester, 14627-0171, Rochester, New York, USA; Research Institute of Physics, St. Petersburg State University, 198904 St. Petersburg, Petrodvoretz, Russia

A passive mode-locking technique with an inhomogeneously broadened absorber is described theoretically in a regime in which the duration of the generated pulse is less than the polarization decay time. The possibility of generation of self-induced-transparency solitons directly from the laser oscillator is shown. A new effect, instability due to spectral hole-burning, is discussed. A comparison with experiment is given. © *1999 American Institute of Physics.*
[S0021-3640(99)00412-0]

PACS numbers: 42.55.Wd, 42.50.Md, 42.65.Tg, 42.60.Mi

Usually the term ''soliton laser'' implies a mode-locked laser, where pulse shaping is due to the interplay between the group-velocity dispersion (GVD) and a Kerr-type nonlinearity. Thus the pulse experiences shaping as a soliton of the nonlinear Schrödinger equation (NLS). Here we refer to a different problem, when the shaping mechanism appears as a result of a *resonant* interaction between a short pulse and a two-level absorber. Conventional techniques of passive mode-locking include either a fast, $\tau \gg T_1, T_2$ (where τ, T_1, and T_2 are the pulse duration and and the decay times of the polarization and population difference, respectively), or a slow, $T_2 \ll \tau \ll T_1$, saturable absorber.[1] If a pulse becomes shorter than the dephasing time, $\tau \ll T_2$, the interaction is called coherent, and above a certain power threshold it may lead to the formation of a self-induced-transparency (SIT) soliton.[2] This case of passive mode-locking with a *coherent* absorber, or in other words, a *SIT soliton laser*, constitutes the subject of this letter.

Although laser operation in the SIT regime is now attracting attention, the level of understanding of the problem seems far from complete. For example, Nakazawa *et al.*[3] described the idea of forming a SIT soliton laser with an erbium-doped fiber (EDF) amplifier at room temperature as the gain medium and an EDF at 4.2 K as a pulse shaper by using the SIT effect. However, in spite of ''ideal'' conditions for SIT, $T^* \ll \tau \ll T_2$ (where $(T^*)^{-1}$ is the inhomogeneous linewidth), the pulse durations obtained were longer than T_2, which means that saturable absorption rather than a coherent pulse formation was dominant in their experiment. The destructive role of Kerr nonlinearity of the fiber[4] can be viewed as a partial explanation for the instability of the SIT regime. A more complete study has to involve the simultaneous solution of the field equation to-
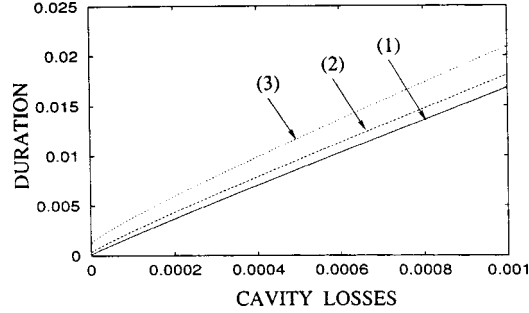
FIG. 1. Normalized duration (τ/T_{2ab}) versus the dimensionless cavity losses (l_{cav}/g_0) for different values of absorber density (a_0/g_0): (*1*) 0.2, (*2*) 0.4, (*3*) 0.8. For parameters see Fig. 2.

gether with the Bloch equations for the amplifier and absorber. The previous studies of the intracavity SIT pulse regime[5] considered the coherent absorber as a homogeneously broadened medium, which is not an appropriate model for an EDF at 4.2 K.

In this letter we develop a theory of a solid-state (fiber) SIT soliton laser with an inhomogeneously broadened absorber and obtain a solution in the form of a 2π pulse. The solution turns out to be unstable in favor of cw operation for the parameters of the experimental setup in Ref. 3. This type of instability has its origin in the familiar hole-burning effect and thus cannot be deduced from the conventional model of a homogeneously broadened absorber. On each round trip a SIT pulse loses in the absorber a small part of its energy ($\propto \tau/T_{2ab}$) due to incomplete Rabi flopping of the population inversion, thus transferring a certain portion of atoms, $\Delta \mathcal{N}_a(\Delta\omega)$, from the ground to the upper state. Since the population relaxes very slowly, $T_{1ab} \approx 10$ ms, compared to the cavity round-trip time $T_R \approx 660$ ns, the absorber is saturated with many ($T_{1ab}/T_R \approx 15000$) pulses (all parameters throughout this letter are taken from Ref. 3). In the steady-state the Gaussian inhomogeneous contour appears to be modified, displaying a profound dip at the center as shown in Fig. 1, because the central group of atoms is saturated more heavily than the others. The net absorption coefficient for the SIT pulse is the nontrivial result of two opposing tendencies: (i) the portion of the lost energy ($\propto \tau/T_{2ab}$) per unit frequency range decreases with decreasing pulse duration; (ii) simultaneously, additional frequency groups of atoms become involved in the absorption as a result of the corresponding increase in the pulse spectral width.[1] On the other hand, a weak narrow-band radiation, which is always present inside a cavity due to spontaneous emission, can experience very small losses in the spectral dip burned by the circulating soliton. If the absorption coefficient for the soliton comes to be larger than that for a cw radiation, the SIT operation becomes unstable. We find that the hole-burning instability takes place for relatively long SIT pulses. We also show that experimental parameters in Ref. 3 lie in the instability region, and one has to increase the pump power to above a certain threshold value in order to get a stable SIT soliton operation.

The wave equation for Rabi frequency can be written in the general form

$$\frac{\partial}{\partial T}\Omega = \left(\frac{\partial}{\partial t} + \hat{O}_{bw} + \hat{O}_D + \hat{O}_g + \hat{O}_{ab}\right)\Omega, \tag{1}$$

where the slow time variable T relates to the evolution over many cavity round trips. The operator $\hat{O}_{\mathrm{bw}}$ accounts for the broad-bandwidth optical filter, where we keep terms up to the second order only:

$$\hat{O}_{\mathrm{bw}} \rightarrow -l_{\mathrm{cav}}[1 - (1/\Omega_f^2)(\partial^2/\partial t^2)].$$

The nonresonant dispersive properties of the host medium are given by the operator $\hat{O}_D$, which includes GVD and self-phase modulation (SPM) in the form

$$\hat{O}_D \rightarrow i[D(\partial^2/\partial t^2) + K|\Omega|^2].$$

The operator $\hat{O}_g$ models the broad-bandwidth homogeneously broadened amplifier,[2)]

$$\hat{O}_g \rightarrow g[1 - T_{2g}(\partial/\partial t)],$$

with g obeying the following differential equation:

$$\frac{d}{dT}g(T) = -\frac{g - g_0}{T_{1g}} - \frac{\Delta\mathcal{N}_g(T)}{T_R}g, \tag{2}$$

where g_0 is the small-signal gain, and $\Delta\mathcal{N}_g$ is the change in population difference after a single round trip,

$$\Delta\mathcal{N}_g(T) = T_{2g}(d_g/d_{\mathrm{ab}})^2 J(T), \quad J(T) \equiv \int^{T_R} |\Omega|^2 dt;$$

$J(T)$ has the meaning of the pulse energy.[3)] Equation (2) implies that population decay time T_{1g} is large compared to T_R, such that g responds only to the average pulse energy $J(T)$ and does not possess an appreciable time-varying component on the time scale of a single round trip. $\hat{O}_{\mathrm{ab}}$ describes the absorber action, which is modeled by the system of Bloch equations. The response of the absorber displays two time scales, one of which is faster than the polarization decay, $T_{2\mathrm{ab}}^{-1}$, and therefore corresponds to coherent pulse shaping. The other is much slower than $T_{2\mathrm{ab}}^{-1}$ and T_R^{-1} and is associated with the slow response of the populations. The latter is insensitive to the particular pulse shape and can be found as a result of averaging the Bloch variables over the cavity round-trip time. A pulse running back and forth inside the cavity selectively saturates the absorption contour, transforming the initial Gaussian distribution of atoms

$$f_0(\Delta\omega) = \exp[-(\Delta\omega T^*)^2]$$

to a more complex shape, $f(\Delta\omega)$, given by

$$\frac{d}{dT}f(T, \Delta\omega) = -\frac{f - f_0}{T_{1\mathrm{ab}}} - \frac{\Delta\mathcal{N}_a(T, \Delta\omega)}{T_R}f, \tag{3}$$

where $\Delta\mathcal{N}_a(\Delta\omega)$ is the fraction of atoms with transition frequencies in the vicinity of $(\omega_0 + \Delta\omega)$ transferred to the upper state by a pulse after a single round trip. Solving the averaged Bloch equations for the absorber, we find $\Delta\mathcal{N}_a$ for two limiting cases:

$$\Delta\mathcal{N}_a^{\mathrm{cw}} = \frac{T_{2\mathrm{ab}}}{1 + (\Delta\omega T_{2\mathrm{ab}})^2}J(T), \quad \text{for } \tau \gg T_{2\mathrm{ab}}, \tag{4}$$

$$\Delta \mathcal{N}_a = \frac{1}{T_{2ab}} \int^{T_R} |\mathcal{P}_{coh}|^2 dt , \quad \text{for} \quad \tau \ll T_{2ab} ; \tag{5}$$

$\mathcal{P}_{coh}$ can be found from a system of Bloch equations:

$$\partial \mathcal{P}_{coh} / \partial t = -i \Delta \omega \mathcal{P}_{coh} + \Omega \mathcal{N}; \tag{6}$$

$$\partial \mathcal{N} / \partial t = -(\Omega \mathcal{P}_{coh}^* + \Omega^* \mathcal{P}_{coh})/2 . \tag{7}$$

Relaxation of polarization does not contribute substantially to the pulse shaping, and the term $(-T_{2ab} \mathcal{P}_{coh})$ is dropped in the right-hand side of Eq. (6). However, the losses in the coherent absorber accumulate over many round trips, and contribute to the net absorption coefficient. The latter can be found in the lower limit of the perturbation theory in a small parameter τ / T_{2ab} (Ref. 2):

$$l(T) = a_0 \frac{\langle \Delta N_a(T, \Delta \omega) \rangle}{\sqrt{\pi} T^* J(T)} , \tag{8}$$

where $\langle \ldots \rangle = (T^* / \sqrt{\pi}) \int \ldots f(\Delta \omega) d\Delta \omega$ denotes averaging over all frequency groups with the distribution function $f(\Delta \omega)$ given by a solution of Eq. (3); a_0 is the unsaturated small-signal absorption of the inhomogeneously broadened medium at the line center. Finally the field equation becomes

$$\frac{\partial \Omega}{\partial T} = \left\{ (g - l_{cav} - l) - [1 + g T_{2g}] \frac{\partial}{\partial t} \right\} \Omega$$

$$+ a_0 \frac{\langle \mathcal{P}_{coh} \rangle}{\sqrt{\pi} T^*} + i \left[D \frac{\partial^2}{\partial t^2} + K |\Omega|^2 \right] \Omega + \frac{l_{cav}}{\Omega_f^2} \frac{\partial^2 \Omega}{\partial t^2} . \tag{9}$$

Equation (9), together with Eqs. (2), (3), (6), and (7), describes the mode-locking operation with a coherent absorber in a self-consistent way. This system is the main result of the present letter. It contains a variety of different regimes arising from an interesting interplay between the resonant and nonresonant mode-locking mechanisms. Here, we limit ourselves by considering the fiber SIT soliton laser proposed in Ref. 3, where the effect of GVD was eliminated by shifting the zero dispersion point to the atomic resonant frequency, and the effect of optical filtering was completely negligible, $\Omega_f \tau > 100$.

When we also put $K = 0$,[4)] the steady-state solution to Eqs. (2), (3), (6), and (7) takes the form of the SIT soliton

$$\Omega = 2 \tau^{-1} \cosh^{-1} [(t - c T_R / L) / \tau] , \tag{10}$$

where L is the length of the cavity. The area of the soliton is equal to 2π, resulting in a unique correspondence between the duration and energy, $J = 8 \tau^{-1}$. The round-trip time is given by

$$T_R = \frac{1}{c} \left[L + L_g g T_{2g} + L_a \frac{a_0 \tau^2}{\sqrt{\pi} T^*} \left\langle \frac{1}{1 + (\Delta \omega \tau)^2} \right\rangle \right] ,$$

where L_g and L_a stand for the lengths of EDF amplifier and EDF absorber, respectively. In the steady state the gain and absorption coefficients reach their stationary values
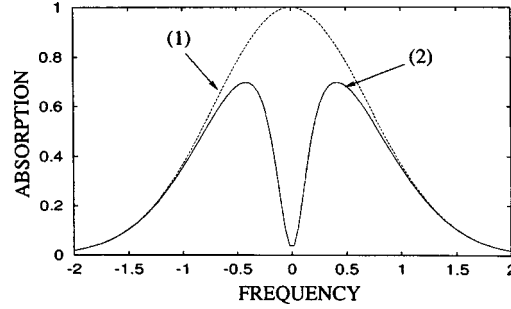
FIG. 2. Inhomogeneously broadened contour: (*1*) original Gaussian distribution of absorbing atoms, $f_0(\Delta\omega)$, of width $(T^*)^{-1}$; (*2*) saturated distribution of the atoms in the ground state for the steady-state mode-locked SIT soliton lasing, $f(\Delta\omega)$, obtained from Eq. (11) with $\tau = 6 \cdot 10^{-3} T_{2ab}$. Other parameters are: $T_{1ab} = T_{1g} = 10$ ms, $T_{2ab} = 3 \cdot 10^{-9}$ s, $T^* = 0.44$ ps, $T_R = 660$ ns. Frequency is in units of $(T^*)^{-1}$.

$$g = \frac{g_0}{1 + \dfrac{T_{1g}}{T_R}\Delta N_g}, \quad f(\Delta\omega) = \frac{f_0(\Delta\omega)}{1 + \dfrac{T_{1ab}}{T_R}\Delta\mathcal{N}_a},$$

$$\Delta\mathcal{N}_a(\Delta\omega) = 8\frac{\tau}{T_{2ab}}\frac{1/3 + (\Delta\omega\tau)^2}{[1 + (\Delta\omega\tau)^2]^2}. \tag{11}$$

It is worth noting that the solution (10) has the same form as for the familiar SIT effect. However, contrary to the classical case, for which the energy/duration of the pulse depends on initial conditions, here the energy/duration has a value uniquely determined by the balance between the net gain and net loss, $g - l_{cav} - l = 0$ [where l is obtained by substitution of (11) into (8)]; see Fig. 1. Additionally, now the SIT soliton propagates through the absorber, the properties of which depend on the parameters of the pulse. Thus the frequency distribution of the atoms is no longer described by a Gaussian function, but transforms into a more complex shape; compare the two curves in Fig. 2. Another, much more important, distinguishing feature between the free-propagating and lasing regimes involves the additional stability problems peculiar to all mode-locked lasers. The mere fact of the existence of a steady-state solution does not ensure that this regime can be realized in practice. In order to convince ourselves that the solution is indeed stable and does not break under the action of small perturbations, we have to perform additional stability tests. In this letter we check the stability of the solitary wave of the form of (10) against the onset of weak cw radiation.

In the limit of highly saturated absorber, $f(\Delta\omega = 0) \ll 1$, which is a very good approximation for solid-state and fiber lasers, one can obtain from Eqs. (8) and (11) an expression for the soliton damping rate:

$$l = a_0 \left[\frac{T_R}{8T_{1ab}}\frac{\tau}{T_{2ab}} \right]^{1/2}, \quad \tau \gg \max\left[T^* ; 8\frac{T_{1ab}}{T_R}\frac{T^*}{T_{2ab}}T^* \right]. \tag{12}$$

The center of the saturated line, where the losses for cw radiation reach their minimum, is the most critical region for the pulse stability. The absorption coefficient for a weak cw field at $\Delta\omega = 0$ is defined by Eq. (8) after the substitution of $\Delta\mathcal{N}_a^{cw}$ in place of $\Delta\mathcal{N}_a$

$$l_{\mathrm{cw}} = \frac{\langle \Delta N_a^{\mathrm{cw}}(\Delta \omega) \rangle}{\sqrt{\pi} T^* J} = \frac{3}{8} a_0 \frac{T_R}{T_{1\mathrm{ab}}} \frac{\tau}{T_{2\mathrm{ab}}}, \tag{13}$$

where we referred to Eq. (4). The stability condition for soliton operation corresponds to the requirement that the soliton losses be smaller than those for cw radiation, $l_s < l_{cw}$. This can be met only with sufficiently short pulses

$$\tau < \left[\frac{9}{8} \frac{T_R}{T_{1\mathrm{ab}}} \right]^{1/3} T_{2\mathrm{ab}}. \tag{14}$$

Substituting the experimental parameters (see the caption to Fig. 2) into Eq. (14), we get stable operation for solitons with durations not longer than 140 ps, which corresponds to peak powers greater than 1.3 kW. In Ref. 3 the pump power was insufficient to produce peak powers as large as this. One can conclude that this is why SIT soliton operation was not observed.

In conclusion, the theory of mode locking of solid-state lasers with an inhomogeneously broadened coherent absorber is developed. A stationary solution in the form of a SIT soliton is found and tested for stability against cw perturbations. Only sufficiently short pulses turn out to be stable; see inequality (14). Based on (14), we conclude that the experimental setup proposed in Ref. 3 must be modified in order to achieve SIT-soliton lasing.

[1] The latter tendency is unique to an inhomogeneously broadened medium as opposed to a homogeneously broadened one, where the absorption coefficient for a SIT soliton is always less than that for cw radiation (apart from the effect of an intracavity spectral filter).

[2] In the experiments of Ref. 3 the homogeneous broadening dominated over the inhomogeneous for the amplifier, while for the absorber the situation was the opposite.

[3] The factor of (d_g / d_{ab}) appears as a result of normalization of the Rabi frequency to the dipole moment of the absorber.

[4] For $K \neq 0$, see Ref. 4

[1] H. A. Haus, J. Appl. Phys. **46**, 3049 (1975); H. A. Haus, IEEE J. Quantum Electron. **QE-13**, 736 (1975).

[2] S. L. McCall and E. L. Hahn, Phys. Rev. **183**, 457 (1969).

[3] M. Nakazawa, K. Suzuki, H. Kubota, and Y. Kimura, Opt. Lett. **18**, 613 (1993).

[4] V. V. Kozlov and E. E. Fradkin, Opt. Lett. **20**, 2165 (1995).

[5] K. P. Komarov and V. D. Ugozhaev, Kvantovaya Elektron. (Moscow) **11**, 1167 (1984) [Sov. J. Quantum Electron. **14**, 787 (1984)]; V. V. Kozlov and E. E. Fradkin, Zh. Éksp. Teor. Fiz. **107**, 62 (1995) [JETP **80**, 32 (1995)]; V. V. Kozlov, Phys. Rev. A **56**, 1607 (1997); V. P. Kalosha, M. Müller, and J. Herrmann, Opt. Lett. **23**, 117 (1998).

Published in English in the original Russian journal. Edited by Steve Torstveit.

Quantum interference and Manley–Rowe relations in resonant four-wave frequency mixing in an optically thick Doppler-broadened medium

A. K. Popov[*] and S. A. Myslivets

Institute of Physics, Siberian Branch of the Russian Academy of Sciences, 660036 Krasnoyarsk, Russia

E. Tiemann and B. Wellegehausen[†]

Institut für Quantenoptik, Universität Hannover, 30167 Hannover, Germany

G. Tartakovsky[‡]

SIMULTEK, USA, 20311 121 CT SE, Kent, Washington 98031-1718

It is shown that under resonant interaction conditions certain notions in nonlinear optics which are based on the Manley–Rowe relations no longer hold because of the interference of elementary quantum-mechanical processes. This conclusion is illustrated by numerical examples corresponding to the experiments performed. © *1999 American Institute of Physics.* [S0021-3640(99)00512-5]

PACS numbers: 42.65.Hw, 42.50.−p

Coherent quantum processes accompanying the interaction of laser radiation with multilevel systems are attracting a great deal of interest because of the possibility of using such processes to manipulate nonlinear-optical responses, the populations of energy levels, refractive indices, and absorption in resonant media.[1,2] Such processes include resonant four-wave processes (RFPs). However, under resonant conditions, together with a giant increase in the nonlinear susceptibilities, many other attendant processes start to play a principal role. This can lead to qualitative contradictions with conventional ideas that hold in limiting cases. The present letter is devoted to this question.

Relatively few experiments have been performed to investigate quantum interference in RFPs in a continuous-wave monochromatic radiation field. Such experiments are difficult because three quite powerful single-frequency lasers with frequency tuning near the resonances must be used simultaneously. One possible solution is to use a Raman transition scheme. Then only two tunable radiations are required in order to obtain RFP by generation of a third radiation on an adjacent transition in the optical pump field. In addition, if molecules with many closely spaced levels are used instead of atoms, then the characteristics of the interacting transitions can be varied and generation can be tuned over a wide frequency range. This possibility was recently realized using the double-Λ transition scheme in sodium dimers (Fig. 1).[3] Similar possibilities have been demonstrated for iodine molecules. For this reason we take as an example the transition scheme
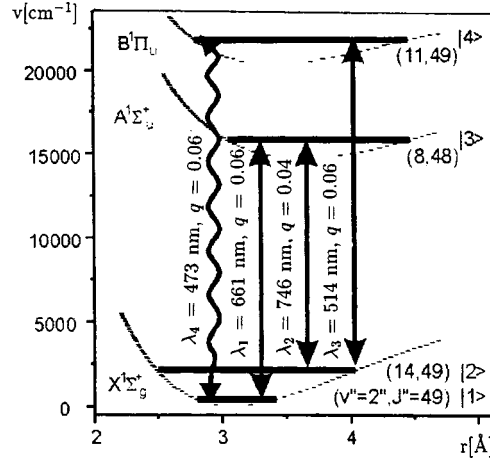
FIG. 1. Scheme of energy levels and transitions in the Na_2 molecule which were used in the experiment of Ref. 3 (the Raman laser runs on the transitions 1-3-2).

corresponding to Fig. 1. The system of wave equations for the slow complex field amplitudes is

$$\frac{dE_{4,2}(z)}{dz} = i\sigma_{4,2}(z)E_{4,2} + i\tilde{\sigma}_{4,2}(z)E_1 E_3 E_{2,4}^*, \tag{1}$$

$$\frac{dE_{1,3}(z)}{dz} = i\sigma_{1,3}(z)E_{1,3} + i\tilde{\sigma}_{1,3}(z)E_4 E_2 E_{3,1}^*. \tag{2}$$

Here $\sigma_j(z) = -2\pi k_j \chi_j(z) = \delta k_j(z) + i\alpha_j(z)/2$, δk_j and α_j are the intensity-dependent resonant components of the wave numbers and absorption coefficients, $\tilde{\sigma}_4(z) = -2\pi k_4 \tilde{\chi}_4(z)$ and so on are intensity-dependent complex nonlinear-coupling parameters for four-wave mixing, and χ_j and $\tilde{\chi}_j$ are the corresponding susceptibilities. The condition $\omega_4 + \omega_2 = \omega_1 + \omega_3$ is assumed to hold. Switching to real amplitudes and phases, we obtain

$$dA_{4,2}/dz = -\alpha_{4,2}A_{4,2}/2 - (\tilde{\sigma}_{4,2}'' \cos\Theta + \tilde{\sigma}_{4,2}' \sin\Theta)A_1 A_{2,4}A_3, \tag{3}$$

$$A_{4,2}d\phi_{4,2}/dz = \delta k_{4,2}A_{4,2} - (\tilde{\sigma}_{4,2}'' \sin\Theta - \tilde{\sigma}_{4,2}' \cos\Theta)A_1 A_{2,4}A_3, \tag{4}$$

$$dA_{1,3}/dz = -\alpha_{1,3}A_{1,3}/2 - (\tilde{\sigma}_{1,3}'' \cos\Theta - \tilde{\sigma}_{1,3}' \sin\Theta)A_2 A_{3,1}A_4, \tag{5}$$

$$A_{1,3}d\phi_{1,3}/dz = \delta k_{1,3}A_{1,3} + (\tilde{\sigma}_{1,3}'' \sin\Theta + \tilde{\sigma}_{1,3}' \cos\Theta)A_2 A_{3,1}A_4, \tag{6}$$

where $\Theta = \phi_1 - \phi_2 + \phi_3 - \phi_4 - \Delta k z$ and $\Delta k = k_1 - k_2 + k_3 - k_4$.

If several strong fields interact with a multilevel system, then the simultaneously occurring elementary processes and interfering quantum paths together lead to a complicated dependence of the optical characteristics of the medium on the frequency and
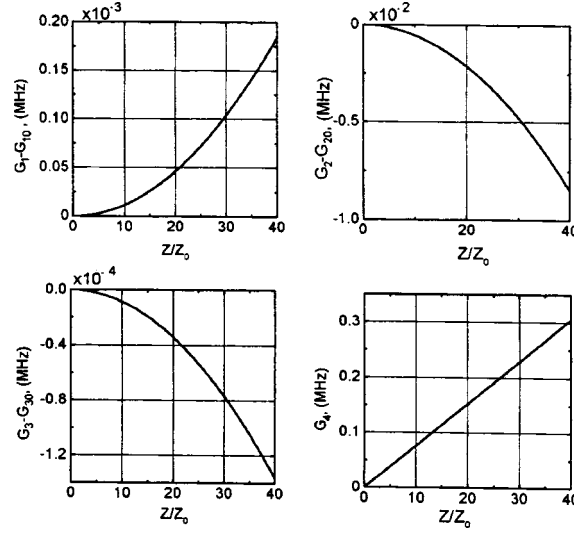
FIG. 2. Completely resonant four-wave conversion on Doppler-broadened transitions. All other accompanying processes are neglected. G_i — interaction parameters (Rabi frequencies, in MHz), G_{i0} — values at the entrance into the medium, Z — thickness of the medium, Z_0 — resonant absorption length of the generated radiation (at the frequency ω_4) in zero fields. $G_{10}=50$, $G_{20}=1, G_{30}=40$ (in MHz). These and the relaxation parameters correspond to the experimental parameters.

intensity of the radiation as well as on all the relaxation parameters by which individual processes can be discriminated.[4] In the limit of weak nonperturbing radiations the expressions for the susceptibilities $\tilde{\chi}_i$ become

$$\tilde{\chi}_2 = \frac{iK}{d_2}\left[\frac{1}{P_{43}^*}\left(\frac{\Delta n_4}{P_4^*} + \frac{\Delta n_3}{P_3} \right) + \frac{1}{P_{41}^*}\left(\frac{\Delta n_1}{P_1} + \frac{\Delta n_4}{P_4^*} \right) \right], \tag{7}$$

$$\tilde{\chi}_4 = \frac{iK}{d_4}\left[\frac{1}{P_{12}}\left(\frac{\Delta n_1}{P_1} + \frac{\Delta n_2}{P_2^*} \right) + \frac{1}{P_{32}}\left(\frac{\Delta n_2}{P_2^*} + \frac{\Delta n_3}{P_3} \right) \right], \tag{8}$$

$$\tilde{\chi}_1 = \frac{iK}{d_1}\left[\frac{1}{P_{43}}\left(\frac{\Delta n_4}{P_4} + \frac{\Delta n_3}{P_3^*} \right) + \frac{1}{P_{32}^*}\left(\frac{\Delta n_2}{P_2} + \frac{\Delta n_3}{P_3^*} \right) \right], \tag{9}$$

$$\tilde{\chi}_3 = \frac{iK}{d_3}\left[\frac{1}{P_{12}^*}\left(\frac{\Delta n_1}{P_1^*} + \frac{\Delta n_2}{P_2} \right) + \frac{1}{P_{41}}\left(\frac{\Delta n_1}{P_1^*} + \frac{\Delta n_4}{P_4} \right) \right]. \tag{10}$$

where $P_j = \Gamma_j + i\Omega_j$ are resonant denominators for the corresponding radiations (for example, $P_4 = \Gamma_4 + i\Omega_4$, $P_{43} = \Gamma_{43} + i(\Omega_4 - \Omega_3)$, and so on); $d_2 = \Gamma_2 + i(\Omega_1 + \Omega_3 - \Omega_4)$, $d_4 = \Gamma_4 + i(\Omega_1 - \Omega_2 + \Omega_3)$, $d_1 = \Gamma_1 + i(\Omega_4 - \Omega_3 + \Omega_2)$, $d_3 = \Gamma_3 + i(\Omega_4 - \Omega_1 + \Omega_2)$; $\Delta n_4 = n_1 - n_4$, Γ_4 is the homogeneous width of the transition 1–4, and so on; n_j are the level populations; $K = d_{13}d_{32}d_{24}d_{41}/4\hbar^3$; and, d_{ij} are the electric-dipole transition moments (see Fig. 1).
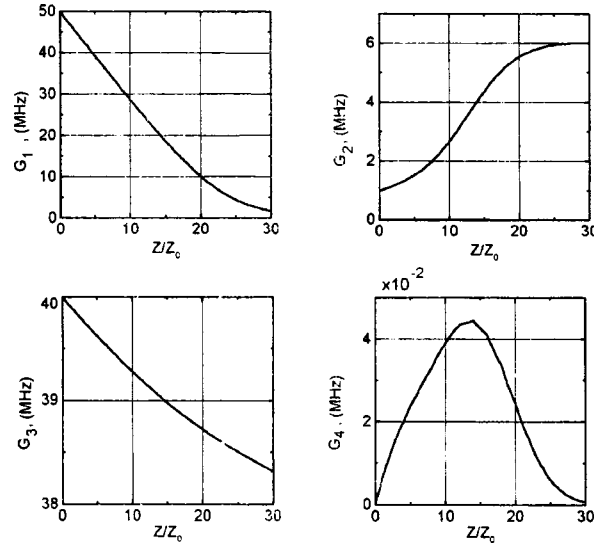
FIG. 3. Same as in Fig. 2 but with allowance for the Raman amplification at the frequency ω_2 and the radiation-perturbed absorption at all other frequencies. The parameters and notation employed are the same as in Fig. 2.

If only the lower level is populated and the departures from all resonances are much greater than the widths of the resonances, all susceptibilities are the same: $\tilde{\chi}_1 = \tilde{\chi}_2 = \tilde{\chi}_3 = \tilde{\chi}_4 = \tilde{\chi} = -Kn_1/\Omega_1\Omega_{12}\Omega_4$. The imaginary parts of the susceptibilities (including absorption) can be neglected in comparison with the real parts. We shall also assume phase matching $\Delta k = 0$. Then the equation for the phase becomes

$$d\Theta/dz = \tilde{\sigma}A_1A_2A_3 \cos\Theta/A_4 .$$

Hence it follows that the phase $\Theta = \pi/2$ is stable, and according to Eqs. (1)–(6) the waves E_1 and E_3 become weaker, while E_2 and E_4 grow. The number of photons $\hbar\omega_1$ and $\hbar\omega_3$ which have vanished is equal to the number of photons $\hbar\omega_2$ and $\hbar\omega_4$ which are generated, and the numbers of each are also equal. At first glance the same thing should happen for the parametric part of the interaction in the resonant case also. However, in this case the susceptibilities become purely imaginary, and their magnitudes and signs differ and their dependences on the radiation intensities are different.[4]

Inhomogeneous broadening due to the variance of the Doppler frequency shifts of individual molecules can also have a large effect on the resonant nonlinear-optical interactions, leading to qualitative effects. In experiments appreciable conversion is ordinarily obtained through the use of optically thick media in which the radiation intensities vary along the medium. For this reason, using the analytical expressions in Ref. 4 to solve the problem posed, we shall illustrate the main results for the resonant case by numerical experiments using an interactive computational program which we developed for this purpose. The perturbation of the medium by the radiation, the Doppler broadening, and effects due to the propagation of the initial and generated radiations in an optically thick

medium are taken into account. In accordance with the experiment, the model employed assumes that each level is perturbed by only a single strong field, i.e., the fields E_1 and E_3 can be arbitrarily strong while all other fields are weak.[4]

The results of the numerical simulation of completely resonant conversion in a Doppler-broadened medium, neglecting the attendant absorption processes, are presented in Fig. 2, and the analogous results obtained with these processes taken into account are presented in Fig. 3. As follows from Fig. 2, the relations obtained on the basis of this approach are in qualitative disagreement with the Manley–Rowe relations (the number of photons $\hbar\omega_1$ increases, while the number of photons $\hbar\omega_2$ decreases). Conversely, the curves in Fig. 3, which were obtained with allowance for the attendant multiphoton absorption and Raman amplification processes, completely agree with the notions concerning the conversion of radiation in absorbing (amplifying) media.

In summary, the main result of this work is that under resonant conditions, in contrast to nonresonant conditions, parametric conversion and absorption of photons cannot be treated independently. This result is also confirmed by a direct analysis of the expressions obtained in Ref. 4, the general forms of which are excessively complicated. Some preliminary results of this work have been presented in Ref. 5.

[*] e-mail: popov@cc.krascience.rssi.ru
[†] e-mail: wellegehausen@mbox.iqo.uni-hannover.de
[‡] e-mail: simultek@msn.com

[1] M. O. Scully, Phys. Rep. **219**, 191 (1992); O. Kocharovskaya, Phys. Rep. **219**, 175 (1992); B. G. Levi, Phys. Today **45**(5), 17 (May 1992); P. Mandel, Contemp. Phys. **34**, 235 (1993); M. O. Scully and M. Fleischhauer, Science **63**, 337 (1994); S. E. Harris, Phys. Today **50**(7), 36 (July 1997).

[2] A. K. Popov and S. G. Rautian, Proc. SPIE **2798**, 49 (1996) (A. V. Andreev, O. Kocharovskaya and P. Mandel, *Coherent Phenomena and Amplification without Inversion*); A. K. Popov, Izv. Ross. Akad. Nauk, Ser. Fiz. **60**, 92 (1996).

[3] S. Babin, U. Hinze, E. Tiemann, and B. Wellegehausen, Opt. Lett. **21**, 1186 (1996); A. Apolonskii, S. Baluschev, U. Hinze *et al.*, Appl. Phys. B: Lasers Opt. **64**, 435 (1997).

[4] A. K. Popov and S. A. Myslivets, Kvantovaya Élektron. (Moscow) **24**, 1033 (1997).

[5] A. K. Popov, S. A. Myslivets, E. Tiemann *et al.*, *Technical Digest of QELS/CLEO,* Baltimore, USA, May 1999.

Translated by M. E. Alferieff

Subwavelength diameter of light beams in active waveguides

T. I. Kuznetsova*)

P. N. Lebedev Physics Institute, Russian Academy of Sciences, 117924 Moscow, Russia

It is shown that there is no frequency cutoff in a uniform cylindrical waveguide containing an amplifying medium. Waves of any frequency grow in the direction of propagation, and for small transverse sections the growth rate is inversely proportional to the waveguide diameter. © *1999 American Institute of Physics.* [S0021-3640(99)00612-X]

PACS numbers: 42.72.Bj, 42.79.Gn

The development of light sources with ultrasmall transverse dimensions is the basis for high-resolution microscopy. The schemes that are in current use[1–3] employ damped waves, as a result of which the light sources obtained using them are weak. The development of a quasipoint source of high-intensity radiation would be very important for high-resolution optical measurements. In this connection, let me call attention to a characteristic feature of waveguides: The properties of the waveguide modes change substantially on switching from a passive to an active waveguide. For definiteness let us consider a waveguide with a circular cross section and perfectly reflecting walls. Let z be the coordinate along the waveguide axis, ρ the distance from the axis, and φ the polar angle. The surface bounding the waveguide is located at $\rho = a$. Consider a wave of the magnetic type[4] (i.e., a TE mode) for which the magnetic field components H_ρ and H_z and the electric field component $E_\varphi \equiv E$ are nonzero; all components vary in time as $\exp(-i\omega t)$ and are independent of the variable φ.

Let the permittivity of the waveguide medium be ε. Then, as is well known, the equation

$$\frac{\partial^2 E}{\partial z^2} + \frac{\partial}{\partial \rho}\left(\frac{1}{\rho}\frac{\partial}{\partial \rho}(\rho E)\right) + \varepsilon\frac{\omega^2}{c^2}E = 0 \tag{1}$$

holds together with the boundary condition

$$E(\rho = a, z) = 0. \tag{2}$$

Consider a wave satisfying Eqs. (1) and (2):

$$E = AJ_1(q\rho)\exp(pz), \tag{3}$$

where

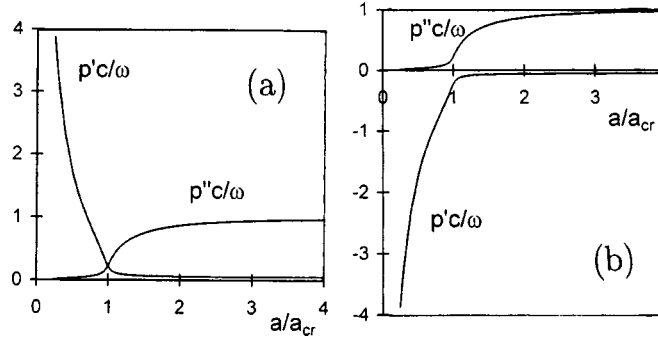$$p^2 - q^2 + \varepsilon(\omega^2/c^2) = 0, \tag{4}$$

FIG. 1. a — Growth rate and wave number of a waveguide mode versus the radius of the active waveguide; b — the same for a waveguide with damping.

$q \approx 3.83/a$, J_1 is a Bessel function, and qa is the first zero of J_1. As is well known, the critical waveguide radius a_{cr} is the radius where

$$(\text{Re } \varepsilon)\frac{\omega^2}{c^2} - [q(a_{cr})]^2 = 0 \tag{5}$$

and which, as a rule, is introduced for the case of real permittivity. For $a > a_{cr}$ the z dependence of the field has the form of a propagating wave $\sim \exp(i\sqrt{\varepsilon(\omega^2/c^2) - q^2}z)$, and for radii less than the critical radius a damped wave is ordinarily chosen. We shall consider an amplifying medium. Let

$$\varepsilon = 1 - i\delta, \tag{6}$$

where $0 < \delta \ll 1$. For real media δ lies in the range $10^{-8} - 10^{-4}$. Let us find the dependence of the field on the longitudinal coordinate in such a medium. For this we need only to calculate the index p. Using Eqs. (4) and (6), we obtain

$$p' + ip'' \equiv p = \sqrt{q^2 - \frac{\omega^2}{c^2} + i\delta\frac{\omega^2}{c^2}}. \tag{7}$$

Hence it is evident that $p'p'' > 0$ for $\delta > 0$, i.e., the direction of growth of the wave is the same as the direction of propagation (equivalent to the direction of energy flux). Calculating the square root in Eq. (7), we obtain the real and imaginary parts of the index p as functions of the waveguide radius a. These dependences are displayed in Fig. 1a for one of the solutions (the second solution is given by $-p'$ and $-p''$). The plots were constructed using the dimensionless growth rate and dimensionless wave number, $p'(c/\omega)$ and $p''(c/\omega)$, and the dimensionless radius a/a_{cr}, where $a_{cr} = 3.83\lambda/2\pi$. The plots were constructed for gain $\delta = 0.1$. For lower values of δ the intersection of the curves at $a/a_{cr} = 1$ remains and the character of the plots does not change, but the plots will be less convenient for visual analysis. The plots show that for large radii the solution is a propagating wave with weak gain, $p' \to \delta(\omega/2c)$, and with longitudinal wave number $p'' \to \omega/c$. As the waveguide radius approaches zero, the growth rate increases and is given by

$$p' \approx q(a). \tag{8}$$

The longitudinal wave number remains positive, decreasing together with a, and is given by

$$p'' \approx \delta \frac{\omega^2}{2c^2 q(a)}. \tag{9}$$

Here the electromagnetic energy flux, which is easy to calculate, is directed along z and its sign is the same as that of p''. Thus positive values of p' and p'' definitely mean that the wave propagates from the entrance into the waveguide and grows in the process. For comparison, the radial dependences of p' and p'' in a waveguide with weak damping are presented in Fig. 1b.

It should be underscored that the exponential growth rate of the field in an amplifying waveguide is very large, and several orders of magnitude greater than the amplification that the same active medium would give in free space. Here the amplitude increases by a factor of e over a distance less than the radiation wavelength. The large gain is due to the characteristics of the wave in the waveguide. It should be noted that for small radii the wave propagates almost perpendicularly to the waveguide walls: Indeed, from Eq. (9) it is easily found that $p'' \ll q$. On propagating over a distance Δz along the axis the light actually traverses a severalfold longer path $\Delta z(2q^2 c^2/\omega^2 \delta)$, which explains the increase in the resulting gain. Thus after entering a uniformly amplifying waveguide, the radiation will propagate with amplification for any diameter-to-wavelength ratio.

Special measures are required to obtain amplification in a waveguide. However, some variants of active waveguides can now be proposed. One such into a micro-waveguide variant can be obtained by introducing a Raman-active material into a micro-waveguide. This requires two light waves at the entrance: a pump wave and the Stokes scattering component (see Ref. 5). On the section where the pump is strong the Stokes component is in an amplifying regime, though it is gradually suppressed because of the damping of the pump. It is difficult to count on amplification over the entire length of the waveguide. Nonetheless, it is possible to increase the penetration depth of the Stokes wave into a cutoff waveguide.

A different variant involves experiments (see Refs. 6 and 7) in which a specific active medium is used to transport energy in a microwaveguide through a nonradiative interaction. In the scheme described in Refs. 6 and 7, it would be good to involve the active medium in both the nonradiative and radiative processes, i.e., to use the inherent amplification of the medium.

The practical implementation of amplifying microwaveguides will make it possible to produce quasipoint sources of high-intensity radiation.

*)e-mail: tkuzn@sci.lebedev.ru

---

[1] D. W. Pohl, W. Denk, and M. Lanz, Appl. Phys. Lett. **44**, 651 (1984).
[2] E. Betzig, J. K. Trautman, T. D. Harris *et al.*, Science **257**, 189 (1992).
[3] A. J. Meixner, D. Zeisel, M. A. Bopp, and G. Tarrach, Opt. Commun. **34**, 2324 (1995).
[4] L. A. Vaĭnshteĭn, *Electromagnetic Waves* [in Russian] (Radio i Svyaz', Moscow, 1988).
[5] T. I. Kuznetsova, in *Raman Scattering of Light. 70 Years of Research* [in Russian] (FIAN, Moscow, 1998), p. 191.

[6] R. Copelman, M. Shortreed, Z.-Y. Shi *et al.*, Phys. Rev. Lett. **78**, 1239 (1997).
[7] V. S. Letokhov and S. K. Sekatskiǐ, JETP Lett. **63**, 319 (1996).

Translated by M. E. Alferieff

Study of polarized argon lines in a plasma focus device

E. O. Baronova*) and G. V. Sholin

Nuclear Fusion Institute, RRC Kurchatov Institute, 123182 Moscow, Russia

L. Jakubowski

The Andrzej Soltan Institute for Nuclear Studies, 05-400 Swierk, Poland

Polarization is important for analyzing line emission in the infrared, visible, and ultraviolet [see A. N. Zaidel and E. Ya. Shreider, *Vacuum Spectroscopy and Its Application* [in Russian], Nauka, Moscow, 1976] and also for x rays. Experimental results are presented for x rays from heliumlike argon in a plasma focus discharge, and ways in which polarized x rays might be created by directional electrons or electric/magnetic fields are discussed.   © *1999 American Institute of Physics.* [S0021-3640(99)00712-4]

PACS numbers: 52.55.Ez, 52.25.Nr

Polarized He-like x rays have been observed in solar flares,[1] laser-produced plasmas,[2] and vacuum sparks.[3] A fruitful collaboration between Polish and Russian scientists provided similar preliminary measurements on a plasma focus machine.[4] A complete interpretation of these spectra is not yet possible because the measurements are averaged over space and time, and other variables are uncontrolled or incompletely known (e.g., the angular distribution, or the calibration as a function of polarization and wavelength). Moreover, how the plasma parameters affect the polarization of the x rays is not yet understood in sufficient detail. This paper presents recent experimental results on evidence for polarization of He-like lines from a plasma focus device, and discusses two effects that might be responsible for the polarization. One is a preferred direction of the electrons that excite the x rays, the other is the orientation of the excited ions in the electromagnetic fields of the pinch.

Time-integrated spectra of ArXVII x-ray lines are taken on a single shot using a 500 kA plasma focus machine.[4] The instrumentation consists of two focusing Johann spectrographs, each with a quartz-crystal cylindrical dispersive element ($2d = 0.8512$ nm and $2d = 0.667$ nm) on a 500 mm radius. The spectral resolution is about $d\lambda/\lambda \sim 8 \times 10^{-5}$. The crystals are calibrated in second and third orders with 8.05 keV x rays from an x-ray tube with a copper anode. The plasma and the crystals are about 700 mm apart. The direction of observation was chosen perpendicular to the discharge axis. A filter consisting of four sheets of 6 μm mylar covered by 0.1 μm Al shields the spectrometers from visible light. To compare the similarity of spectrometers, spectra were measured with the dispersive planes of both devices oriented parallel to the discharge axis. Figure 1 shows the results of these measurements.
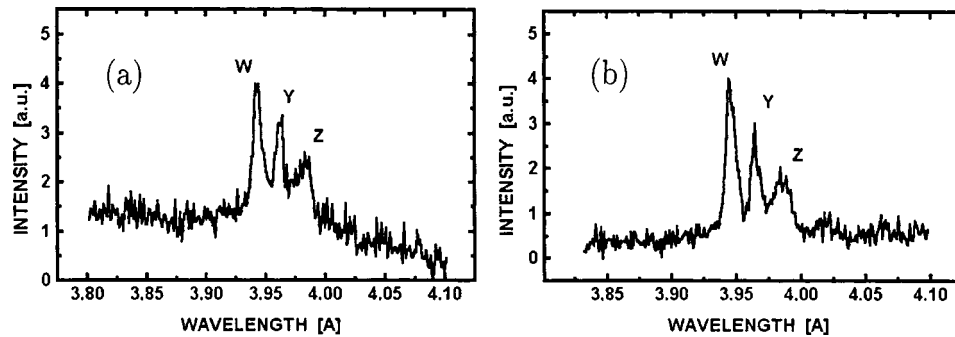
FIG. 1. Ar line profiles measured using the crystal with $2d = 0.851$ nm (a) and the crystal with $2d = 0.667$ nm (b); both were measured with the dispersive planes of the crystals parallel to the discharge axis and were obtained in the same shot.

All of the spectra clearly show the ArXVII $1s2p(^1P_1) - 1s^2(^1S_0)$ resonance line (marked with Gabriel's notation, w), which is well resolved in all cases. The $1s2p(^3P_1) - 1s^2(^1S_0)$ intercombination line (marked y) is also easily resolved. It merges with two additional lines to the right, the $1s2p(^3P_2) - 1s^2(^1S_0)$ magnetic quadrupole transition and the $1s2s(^3S_1) - 1s^2(^1S_0)$ forbidden line. These are x and z in Gabriel's notation. In all the shots the spectra from the two devices show the same shapes of the He-like lines, when the w line is more intense than the y line and when the relative intensities are about the same.

To investigate the polarization we rotated the spectrograph with $2d = 0.667$ nm by 90 degrees. The dispersive planes of the two spectrographs became mutually perpendicular. The devices were optically aligned to observe the same plasma region. Figure 2 shows the results of those measurements.

The two spectra in this figure are substantially different, even though they are taken on the same experimental shot. In Fig. 2a ($2d = 0.815$ nm) the y line is lower than the w line, but when the same lines are taken with another crystal ($2d = 0.667$ nm) in Fig. 2b, the y line is higher than the w line. The spatial averaging done by the instrumentation
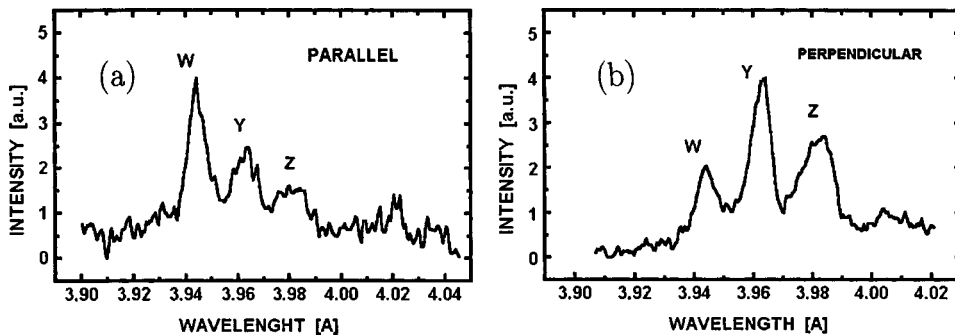

FIG. 2. Ar line profiles measured with the dispersive plane of the crystal with $2d = 0.851$ nm parallel to the discharge axis (a) and with the dispersive plane of the crystal with $2d = 0.667$ nm perpendicular to the discharge axis (b); both were obtained in the same shot.

should suppress temperature and density gradients in and around the bright spots, and should not give different spectra. The same is true for different azimuthal locations for the orthogonal spectrographs: two spectrographs oriented in parallel measure identical spectra. All this evidence suggests that the differences between the two spectra on Fig. 2 might reflect polarization of the x rays. The relative intensity of the w and y lines can be used to estimate the plasma density. However, using the w/y line ratio in the spectra from Fig. 2 gives substantially different density estimates, even though the spectra come from the same plasma. This problem might be resolved by taking x-ray polarization into account explicitly, and correcting for the polarization in measuring the line intensities. Finding line ratios that are consistent in the two spectra gives the degree of polarization of the x rays. The degree of polarization would be interpretable in terms of interesting plasma parameters if it were known how the plasma affects x-ray polarization.

Radiation from a plasma can be polarized if the excited ion has some given direction, if the directed excitation is not randomized before the ion emits a polarized photon, and if the polarized photon leaves the plasma with its original polarization intact. The intensity and polarization of x rays has been calculated using quantum mechanics since 1927:[5] Ref. 6 focuses on the heliumlike ions and the heliumlike lines used here. These lines are favored for plasma diagnostics because they are abundant over a large temperature range and are usually well resolved by modern spectrometers. In hot, dense plasmas the ions are usually excited by electrons with an anisotropic velocity distribution function, and sometimes even by a directional electron beam. Classical plasma diagnostics usually assumes Maxwellian electrons and ignores suprathermal electrons or electron beams.[7] However, recent theoretical studies[8] have shown that even a few percent hot electrons in a Maxwellian tail may affect the line intensities enough to change density and temperature estimates. Moreover, energetic anisotropic electrons and electron beams polarize the x-ray lines, and polarization measurements might give information about these electrons. According to theoretical predictions[8] the degree and direction of polarization of the w, x, and y lines are different and can be equal to 10–60%, while the forbidden line z is unpolarized.

Our spectra show that the w line is polarized in the direction perpendicular to the discharge axis. This is consistent with an electron velocity distribution having a nonthermal tail of moderately energetic electrons (~ 5 keV) peaked in the radial direction. Electrons with a few keV energy have quite complicated orbits that are determined by the configuration of electromagnetic fields inside the plasma.

The fine spatial structure of any type of Z-pinch plasmas (hot spots and micropinches) is well known. In these experiments the x rays come from hot spots in each shot, but the plasma size, the spatial extent of the electron beam, its duration, and the probable interaction of spatially anisotropic hot electrons with multiply charged ions are not known in detail. Certain simplified models suggest that highly ionized ions coexist with fast electrons in the same plasma volume over some time.[9]

Interpreting the polarization measurement in terms of an anisotropic electron distribution assumes that the electric field of the electron is dominant in determining the orientation of the ion during the time needed to radiate the polarized x ray. An alternative possibility is that the electric field of the plasma is dominant in orienting the $2p$-electron orbit in the excited ion, as was first suggested by Sholin.[10] Then the polarization is a measure not of anisotropic electrons but of the electromagnetic fields in the plasma.

Whether this is the case depends on the plasma parameters. In Sholin's model[10] the orientation of the $2p$ orbital in the excited ion is determined by the magnitude of the impact parameter ρ relative to the Weisskopf radius ρ_w (Ref. 11). The orientation is along the electric field of the outgoing electron if $\rho < \rho_w$ and along the magnetic field if $\rho > \rho_w$. In either case, if the ion decays while the orientation of the ion is influenced predominantly by the electron, then the polarization is dominated by anisotropic electrons. If the electron is gone by the time the ion decays, it is the electric/magnetic fields that determine the polarization.

The important quantity is the radiation time compared to the collision time. The collision time is $t_c = a_0/ZV$, where a_0 is the Bohr radius, V is the electron velocity, and Z is the atomic number. The radiative decay time t_r is roughly t_0/a^3Z^4, where $t_0 = a_0 h/2pe^2 = 200$ ns is a typical atomic decay time and a_0 is the fine structure constant. For iron t_r is maybe 0.01 fs, and for typical electron energies t_r/t_c is about 10. Therefore, the polarization should primarily be interpreted in terms of the plasma electromagnetic fields. Quantitative calculations on how large the electric field must be to give substantial polarization of the w line are still underway. However, a preliminary number is about $10^8 - 10^9$ V/cm. Such high fields might exist in a bright spot. One might guess an axial electric field of 100 kV over a 0.1 mm length, or $E = 10$ MV/cm. However, the radial electric field is a factor of $\omega \cdot \tau$ larger, where ω is the cyclotron frequency and τ is the electron collision time. In a hot spot this factor might be up to 100, so that fields up to 1 GV/cm might exist. It is gratifying that the fields estimated from the polarization are about of this order. However, further work must be done to verify that all the relevant influences have been taken into account properly.

The spectra of He-like Ar lines in a plasma focus show clear evidence of polarization for the resonance line (w). Polarization affects the relative intensity of the various lines that are commonly used for diagnostic purposes. Using line ratios might be misleading unless x-ray polarization is explicitly accounted for. Two effects give rise to polarized x rays. The first is anisotropy of the electron velocity distribution, and the second is the existence of macroscopic electric/magnetic fields. A quantitative interpretation of the observed polarization in its preliminary form is in encouraging agreement with what might be expected in and around a hot spot in a Z pinch. However, both the measurements and the theoretical modeling need much additional work before polarization can be used as an unambiguous plasma diagnostics technique by itself.

*)e-mail: baronova@nfi.kiae.su

[1] A. A. Korchak, Dokl. Akad. Nauk. SSSR **172**, 306 (1967) [Sov. Phys. Dokl. **12**, 92 (1967)].
[2] J. C. Kieffer *et al.*, Phys. Rev. Lett. **68**, 480 (1992).
[3] E. O. Baronova, V. V. Vikhrev *et al.*, Plasma Phys. Rep. **24**, 25 (1998).
[4] L. Jakubowski, M. Sadowski, and E. O. Baronova, *Proceedings of the International Conference on Plasma Physics*, Nagoya, Japan (1996), Vol. 2, p. 1326.
[5] J. R. Oppenheimer, Z. Phys. **a43**, 27 (1927).
[6] M. K. Inal and J. Dubau, J. Phys. B: At. Mol. Phys. **20**, 4221 (1987).
[7] L. P. Presnyakov, Usp. Fiz. Nauk **119**, 49 (1978) [*sic*].
[8] F. B. Rosmej and O. N. Rosmej, AIP Conf. Proc. No. 299, AIP Press, New York, 1994, p. 560.

[9] V. Vikhrev and E. Baronova, *Proceedings of the International Conference on Plasma Physics*, Nagoya, Japan (1996), Vol. 1, p. 441.
[10] V. Sholin, Dokl. Akad. Nauk SSSR **175**, 1256 (1967) [Sov. Phys. Dokl. **12**, 811 (1967)].
[11] J. B. Hasted, *Physics of Atomic Collisions*, Butterworths, London, 1964, p. 291.

Electrical conductivity of nonideal hydrogen plasma at megabar dynamic pressures

V. E. Fortov,[*] V. Ya. Ternovoĭ, S. V. Kvitov, V. B. Mintsev, D. N. Nikolaev, A. A. Pyalling, and A. S. Filimonov

Institute of Chemical Physics, Russian Academy of Sciences, 142432 Chernogolovka, Moscow Region, Russia

The electrical conductivity of a nonideal hydrogen plasma is measured under shock-wave compression to pressures ~ 1.5 Mbar. It is found that the conductivity increases sharply (by five orders of magnitude) at a density $\rho \sim 0.3$–0.4 g/cm^3, reaching close to liquid-metal values $\sim 10^3$ S/cm. The data obtained can be described by a nonideal-plasma model taking into account the increase in the number of conduction electrons as a result of ''ionization by pressure.'' © *1999 American Institute of Physics.* [S0021-3640(99)00812-9]

PACS numbers: 52.25.Fi, 07.35.+k

The behavior of hydrogen, the simplest and most abundant element in nature, at high pressures is of great practical and fundamental interest.[1–6] The states of greatest fundamental interest are states at extremely high densities and pressures, where the interparticle interaction energy $E_k \sim e^2 n_e^{1/3}$ is greater than the kinetic energy of disordered motion of the particles, $E \sim kT$ or $E \sim E_F = \hbar^2 n_e^{2/3}/2m$, which makes it difficult to give a theoretical description of such a nonideal plasma and creates great difficulties in studying such a plasma experimentally.[7–9] We note that a number of theoretical models of nonideal plasma[7,9–17] extrapolated to megabar pressures predict a sharp increase in the degree of ionization, accompanied in many cases by ''plasma'' phase transitions with critical points (see Fig. 1) at $T_c \sim 1$–2 eV, $P_c \sim 20$–100 GPa, and $p_c \sim 0.1$–0.5 g/cm^3.

Our objective in the present work was to study experimentally a compressed and heated hydrogen plasma in the region of strong nonideality. For this reason, in contrast to Ref. 3 most experiments were performed by shock-wave compression of targets consisting of hydrogen gas at high pressure, though in a number of experiments we also compressed liquid hydrogen.[18–20]

In the experiments a 2–6 mm thick layer of hydrogen gas ($P_0 = 1$–10 MPa, $T_0 = 77.4$ K) or liquid hydrogen ($P_0 = 0.1$ MPa, $T = 20.4$ K), sandwiched between steel and sapphire disks, was systematically compressed by a series of planar reflected shock waves. These waves were excited by the impact of 1–1.5 mm thick steel impactors accelerated by the detonation products of condensed explosives to 5–6 km/s velocities (see Fig. 2). The geometric dimensions of the experimental setup were chosen so as to
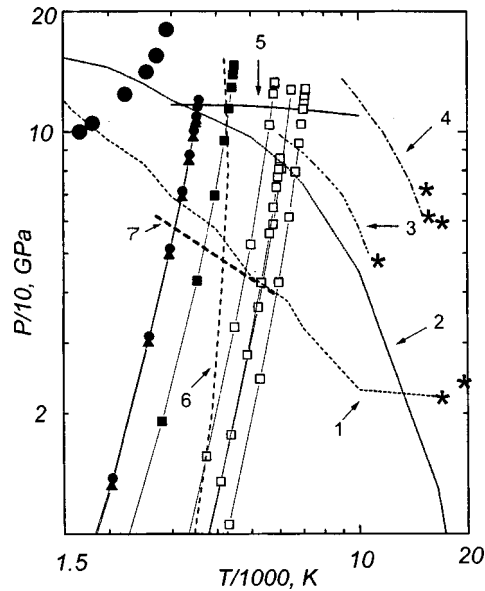
FIG. 1. $P - T$ diagram for hydrogen: ■, □ — states of quasi-isentropic compression of liquid hydrogen and hydrogen gas according to the model of Ref. 22; ● — experimental data of Ref. 3; * — critical points of a plasma phase transition according to different models;[7,10–15] boundaries of plasma phase transitions: curve *1* — Ref. 7, curve *2* — Ref. 10, curve *3* — Ref. 11, curve *4* — Ref. 12, curve *5* — Ref. 13; curve *6* — states of hydrogen in Jupiter's atmosphere;[6] curve *7* — boundary of the onset of a transition to a high-conductivity state according to the results of the present work.

prevent distortion by the lateral and rear unloading waves, thereby making the dynamic compression process stationary and one-dimensional.

A window of single-crystal sapphire (1.8–5 mm thick and ∼15 mm in diameter), which retains its optical and electrical insulating properties under one-time compression
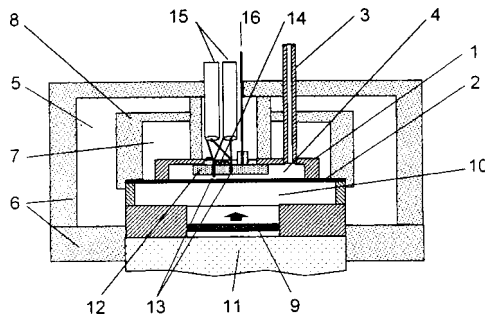

FIG. 2. Diagram of experiments using simultaneous optical and electrical diagnostics of the properties of hydrogen under repeated shock compression: *1* — aluminum case; *2* — stainless steel bottom; *3* — feed and ventilation pipes; *4* — hydrogen; *5* — nitrogen cooling loop; *6,8* — polyurethane foam case of the cooling loops; *7* — hydrogen cooling loop; *9* — steel impactor; *10* — evacuated acceleration chamber; *11* — octogen (HMX) explosive charge; *12* — sapphire window; *13* — measuring and grounding electrodes; *14* — shunting resistance; *15* — current feed and measuring cables; *16* — diaphragmed quartz–quartz optical waveguide.

to 220 GPa,[21] made it possible to detect optical radiation from the hydrogen by means of fast multichannel pyrometers and simultaneously to measure the conductivity by means of electric probes and TDS-744 digital multichannel oscillographs. Prior to each experiment a pulse from a laser diode, connected in place of the electric measuring cell, was recorded to synchronize the measuring systems.

In the experimental arrangement chosen[19–21] the compression and irreversible heating of hydrogen were performed by a series of shock waves in their successive reflection from the sapphire window and the steel impactor. Hydrodynamic analysis of the process showed that the further compression after the first two shock waves have passed through the hydrogen layer is quasi-isentropic. This makes it possible to advance to higher densities than with purely shock-wave compression ($\rho/\rho_0 \sim 10-100$) and low temperatures, thereby intensifying the interparticle interaction effects of interest to us. The reverberation of the shock waves is observed clearly as characteristic ''steps'' in the oscillograms of the radiation and conductivity. The thermodynamic parameters of shock compression — P, ρ, and E — can be determined independently from the measured times of arrival of the shock waves at the boundary of the plasma volume on the basis of the laws of conservation of mass, momentum, and energy.[8] The data so obtained on the energy and temperature equations of state of hydrogen and helium, the latter being chosen as a reference material, up to pressures 30–60 GPa are in agreement with the ''chemical'' model[7,8] of a nonideal plasma as well as with the results of the semiempirical equation of state of hydrogen.[22] However, reliable experimental information on the thermodynamics of hydrogen could not be obtained by this method at pressures above 60 GPa. In this case the thermodynamic parameters of repeated shock compression were calculated using one- and two-dimensional hydrodynamic codes employing semiempirical states of hydrogen[22] and of the structural materials.[23]

The conductivity was recorded using an electrical circuit[24] in the dc regime. The electrical current was delivered to the shock-compressed hydrogen by an electrode arranged perpendicular to the shock wave front. The current flowed along the shock-compressed sample, emerging at the surface of the steel screen and passing out of the region of compression through the grounding electrode.

The agreement between our data and the results obtained in Ref. 3 with the current flowing perpendicular to the front attests to a volume character of the measured conductivity. In a number of experiments, changing the current from 0.5 to 40 A did not lead to nonlinearity of the current–voltage characteristic. This indicates the absence of an electric arc in the plasma layer.

The experimental oscillograms as a whole correspond to the optical measurements and hydrodynamic calculations — the step character of the electric signals corresponds to the moments of arrival of the reflected shock waves, successively compressing the hydrogen to 1–1.5 Mbar pressures. At the final stages of compression the conductivity of the plasma reaches high values $\sim 100-1000$ S/cm, which is close to the measurements in Ref. 3. In our case, however, where the compression starts from the gas phase, the jump in the conductivity is observed at somewhat lower pressures (40–70 GPa) and densities 0.3–0.5 g/cm^3, but it is likewise of a threshold character with respect to the density, without appreciable hysteresis accompanying unloading of the plasma.

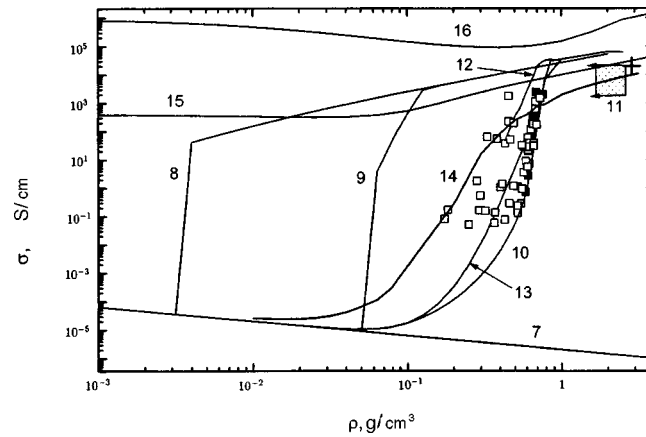The experimental results are displayed in Fig. 3, where they are compared with a

FIG. 3. Conductivity of hydrogen plasma versus density. Experiment: □ — Ref. 20; ■ — Ref. 3, + — Ref. 8. Theory: see citations in text.

number of models of nonideal plasma on the isotherms $T = 4500$ K and with measurements performed by other authors. In the experiment there is a wide spectrum of states of hydrogen, which is compressed to densities $\rho \sim 0.01-0.7$ g/cm^3 and heated to temperatures $T \sim 10^4$ K at pressures up to $P \leqslant 150$ GPa with developed ionization $a \leqslant 0.4$ and a high electron density $n_e \sim 2 \times 10^{23}$ 1/cm^3. At the maximum values of the parameters the plasma is degenerate, $n_e \lambda^3 \sim 200$ ($\lambda = (h^2/2\pi mkT)^{1/2}$ is the de Broglie wavelength) and highly nonideal with respect to the Coulomb interaction, $\Gamma = E_k/E_F \sim 10$, and the interatomic interaction, $\Gamma_a = n_a r_a^3 \sim 1$. The conductivity of the plasma increases sharply (by ~ 5 orders of magnitude) in a relatively narrow density range $\rho \sim 0.2-0.6$ g/cm^3, reaching values characteristic for heated alkali metals.[8]

The sharp increase observed in the conductivity of shock-compressed hydrogen can be explained by athermal growth of the degree of ionization ("ionization by pressure"[7]) because of the strong interparticle interaction in the compressed and disordered medium. Indeed, if the interparticle interaction were neglected, the degree of ionization and therefore the conductivity of an ideal plasma would have decreased with increasing density (curve *7* in Fig. 3) in accordance with the Saha equation of ionization equilibrium,[7,8] since in accordance with the Lorentz and Ziman models the conductivity is proportional to the degree of ionization in the region of weakly ionized plasma.[8] Taking into account the Coulomb interaction using the simplest Debye–Hückel models (curve *8*) and using more modern interpolation approximations that take into account the Coulomb interaction of the charges, the degeneracy of the electrons, and the sizes of the heavy particles[7,13] (curves *9* and *10*, respectively), substantially decreases the ionization potential of the hydrogen atom, sharply increases the degree of ionization of the plasma, and therefore sharply increases the conductivity of the plasma. This sharp dependence in the region of developed ionization becomes weaker at high densities, since on the one hand the processes of hydrogen ionization are completed here, and, on the other hand, according to Spitzer's model for a nondegenerate plasma, the dependence of the conductivity on n_e is only logarithmic, whereas for a degenerate plasma the dependence is linear, approaching the Regel'–Ioffe "minimum" metallic conductivity[16] (curve *11* in Fig. 3). We note that

the models *8*, *9*, and *10* become thermodynamically unstable in our experimental range; this can serve as evidence of a ''plasma'' phase transition. It is significant that the model of Ref. 13, which contains a phase transition, is consistent with the conductivity data.

Shock-wave compression of hydrogen leads to overlapping of the wave functions of the atoms and, in consequence, to a percolation mechanism of conduction,[17] which is described by a density-dependent decrease of the ionization potential (curve *12*). Mott's metallization model[16] also leads to a density-dependent decrease of the ionization potential. This model was used in Ref. 7 to construct a semiempirical wide-range model of ionization equilibrium and transport properties of compressed and heated matter, where the region of ionization by pressure was determined on the basis of experiments with alkali metals — curve *13* in Fig. 3.

Since under the conditions of our experiments the characteristic distance between the atoms is comparable to the sizes of the atoms, the resulting overlap of the atomic electronic shells gives rise to repulsion between the atoms at short distances and correspondingly to an increase in the degree of ionization of the substance. This effect can be reproduced by a model which is a simplified variant of the ''bounded'' atom model.[7,25] In this model the atoms are simulated by an ensemble of hard spheres with radius r_c on the basis of the molecular-dynamics method, and the ring approximation with allowance for the degeneracy of the electrons is used to calculate the thermodynamics of free charges.[7] This variant of the model has been used previously to describe shock-compressed metals at megabar pressures in the region of their ionization by pressure.[25] It is seen (curve *14*) that this approximation gives a reasonable reproduction of the experimentally observed ionization of hydrogen by pressure. As compared to previous experiments with nonideal plasmas,[26,27] this effect is more prominently manifested in hydrogen, since $kT \ll I$ for hydrogen, and it is not masked by thermal ionization effects. To illustrate this effect in hydrogen, the computed isotherms of conductivity for $T = 30\,000$ K (curve *15*) and $T = 10^6$ K (curve *16*) are presented in Fig. 3. It is seen that as the temperature increases, the density dependence of the conductivity is substantially smoothed.

In a future paper we shall present the results of thermodynamic measurements for a hydrogen plasma and of the electrical conductivity for other substances.

*⁾e-mail: fortov@ficp.ac.ru

[1] E. Wigner and H. B. Huntington, J. Chem. Phys. **3**, 764 (1935).

[2] H. K. Mao and R. J. Hemley, Rev. Mod. Phys. **66**, 671 (1994).

[3] S. T. Weir, A. C. Mitchell, and W. J. Nellis, Phys. Rev. Lett. **76**, 1860 (1996).

[4] Yu. Kagan, V. V. Pushkarev, and A. Kholas, Zh. Éksp. Teor. Fiz. **73**, 968 (1977) [Sov. Phys. JETP **46**, 511 (1977)].

[5] N. W. Ashcroft, Phys. Rev. Lett. **26**, 1748 (1968).

[6] W. J. Nellis, N. C. Holmes, and M. Ross, Science **269**, 1249 (1995).

[7] W. Ebeling, A. Forster, and V. E. Fortov *et al.*, *Thermophysical Properties of Hot Dense Plasmas* (Teubner, Stuttgart, 1991).

[8] V. E. Fortov and I. T. Yakubov, *Nonideal Plasma* [in Russian] (Énergoatomizdat, Moscow, 1994).

[9] G. É. Norman and A. N. Starostin, Teplofiz. Vys. Temp. **6**, 410 (1968).

[10] H. Kitamura, and S. Ichimaru, J. Phys. Soc. Jpn. **67**, 950 (1998).

[11] W. R. Magro, D. M. Ceperley, C. Pierleoni, *et al.*, Phys. Rev. Lett. **76**, 1240 (1996).

[12] D. Saumon, and G. Chabrier, Phys. Rev. Lett. **62**, 2397 (1989).

[13] D. Beule, W. Ebeling, A. Forster *et al.*, Contrib. Plasma Phys. **39**, 21 (1999).

[14] M. Robnik and W. Kundt, Astron. Astrophys. **120**, 227 (1983).

[15] H. Reiholz, R. Redmer, and S. Nagel, Phys. Rev. E **52**, 5368 (1995).

[16] N. F. Mott and E. A. Davis*, Electron Processes in Non-Crystalline Materials* (Clarendon Press, Oxford, 1979).

[17] A. A. Likal'ter, Zh. Éksp. Teor. Fiz. **113**, 1094, (1998) [JETP **86**, 598 (1998)].

[18] V. I. Postnov, D. N. Nikolaev, V. Ya. Ternovoi *et al.*, in *Shock Compression of Condensed Matter*, edited by S. C. Schmidt, D. P. Dandekar, and J. W. Forbes (AIP Press, New York, 1997).

[19] V. E. Fortov *et al.*, *Proceedings of the International Conference on Strongly Coupled Coulomb Systems*, Boston, 1997, edited by G. Kalman (Plenum Press, New York, 1998).

[20] V. Ya. Ternovoi, A. S. Filimonov, V. E. Fortov *et al.*, Physica B **265**, 6 (1999).

[21] S. T. Weir, A. C. Mitchell, and W. J. Nellis, J. Appl. Phys. **80**, 1522 (1996).

[22] H. Yuranek, R. Redmer, G. Ropke *et al.*, Contrib. Plasma Phys. **39**, 251 (1999).

[23] A. V. Bushman, I. V. Lomonosov, and V. E. Fortov, *Equations of State of Metals at High Energy Densities* [in Russian] (Institute of Chemical Physics, Russian Academy of Sciences, Chernogolovka, 1992).

[24] R. N. Keeler, Rev. Sci. Instrum. **39**, 513 (1968).

[25] V. K. Gryaznov, M. V. Zhernokletov, I. L. Iosilevskiĭ *et al.*, Zh. Éksp. Teor. Fiz. **114**, 1242 (1998) [JETP **87**, 678 (1998)].

[26] Yu. V. Ivanov, V. E. Fortov, V. B. Mintsev, and A. N. Dremin, Zh. Éksp. Teor. Fiz. **71**, 216 (1976) [Sov. Phys. JETP **44**, 112 (1976)].

[27] V. B. Mintsev, V. E. Fortov, and V. K. Gryaznov, Zh. Éksp. Teor. Fiz. **79,** 116 (1980) [Sov. Phys. JETP **52**, 59 (1980)].

Translated by M. E. Alferieff

Vertical hopping conduction via virtual states in intentionally disordered superlattices

I. P. Zvyagin

M. V. Lomonosov Moscow State University, 119899 Moscow, Russia

A new mechanism of vertical conduction in intentionally disordered superlattices is examined. It is shown that low-temperature conduction due to phonon-assisted tunneling between distant quantum wells of a superlattice is determined mainly by hopping processes via virtual intermediate states. Under standard conditions a weak temperature dependence of vertical conduction is obtained for this mechanism. The characteristic behavior of the conductivity as a function of disorder amplitude is found for this mechanism. © *1999 American Institute of Physics.* [S0021-3640(99)00912-3]

PACS numbers: 73.50.−h, 72.20.Ee

Superlattices and structures with multiple quantum wells into which disorder has been introduced artificially by random controllable variations of the well thickness during growth have been discussed in Ref. 1 and implemented experimentally in Refs. 2 and 3. In such structures, called intentionally disordered superlattices (IDSLs), vertical transport (i.e., transport in the direction of the growth axis) has been investigated by optical methods, specifically, stationary and picosecond luminescence spectroscopy methods, as well as by direct measurements of the vertical conductivity.[2–5] The measurements of the magnitude and temperature dependence of the vertical electron mobility show that even in superlattices (SLs) without artificially introduced disorder, vertical transport at small overlaps of the wave functions of electrons in neighboring wells is often due to phonon-assisted electronic transitions.[6,7] Artificial disorder produces much stronger localization of the electronic states. The character of this localization for short-period GaAs/AlAs SLs with random well-width fluctuations and barrier thicknesses from one to three monolayers has been investigated in detail in Ref. 8 in various regions of the energy spectrum of GaAs/GaAlAs. It was found that for not very high energies the decay length of the wave function is less than the thickness of a monolayer, and conduction is due to phonon-assisted hops between states localized in the direction of the growth axis of the IDSL.[9] A GaAs/Ga$_{0.7}$Al$_{0.3}$As IDSL doped to a density of 5×10^{17} cm^{-3}, with a Gaussian distribution of the energy levels and different values of the rms deviation of the energy levels (we shall refer to this quantity as the disorder energy) have been investigated in Ref. 5. For low disorder energies the temperature coefficient of the vertical resistance was positive, which indicates that transport can be described by studying the phonon scattering of the Bloch electrons in a miniband. In a structure where the disorder energy is greater than the miniband width in an ideal SL, the temperature coefficient of the vertical resistance

became negative, since the electron states in IDSLs are strongly localized in the direction of the growth axis z, and vertical conduction occurs by a hopping mechanism at all temperatures. At the same time, the measurements performed in Ref. 5 show that even for strong localization the temperature dependence of the vertical conductivity at low temperatures is not activational, as one would expect for hops via localized states with strongly differing energies, but is rather weak (it is of a quasimetallic character).

It has been shown[5,10] that the weakening of the temperature dependence of vertical hopping conduction in doped IDSLs could be due to Coulomb fields produced by the redistribution of electrons between the wells of the SL; this decreases the disorder energy. However, this circumstance alone cannot explain the quasimetallic character of the temperature dependence of the conductivity, since the quasimetallic character of the conductivity is preserved in structures with large disorder even though the renormalized disorder energy remains appreciably greater than the miniband width. We shall show below that the weakening of the temperature dependence of the vertical conductivity could be due to a specific hopping mechanism — phonon-assisted tunneling between distant wells in an IDSL via virtual states.

The solution of the problem of an electron in a layered structure with ideally flat boundaries is well known: The states of the electron are characterized by longitudinal (in a direction along the layers) quasimomentum $\mathbf{k}_\parallel$ and quantum numbers λ enumerating the solutions of the one-dimensional Schrödinger equation with the potential $V(z) = \Sigma_n V_i(z)$ describing modulation of the conduction band edge along the growth axis z of the structure, where $V_i(z)$ is the potential of the ith well (we assume that $V_i(z) = 0$ in the region of barriers). The wave functions of electrons in states $\{\lambda \mathbf{k}_\parallel\}$ can be represented in a factorized form, $\psi_{\lambda \mathbf{k}_\parallel} = A U_\lambda(z) \exp(i\mathbf{k}_\parallel \cdot \boldsymbol{\rho})$, where A is a normalization factor, $\boldsymbol{\rho}$ is the radius vector in the well plane, $U_\lambda(z)$ are solutions of the one-dimensional problem that correspond to energy levels ϵ_λ; the energies of the states $\{\lambda \mathbf{k}_\parallel\}$ are $E_{\lambda \mathbf{k}_\parallel} = \epsilon_\lambda + \hbar^2 k_\parallel^2 / 2m$. Since for real structures[5] the rms deviation of the energy levels and the transfer integral are small compared with the distance to the second subband, we shall confine our attention to only the states λ that are obtained as a result of hybridization of the wave functions of the ground state in each well. The wave functions $U_\lambda(z)$ are localized, and the vertical conductivity of the IDSL is determined by the phonon-assisted electronic transitions between the states $\{\lambda \mathbf{k}_\parallel\}$. Just as in the standard theory of hopping conduction along localized states,[11,12] the problem of calculating the vertical conductivity can be reduced to calculating the resistance of an equivalent Miller–Abrahams network whose sites are connected to one another by the resistances

$$R_{\lambda \lambda'} = \left\{ (e^2/kT) \sum_{\mathbf{k}_\parallel, \mathbf{k}_\parallel'} \Gamma_{\lambda \mathbf{k}_\parallel, \lambda' \mathbf{k}_\parallel'} \right\}^{-1}, \qquad (1)$$

where $\Gamma_{\lambda \mathbf{k}_\parallel, \lambda' \mathbf{k}_\parallel'} = W_{\lambda' \mathbf{k}_\parallel', \lambda \mathbf{k}_\parallel} f_{\lambda \mathbf{k}_\parallel} (1 - f_{\lambda' \mathbf{k}_\parallel'})$ are the transition rates from the state $\{\lambda \mathbf{k}_\parallel\}$ into the state $\{\lambda' \mathbf{k}_\parallel'\}$, $W_{\lambda' \mathbf{k}_\parallel', \lambda \mathbf{k}_\parallel}$ are the probabilities of these transitions, and $f_{\lambda \mathbf{k}_\parallel}$ are equilibrium occupation probabilities of the states $\{\lambda \mathbf{k}_\parallel\}$. Here the difference from the standard problem is that to calculate the resistances we must sum over the initial and final states with different values of $\mathbf{k}_\parallel$ and $\mathbf{k}_\parallel'$.

In doped IDSLs at low temperatures, states with energies $E_{\lambda \mathbf{k}_\parallel} < \mu$, where μ is the Fermi level, are filled with electrons. Acoustic-phonon-assisted transitions between such

states occur in a narrow energy range with a width of the order of kT near the Fermi level, and the temperature dependence of the rates of such transitions is nonactivational. However, transitions between the states of wells in at least one of which the bottom of the lowest subband lies above the Fermi level lead to an activational temperature dependence of the resistance, determined by the expression $R_{ij} = R_0 \exp\{(\max(\epsilon_\lambda, \epsilon'_\lambda) - \mu)/kT\}$, where the pre-exponential factor R_0 is an exponential function of the overlap of the wave functions but depends weakly on the energy levels and on the temperature.

When the distance from the level of interest to neighboring levels is greater than the transport integral, the corresponding state remains unhybridized. Then the energy level ϵ_λ is close to the ground-state energy ε_i in the corresponding well, and the function $U_\lambda(z)$ is close to an ''atomic type'' wave function $u_i(z)$, calculated in the approximation that the ith well is isolated. In the limiting case of a large rms deviation of the energy levels and weak overlap of the wave functions of neighboring levels, the Miller–Abrahams network consists of resistances R_{ij} ''connected'' between the levels i and j and expressed in terms of the transition rates between the wells. In the nearest-neighbor approximation, because of the quasi-one-dimensional character of the system under study the vertical resistance of the structure is determined by the sum of series-connected resistances $R_{i,i+1}$. The rms deviation of the energies ε_i leads to an exponentially large scatter in the resistances $R_{i,i+1}$, so that the total resistance of the equivalent chain is determined by a small number of ''critical'' resistances (critical regions of the chains), adjoining wells with the highest energy levels ε_i. This leads to an activational temperature dependence of the resistance, with the activation energy determined by the position of the subband bottom in the critical well relative to the Fermi level.

It is easy to show that an activational temperature dependence of the vertical conduction is still obrtained when the transfer integral has a finite value comparable to the amplitude of the rms deviation of the energy levels. Indeed, once again the total vertical resistance of the structure is determined by the critical wells with the highest-lying levels (i.e., in the high-energy tail of the distribution function). We note that appreciable hybridization occurs only for states for which the distance between the energy levels does not exceed the transfer energy (such states can correspond to ''cluster'' wave functions corresponding to hybridization of the wave functions $u_i(z)$ of several neighboring wells). At the same time the wave functions of the states in critical wells remain unhybridized.

Since the resistance associated with tunneling into a critical well grows exponentially with decreasing temperature, the (phonon-assisted) tunneling between next-nearest neighbors, which is characterized by a much lower activation energy, becomes more favorable. We shall show that the conductivity associated with tunneling between next-nearest neighbors in critical regions is largely determined not by conventional hops but rather by hopping processes via virtual intermediate states.

On this basis the critical region can be schematically represented by the three-level system shown in Fig. 1. Energy level E_2 in the scheme corresponds to the critical well 2, and energy levels E_1 and E_3 correspond to cluster-type neighboring states (in Fig. 1 the clusters are represented schematically by individual wells). It turns out that for the characteristic values of the parameters of the structures investigated experimentally the most likely situation is one in which cluster levels located below the Fermi level, i.e., E_1, $E_3 < \mu$, are present in wells next to critical wells. It is easy to write down an expression
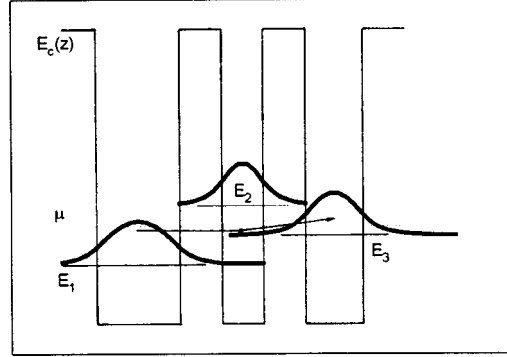
FIG. 1. Critical region of an IDSL (schematic). The arrows show transitions near the Fermi level μ via a virtual state at the center of the well.

for the hybridized wave functions of the three-level problem. The function of the state with the lowest energy E_1 is

$$U_1(z) = A_1\{u_1(z) + c_{12}u_2(z) + c_{13}u_3(z)\}, \tag{2}$$

where A_1 is a normalization factor, $c_{mn} = t_{mn}(E_m - E_n)$, $t_{mn} = \int dz u_m(z)\tilde{V}_n(z)u_n(z)$ is the transfer integral, and $\tilde{V}_n(z)$ is the potential produced by all wells except the ones belonging to the given cluster (here we assume that the overlap of the wave functions is weak and we drop all integrals except the ones containing the wave functions of the nearest neighbors). Similar expressions can be easily written for the functions $U_2(z)$ and $U_3(z)$ on the basis of the present model.

The probability of phonon-assisted transitions between states 1 and 3 can be expressed in terms of matrix elements of the type

$$I_{1\mathbf{k}_\parallel, 3\mathbf{k}_\parallel'} = \int dz \int d\boldsymbol{\rho} \exp\{i(\mathbf{k}_\parallel - \mathbf{k}_\parallel') \cdot \boldsymbol{\rho}\} U_1(z) H_{e,ph} U_3(z)$$

$$= A_1 A_3 \{c_{12} H_{23}^{\mathbf{k}_\parallel \mathbf{k}_\parallel'} + c_{32} H_{12}^{\mathbf{k}_\parallel \mathbf{k}_\parallel'} + c_{12} c_{32} H_{22}^{\mathbf{k}_\parallel \mathbf{k}_\parallel'} + c_{13} H_{33}^{\mathbf{k}_\parallel \mathbf{k}_\parallel'} + c_{31} H_{11}^{\mathbf{k}_\parallel \mathbf{k}_\parallel'}\}, \tag{3}$$

where $H_{mn}^{\mathbf{k}_\parallel \mathbf{k}_\parallel'} = \int dz \int d\boldsymbol{\rho} \exp\{i(\mathbf{k}_\parallel - \mathbf{k}_\parallel') \cdot \boldsymbol{\rho}\} u_m(z) H_{e,ph} u_n(z)$ and $H_{e,ph}$ is the electron-phonon interaction Hamiltonian. Expression (3) describes the transition amplitude between states 1 and 3 as a sum of the contributions of the channels corresponding to tunneling between states localized near different wells via virtual states. The first three terms in Eq. (3) describe transitions via virtual states of the well 2 (for example, the first term corresponds to a phonon-free transition from the state 1 into the state 2 and a phonon-assisted transition from the state 2 into the state 3). The last two terms in Eq. (3) describe transitions via a virtual state of the well 1 or 3. Assuming the energy dependence of the decay length of the wave function to be weak in the subbarrier region, the main exponential dependences on the temperature and on the parameters of the structure are identical for all terms in Eq. (3). Note that in the standard approach to calculating the vertical conductivity of a SL of the type studied in Refs. 7 and 9, just as in problems concerning the hopping conductivity of one-dimensional systems (see, for example, Ref.

13), the probability of phonon-assisted tunneling between states localized near individual wells can be calculated neglecting the other wells, i.e., neglecting hybridization effects. In the present system the probability of such transitions from well 1 into well 3 is much lower than the probability of tunneling via virtual states (3). Indeed, for a direct transition from well 1 into well 3 the matrix element contains the integral $\int dz u_1(z) H_{e,ph}^{\mathbf{k}_\parallel \mathbf{k}_\parallel'} u_3(z)$, proportional to $\exp\{-\alpha(2w+L)\}$, where α is the reciprocal of the decay length of the wave function in the subbarrier region, w is the thickness of the barrier, and L is the width of the critical well. At the same time the terms in the matrix element (3) are proportional to $[t_{mn}^{(0)}/(E_m-E_n)]\exp(-2\alpha w)$, where $t_{12}^{(0)}$ is the pre-exponential factor in the expression for the transfer integral. The ratio of the probability of a transition between distant wells via virtual states to the corresponding probability, calculated neglecting the presence of intermediate wells, is of the order of $(\overline{t^{(0)}}/\bar{E})^2\exp(-2\alpha L)\ll 1$, where $\overline{t^{(0)}}$ is the characteristic value of the pre-exponential factor of the transfer integral (it is of the order of $\sqrt{\hbar^2\varepsilon_1/2m^*L^2}$, where ε_1 is the lowest energy level in the well and m^* is the effective mass[1]), and $\bar{E}$ is the disorder energy. Taking for estimation $\overline{t^{(0)}}=30$ meV, $\bar{E}=20$ meV, and $\exp(-\alpha L)=65$ (these values are characteristic for the structures investigated in Ref. 5), we find that the desired probability ratio is of the order of 2×10^3. Thus the presence of intermediate virtual states must be taken into account when calculating the transition probabilities between distant centers. This distinguishes the situation considered here from the standard problem of hopping conduction for two- and three-dimensional systems of pointlike centers, for which the tunneling length for a process of the type (3) for the typical configuration of centers is much greater than the distance between distant sites.

On account of phonon participation, for the configuration under study transitions between the states $\{1\mathbf{k}_\parallel\}$ and $\{3\mathbf{k}_\parallel'\}$ with close energies $E_{1\mathbf{k}_\parallel}$ and $E_{3\mathbf{k}_\parallel'}$ can occur, and these make the main contribution to the resistance. In this case the resistances of the critical regions depend weakly (nonexponentially) on the temperature. Using Eq. (3), it is easy to estimate the temperature T_1 at which a transition occurs from an activational to a nonactivational dependence of the vertical conductivity. It is determined from the condition $(\bar{t}=\overline{t^{(0)}}/\bar{E})^2=\exp\{-E_a/kT_1\}$, where $\bar{t}=\overline{t^{(0)}}\exp(-\alpha w)$ and E_a is the activation energy (of the order of $\bar{E}$). Taking for estimation $E_a=20$ meV and $\bar{E}/\bar{t}=4$, we find $T_1\approx 80$ K, which agrees with the results of Ref. 5. On this basis the vertical resistance of the structure is determined by the resistance of the critical region which is inversely proportional to the squared modulus of the matrix element (3). According to Eq. (3), when the disorder energy changes, the vertical resistance of the IDSL changes in proportion to the squared disorder energy. In reality, the structures studied with of the order of 100 wells are mesoscopic, and the critical resistance (just as the total vertical conductivity) can fluctuate strongly for different realizations. However, the method used in Ref. 5 makes it possible to investigate the scaling of the conductivity by varying the amplitude of the rms deviation of the energy levels for the same given realization of disorder.

We note that the mechanism of hopping conduction via virtual intermediate states can also play a large role for granular metals. It is well known that when the theory of hopping conduction with a variable hopping length and with allowance for Coulomb effects is applied to granular metals in the insulating region, where the conductivity is due to phonon-assisted tunneling between metallic grains, it describes a temperature

dependence of the conductivity which ordinarily has the form $\ln\sigma=\ln\sigma_0-(T_{SE}/T)^{1/2}$, where σ_0 and T_{SE} are parameters. However, one difficulty of the theory is that the decay length of the wave function, which determines the tunneling between non-nearest-neighbor grains, must be chosen anomalously large in order to obtain the correct value of the conductivity (see, for example, Refs. 14–16). This difficulty could be due to the fact that the theory has neglected hops via intermediate virtual states; generally speaking, such processes greatly increase the probability of phonon-assisted tunneling to distant grains.

[1] J. D. Dow, S. Y. Ren, and K. Hess, Phys. Rev. B **25**, 6218 (1982).

[2] A. Chomette, B. Deveaud, A. Regreny *et al.*, Phys. Rev. Lett. **57**, 1464 (1986).

[3] T. Yamamoto, M. Kasu, S. Noda *et al.*, J. Appl. Phys. **68**, 5318 (1990).

[4] M. Lee, S. A. Solin, and D. R. Hines, Phys. Rev. B **48**, 11921 (1993).

[5] G. Richter, W. Stolz, S. Koch *et al.*, Superlattices Microstruct. **74**, 475 (1997).

[6] R. Tsu and G. Dohler, Phys. Rev. B **12**, 680 (1975).

[7] D. Caleski, J. F. Palmier, and A. Chomette, J. Phys. C **17**, 5017 (1984).

[8] K. A. Mäder, W. Lin-Wang, and A. Zunger, Phys. Rev. Lett. n **74**, 2555 (1995).

[9] Lin-Wang Wang, A. Zunger, and K. A. Mäder, Phys. Rev. B **53**, 2010 (1996).

[10] I. P. Zvyagin and M. A. Ormont, Fiz. Tekh. Poluprovodn. **33**, 79 (1999) [Semiconductors **33**, 69 (1999)].

[11] B. I. Shklovskiǐ and A. L. Éfros, *Electronic Properties of Doped Semiconductors* (Springer-Verlag, New York, 1984) [Russian original, Nauka, Moscow, 1979].

[12] V. L. Bonch-Bruevich, I. P. Zvyagin, R. Kaǐper *et al.*, *Electronic Theory of Disordered Semiconductors* (Nauka, Moscow, 1981).

[13] J. Kurkijärvi, Phys. Rev. **8**, 922 (1973).

[14] C. J. Adkins, J. Phys.: Condens. Matter **1**, 1253 (1989).

[15] M. Pollak and C. J. Adkins, Philos. Mag. B **65**, 855 (1992).

[16] C. J. Adkins, in *Proceedings of the 6th International Conference on Hopping and Related Phenomena,* edited by O. Millo and Z. Ovadyahu (Racah Institute of Physics, The Hebrew University, Jerusalem, 1995).

Translated by M. E. Alferieff

X-ray spectroscopy of thermally distorted electronic states in crystals

V. E. Dmitrienko

A. V. Shubnikov Institute of Crystallography, 117333 Moscow, Russia

E. N. Ovchinnikova

Moscow State University, Physics Department, 119899 Moscow, Russia

K. Ishida

Department of Physics, Science University of Tokyo, Noda-shi, Chiba 278, Japan

A new type of x-ray spectroscopy is proposed which can detect the thermal-motion-induced distortions of atomic electronic states in crystals. It is shown that those distortions can cause extra Bragg reflections (so-called forbidden reflections) and that their intensity should grow with increasing temperature. The reason is that the thermal displacements, which change the symmetry of atomic environment, can modify the tensor amplitude of x-ray resonant scattering. In the first approximation, the structure factor of extra reflections is proportional to the reflection vector $\mathbf{H}$ and to the mean-square thermal displacement $\overline{u_j u_k}$ for optical phonons. It is demonstrated that the forbidden resonant reflections, observed recently in Ge, could be caused by the thermal motion. © *1999 American Institute of Physics.*

[S0021-3640(99)01012-9]

PACS numbers: 78.70.Ck, 61.10.Eq

X-ray resonant scattering is now widely used to study structural and magnetic properties of solids.[1,2] The resonant effects are especially important for additional reflections, which can appear in x-ray diffraction when the energy of the incident radiation approaches the values required to excite an inner-shell electron to an empty state of an outer shell. These ATS (Anisotropy of the Tensor of Susceptibility) reflections occur even in nonmagnetic crystals because the outer shells are strongly affected by the local environment and therefore the atomic scattering amplitude becomes anisotropic.[3–5] It was shown that the anisotropy violates the extinction rules, tabulated for glide planes and/or screw axes, and new general extinction rules were found in the dipole approximation.[4] This anisotropy is local and therefore it is allowed even in cubic crystals and in icosahedral quasicrystals[5,6] if the resonant atoms are at sites with not too high symmetry. However, if the symmetry of the sites occupied by the resonant atoms is high (for instance, cubic), the anisotropy is absent and no ATS reflections are expected. In principle, if ATS reflections are forbidden in the dipole approximation they can be obtained in the dipole–quadrupole or higher approximations.[7,8] ATS reflections have been observed in many crystals and in

liquid crystals, they demonstrate very unusual polarization properties (see Refs. 9 and 10 for reviews). From a practical standpoint the ATS reflections provide us with an instrument for x-ray spectroscopy of the atomic electronic states distorted by crystal fields.

The present paper explores some of the complications that arise in coherent resonant scattering of x rays when thermal atomic motion is taken into account. Previously the forbidden reflections caused by the asphericity of thermal motion have been observed far from absorption edges (a survey may be found in Ref. 11). The latter effect does not violate the glide-plane and screw-axis extinction rules. In contrast, we show that the thermal motion can change the anisotropy of the resonant scattering and can induce extra reflections violating the glide-plane and screw-axis extinction rules. Thus the spectroscopy of these thermal-motion-induced (TMI) reflections could provide information about thermally distorted electronic states.

ANISOTROPY OF SCATTERING AND THERMAL ATOMIC MOTION

In this section we demonstrate schematically how the anisotropy of resonant scattering and the tensor structure factor could be changed by thermal motion. To illustrate the basic idea we will use atomic scattering factors instead of a more rigorous approach based on x-ray susceptibility. The anomalous contribution to the scattering factor of an atom is described by a symmetric tensor f_{jk}, which depends not only on the x-ray frequency ω but also on the environment of this atom. The resonant part of the tensor scattering factor of the sth atom in the unit cell can be written in dipole approximation as:[2]

$$f_{jk}^s(\omega,\mathbf{r}^s)=\sum_{a,b} p_a \frac{(E_a-E_b)}{\hbar\omega m} \frac{\langle a|P_j^+|b\rangle\langle b|P_k|a\rangle}{E_a-E_b+\hbar\omega-i\Gamma/2},\tag{1}$$

where $\mathbf{r}^s$ is a current atomic position, $|a\rangle$ describes the initial and final electronic states with energy E_a, p_a is the probability of finding the atom in the $|a\rangle$ state, $|b\rangle$ describes an intermediate electronic state with energy E_b, and $\mathbf{P}=-i\hbar\Sigma_n\nabla^{(n)}$, the last summation extending over all electrons in the atom.

The tensor f_{jk}^s is a function of $\mathbf{r}^s$ because the intermediate states $|b\rangle$, corresponding to outer shells, depend on the atom's environment and, in particular, on the current position $\mathbf{r}^s$ of the sth atom among other atoms. In fact, it is well known that even small *static* changes of the environment can noticeably change f_{jk}^s. For example, for octahedral symmetry f_{jk}^s should be isotropic. However, in the FeS_2 and Fe_2O_3 crystals, where each iron atom is contained inside a slightly distorted octahedron of sulfur or oxygen atoms, a pronounced anisotropy of f_{jk}^s is observed.[12,13] The thermal motion produces *dynamic* changes of the environment. For them it is important that $f_{jk}^s(\omega,\mathbf{r}^s)$ is determined by the electron subsystem of the crystal, which is much faster than nuclear motion — the so-called Born–Oppenheimer or adiabatic approximation. Therefore the outer electronic states follow the current atomic configurations. Another important approximation, used implicitly in (1), is that the typical time of x-ray resonant scattering, $\hbar/\Gamma$, is much smaller than the typical time of thermal motion. Just because of this we should take into account only the current atomic position $\mathbf{r}^s$ in (1) as if it were a static position (i.e., the atomic position does not change during scattering).

We see that the value of the tensor $f_{jk}^s(\omega, \mathbf{r}^s)$ changes all the time in accordance with the thermal motion, and the current symmetry of this tensor corresponds to the current symmetry of the atomic positions. This is in contrast, for example, with the Mössbauer resonant scattering, where the typical time is much longer than that of thermal motion, and the symmetry of the resonant scattering amplitude corresponds to the *average* symmetry of the atomic site. For simplicity we will suppose hereafter that the electronic wave functions for the sth atom, $|b\rangle$, their energy, E_b, and, hence, f_{jk}^s are functions of $\mathbf{r}^s$ only, i.e., we neglect the thermal motion of neighboring atoms.

To obtain the tensor structure factor $F_{jk}(\mathbf{H})$ describing the coherent scattering for reflection $\mathbf{H}$, we should multiply $f_{jk}^s(\omega, \mathbf{r}^s)$ by $\exp(i\mathbf{H}\cdot\mathbf{r}^s)$, do a summation over all atoms, and then average over thermal vibrations:

$$F_{jk}(\mathbf{H}) = \sum_s \overline{f_{jk}^s(\omega, \mathbf{r}^s)\exp(i\mathbf{H}\cdot\mathbf{r}^s)} ; \tag{2}$$

hereafter the bar means thermal averaging.

Actually, since it is very difficult to compute $f_{jk}^s(\omega, \mathbf{r}^s)$, we will use a phenomenological approach. We suppose that the thermal displacement $\mathbf{u}^s$ ($\mathbf{u}^s = \mathbf{r}^s - \mathbf{r}^{0s}$) from the average position $\mathbf{r}^{0s}$ is small enough that we can use a tensor expansion of f_{ik}^s and $\exp(i\mathbf{H}\cdot\mathbf{r}^s)$:

$$\exp(i\mathbf{H}\cdot\mathbf{r}^s) = (1 + i\mathbf{H}\cdot\mathbf{u}^s + \ldots)\exp(i\mathbf{H}\cdot\mathbf{r}^{0s}), \tag{3}$$

$$f_{jk}^s(\omega, \mathbf{r}^s) = (f_{jk}^{0s} + f_{jkl}^{1s}u_l^s + f_{jklm}^{2s}u_l^s u_m^s + \ldots). \tag{4}$$

On the right-hand side of (4), all the tensors $\hat{f}^{ps}$ of different ranks are invariant under the "average" symmetry group, which coincides with the point group of the atom site. Substitution of (3) and (4) into (2) gives us the terms $\overline{u_l u_m \ldots u_n}$. Because we are interested in thermal effects, we will consider only those situations when the zero-order term f_{jk}^{0s} vanishes fir reasons of symmetry. The first nonvanishing term is obviously $\overline{u_l u_m}$, and hereafter we keep only its contribution to the tensor structure factor. It is evident that $f_{jklm}^{2s}\overline{u_l^s u_m^s}$ has exactly the same symmetry as f_{jk}^{0s}, and they vanish together; the same is valid for all the terms in (4). Thus the TMI contribution arises only from those cross terms in (2) which are proportional to $\mathbf{H}\cdot\mathbf{u}$ or to higher powers of $\mathbf{H}\cdot\mathbf{u}$. Generally, the first nonvanishing term is $if_{jkl}^{1s}H_m\overline{u_l^s u_m^s}$.

The analysis of (2) provides the following simple recipe for TMI-ATS reflections: only those extinction rules and those restrictions on the tensor structure factor which are found for general atomic sites[4] are valid. The additional restrictions found for special sites[5] are violated by the thermal vibrations providing the TMI-ATS reflections. This is quite obvious from the physical point of view because vibrating atoms leave special sites and spend most of the time in general positions. Therefore only the general extinction rules survive.

EXAMPLES

If the resonant atoms are at sites with cubic point symmetry, then $f_{jkl}^{1s} = f^{1s}T_{jkl}$, where $T_{jkl} = e_j^1 e_k^2 e_l^3$, and $\mathbf{e}^1, \mathbf{e}^2, \mathbf{e}^3$ is a right-hand triad of unit vectors directed along cubic axes. The tensor $\hat{T}$ is nonzero only for the 23 and $\bar{4}3m$ cubic groups, where its

nonzero components are $T_{xyz}=T_{yzx}=T_{zxy}=T_{xzy}=T_{zyx}=T_{yxz}=1$. Taking into account that $\overline{u_j u_k}=\overline{\mathbf{u}^2}\delta_{jk}/3$ for cubic symmetry, we have $f_{jk}^s=if^{1s}T_{jkl}H_l\overline{\mathbf{u}^2}/3$.

Let us consider the $0kl, k+l=4n+2$ forbidden reflections in the Ge crystal (symmetry group $Fd\overline{3m}$; the atoms are in special positions $8(a)$ with $\overline{4}3m$ symmetry). This extinction is induced by the atoms at (000) and (1/41/41/4), which scatter in antiphase, causing the conventional structure factor to vanish. However, because these atoms are related by an inversion center, the corresponding tensors f_{jkl}^{1s} have opposite signs. Hence the TMI mechanism provides in-phase resonant scattering. Finally, we obtain from (2) for Ge crystals:

$$F_{ij}(0kl,k+l=4n+2)=\frac{8}{3}if^{1s}\overline{\mathbf{u}^2}\begin{pmatrix} 0 & H_z & H_y \\ H_z & 0 & 0 \\ H_y & 0 & 0 \end{pmatrix}. \tag{5}$$

We see that the structure factor is proportional to $\overline{\mathbf{u}^2}$ and H_j. The unknown phenomenological coefficient f^{1s} is the same for all TMI reflections in Ge and does not depend on temperature. However, according to (1), it strongly depends on ω.

If resonant atoms are located at special sites of noncubic crystals, there are various cases when the conventional ATS contribution is absent but the TMI contribution is possible. Let us consider K_2CrO_4, where the resonant Cr atoms are in sites 4(c) of the space group $Pnma$ with the coordinates: (1) $x,1/4,z$; (2) $-x,3/4,-z$; (3) $1/2-x, 3/4, 1/2+z$; (4) $1/2+x,1/4,1/2-z$. Because all the Cr atoms are on mirror planes, the temperature-independent dipole–dipole terms vanish for $0k0, k=2n+1$ reflections. However, for the group m_y, the third-rank tensor f_{jkl}^{1s} has 10 independent components, and one of them, f_{xyy}^{1s}, contributes into the structure amplitude:

$$F_{jk}(0k0, k=2n+1)=4iH_y\overline{u_y^2}f_{xyy}^{1s}\begin{pmatrix} 0 & 1 & 0 \\ 1 & 0 & 0 \\ 0 & 0 & 0 \end{pmatrix}. \tag{6}$$

Again we have only one phenomenological parameter, f_{xyy}^{1s}, for all $0k0, k=2n+1$ reflections.

DISCUSSION AND CONCLUSION

It is quite evident that acoustic phonons give no contribution to the TMI anisotropy because in the acoustic phonon modes each unit cell moves as a whole and no anisotropy appears. Thus, only relative atomic displacements should be taken into account. This is similar to the calculation of the temperature factor for the extended x-ray absorption fine structure (EXAFS), where again only the relative positions of the atoms are of importance. In the simplest approximation, we can suppose that each atom moves independently among the others. In this case we should calculate $\overline{u_j u_k}$ taking into account only optical phonons. In Ge crystal, the frequency of optical modes ω_0 changes only slightly with the wave vector, and for estimations we can put $\omega_0=\text{const}=5\times10^{13}$ s^{-1}. In this case,

$$\overline{u_i^2}\sim\frac{\hbar}{2M\omega}\coth\frac{\hbar\omega}{2k_BT},$$

where M is the Ge atomic mass. For high temperature $\overline{u_i^2} \sim k_B T / M \omega^2$, and therefore the structure amplitude of TMI-ATS reflections is proportional to T and to $\mathbf{H}$ (for 1000 K $\sqrt{\overline{u_i^2}} \approx 0.06$ Å). More exactly, instead of $i H_m \overline{u_l^s u_m^s}$ we should write

$$\overline{u_l^s \exp(i H_m u_m^s)} = -i \frac{d}{dH_l} \overline{\exp(i H_m u_m^s)}$$

$$= -i \frac{d}{dH_l} \exp(-H_m H_n \overline{u_m^s u_n^s}/2) = i H_m \overline{u_l^s u_m^s} \exp(-H_m H_n \overline{u_m^s u_n^s}/2).$$

Thus the tensor structure factor ceases to grow with T and $\mathbf{H}$ and reaches its maximum when $\mathbf{H}^2 \sim 1/\overline{\mathbf{u}^2}$. The TMI anisotropy should be more pronounced when the amplitude of optical modes is large, for example near structural phase transitions of second order.

Notice that the tensor form of (5) coincides with the tensor form of the dipole–quadrupole contribution to the structure amplitude,[8] but in the latter case the structure amplitude should decrease with temperature growth because of the Debye–Waller factor. This allows us to distinguish the dipole–quadrupole and TMI contributions to the scattering factor. Therefore high temperature measurements are required to clarify the origin of the $0kl, k+l = 4n+2$ reflections observed near the absorption edge of Ge.[8,14] Those two contributions may be also distinguished owing to their different spectra, corresponding to dipole–quadrupole and dipole–dipole transitions.

In conclusion, we have shown that the resonant spectroscopy of special ''forbidden'' reflections could provide a unique method for studying those distortions of electronic states which appear owing to thermal deviation from average atomic positions. The effect under discussion is sensitive only to the thermal vibrations of resonant atoms, while all other atoms give no contribution. Conversely, this effect may be used to study the temperature dependence of special phonon modes contributing to local symmetry distortions.

[1] D. H. Templeton, in *Resonant Anomalous X-Ray Scattering*, edited by G. Materlik, C. J. Spark, and K. Fisher, North-Holland, Amsterdam (1994), p. 1.

[2] M. Blume, in *Resonant Anomalous X-Ray Scattering*, edited by G. Materlik, C. J. Spark, and K. Fisher, North-Holland, Amsterdam (1994), p. 495.

[3] D. H. Templeton and L. K. Templeton, Acta Crystallogr., Sect. A: Cryst. Phys., Diffr., Theor. Gen. Crystallogr. **36**, 237 (1980).

[4] V. E. Dmitrienko, Acta Crystallogr., Sect. A: Crystallogr. **39**, 29 (1983).

[5] V. E. Dmitrienko, Acta Crystallogr., Sect. A: Crystallogr. **40**, 89 (1984).

[6] V. E. Dmitrienko, JETP Lett. **50**, 171 (1989).

[7] K. D. Finkelstein, Q. Shen, and S. Shastri, Phys. Rev. Lett. **69**, 1612 (1992).

[8] D. H. Templeton and L. K. Templeton, Phys. Rev. B **49**, 14850 (1994).

[9] V. A. Belyakov and V. E. Dmitrienko, Uspekhi Fiz. Nauk. **158**, 679 (1989) [Sov. Phys. Usp. **32**, 697 (1989)].

[10] A. Kirfel and A. Petcov, Z. Kristallogr. **195**, 1 (1991).

[11] B. Dawson, in *Advances in Structure Research by Diffraction Methods*, Vol. 6, edited by W. Hoppe and R. Mason, Pergamon Press, Oxford, (1975), p. 1.

[12] T. Nagano, J. Kokubun, I. Yazawa *et al.*, J. Phys. Soc. Jpn. **65**, 3060 (1996).

[13] G. Dräger, R. Frahm, G. Materlik, and O. Brümmer, Phys. Status Solidi B **146**, 287 (1988).

[14] R. Colella, private communication (1999).

Electron spin resonance of copper pair centers in crystals with perovskite structure

D. V. Azamat,*) A. G. Badalyan, P. G. Baranov, P. P. Syrnikov, and V. A. Trepakov

A. F. Ioffe Physicotechnical Institute, Russian Academy of Sciences, 194021 St. Petersburg, Russia

J. Rosa and L. Jastrabik

Institute of Physics, Czech Academy of Sciences, 18040 Prague-8, Czech Republic

Copper pair centers, which could be of interest for obtaining quantitative information about exchange interactions in superconductors based on cuprate perovskites, are observed in crystals with the perovskite structure by the ESR method. Such centers are investigated in $KTaO_3$:Cu and $K_{1-x}Li_xTaO_3$:Cu crystals. A model consisting of a chain of two equivalent Cu^{2+} ions and three oxygen vacancies, extending along the $\langle 100 \rangle$ axis, is proposed for the centers. The exchange interaction in the pairs is ferromagnetic. © *1999 American Institute of Physics.* [S0021-3640(99)01112-3]

PACS numbers: 76.30.Fc

There are only relatively few works on the ESR of Cu^{2+} impurity centers in $KTaO_3$. Doubly charged copper ions were investigated by ESR in Ref. 1. During growth of the crystals, these ions substitute for Ta^{5+} in the octahedral position and form tetragonal centers; this has been shown by analysis of the hyperfine and superhyperfine interactions. The angular dependence of the ESR spectra of Cu^{2+} in the Q range were investigated in Ref. 2, and two types of axial Cu^{2+} centers were observed. The authors conjectured that the presence of two copper centers is due to the different positions of oxygen vacancies which are present in the crystal in order to neutralize the excess negative charge of tantalum (Ta^{5+}) sites occupied by copper ions. The presence of vacancies in the nearest-neighbor environment of Cu^{2+} ions can stabilize the static distortion caused by the Jahn–Teller effect, which occurs for the $3d^9$ configuration of the Cu^{2+} ions. For high impurity concentrations a substantial probability of copper ions occupying neighboring Ta^{5+} sites appears. The interaction between ions in such a pair should result in a completely new ESR spectra. Knowing the parameters of the spin Hamiltonian for single Cu^{2+} ions, one can determine the structure of pair centers. In the present work we observed $Cu^{2+}-Cu^{2+}$ pair centers in $KTaO_3$:Cu and $K_{1-x}Li_xTaO_3$:Cu crystals. An important reason for the interest in investigating such centers is that potassium tantalate crystals possess the perovskite structure, and copper centers in them can be model objects for investigating exchange interactions in cuprate superconductors.
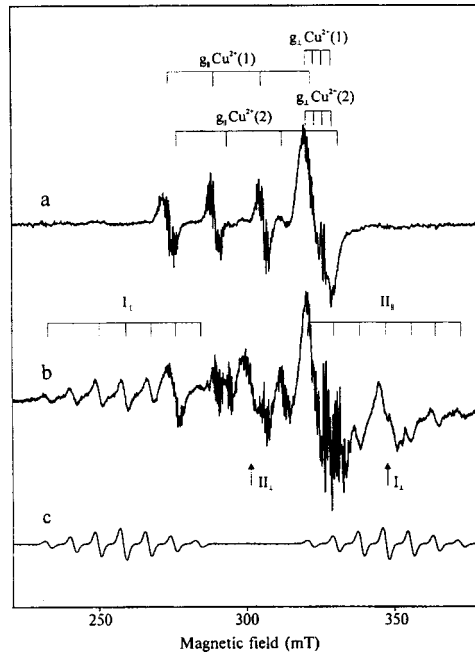
FIG. 1. ESR spectra of single Cu^{2+} (1) and Cu^{2+} (2) centers in a $KTaO_3$:Cu crystal (a) and $Cu^{2+}-Cu^{2+}$ pair centers in a $K_{1-x}Li_xTaO_3$:Cu crystal (b). The spectra were recorded at 300 K, $\nu=9.26$ GHz, and $B \parallel \langle 100 \rangle$. Simulated ESR spectrum of $Cu^{2+}-Cu^{2+}$ for $B \parallel z$ (c).

The experimental crystals were grown at the A. F. Ioffe Physicotechnical Institute. The $KTaO_3$:Cu and $K_{1-x}Li_xTaO_3$:Cu crystals were grown in a platinum crucible by spontaneous crystallization.[3] The copper concentration in the melting stock ranged from 0.05 to 0.5 mole %. The ESR spectra were recorded with a 3-cm range radio spectrometer. The angular dependences were measured by rotating the sample around the $\langle 100 \rangle$ and $\langle 110 \rangle$ crystallographic axes. A helium continuous-flow cryostat was used to investigate the temperature dependence of the ESR signal in the range 3.5–300 K.

SINGLE Cu^{2+} CENTERS

An ESR spectrum of single Cu^{2+} centers in a $KTaO_3$:Cu crystal is shown in Fig. 1a. The spectrum was recorded at 300 K and $B \parallel \langle 100 \rangle$. The figure shows lines corresponding to two types of axial Cu^{2+} centers with close parameters of the spin Hamiltonian. The tetragonal axes z of the centers are directed along $\langle 100 \rangle$. The same centers were also observed in a $K_{1-x}Li_xTaO_3$:Cu crystal (the lithium concentration in the melting stock was 3 mole %). The ESR spectra for Cu^{2+} centers of each type with $B \parallel z$ orientation consist of four hyperfine structure lines (the electron spin $S=1/2$, the nuclear spin $I=3/2$). For $B \perp z$ the lines of the hyperfine structure (HFS) are not resolved, and a single intense line is observed.

The spin Hamiltonian describing the angular dependence of the HFS of the ESR spectra has the form
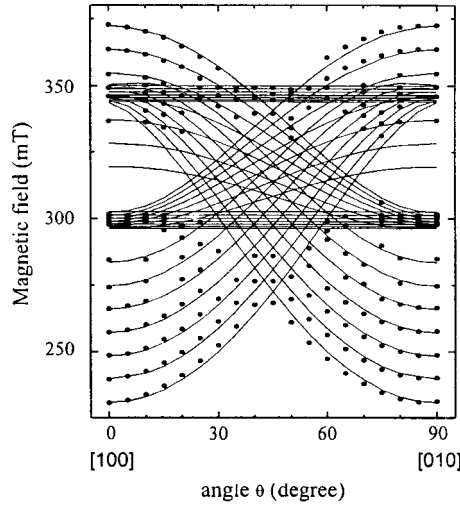
FIG. 2. Angular dependence of the ESR spectrum of Cu^{2+}–Cu^{2+} pair centers with the sample rotating around the $\langle 100 \rangle$ axis. Dots — experiment, lines — calculation using the Hamiltonian (3).

$$H = g_\parallel \mu_B B_z S_z + g_\perp \mu_B (B_x S_x + B_y S_y) + A_\parallel S_z I_z + A_\perp (S_x I_x + S_y I_y), \tag{1}$$

where μ_B is the Bohr magneton, $g_\parallel$ and $g_\perp$ are components of the g tensor, and $A_\parallel$ and $A_\perp$ are HFS constants. We obtained the following values for the parameters of the spin Hamiltonian for single Cu^{2+} (1) and Cu^{2+} (2) centers at 300 K: $g_\parallel(1) = 2.24$, $g_\parallel(2) = 2.20$, $g_\perp(1) = g_\perp(2) = 2.04$, $A_\parallel(1) = 173 \times 10^{-4}$ cm^{-1}, $A_\parallel(2) = 193 \times 10^{-4}$ cm^{-1}, and $A_\perp(1) = A_\perp(2) = 30 \times 10^{-4}$ cm^{-1}, which are close to the values obtained in Ref. 2. In the $B \parallel z$ orientation for each Cu^{2+} (1) and Cu^{2+} (2) center a well-resolved superhyperfine structure (SHFS) due to the hyperfine interaction with eight potassium ions is observed. The SHFS constants do not depend on the presence of lithium in the crystal, and for $B \parallel \langle 100 \rangle$ they are approximately 0.1 mT for Cu^{2+} (1) and 0.15 mT for Cu^{2+} (2). The intensity ratio between the Cu^{2+} (1) and Cu^{2+} (2) centers was different in samples with different copper concentration. In some samples predominantly centers of only one type are observed, while in other samples the concentration of both centers is comparable. Apparently, the Cu^{2+} (1) and Cu^{2+} (2) centers differ by the arrangement of the oxygen vacancies around them.

EXCHANGE COUPLED Cu²⁺–Cu²⁺ PAIRS

The ESR spectrum of a $K_{1-x}Li_xTaO_3$:Cu crystal with a high copper concentration is shown in Fig. 1b. Together with the spectra of single Cu^{2+} (1) and Cu^{2+} (2) ions, two groups of lines belonging to a new center, which are denoted as I and II are also seen. Each group contains seven HFS lines. The groups of lines $I_\parallel$, $II_\parallel$, and $I_\perp$, $II_\perp$ correspond to the z axis of a center being oriented parallel to and perpendicular to the magnetic field. The angular dependence of the groups of lines I and II (Fig. 2) is characteristic for a triplet center ($S = 1$) with axial symmetry and $g\mu_B B \gg D$.

Each group consists of seven HFS lines of width 2.6 ± 0.1 mT with intensities in the ratio 1:2:3:4:3:2:1, which indicates an interaction between an unpaired electron and two

equivalent nuclei with spin $I = 3/2$. The HFS constant in the spectrum of the new center is approximately equal to half the values of the HFS constants for Cu^{2+} (1) and Cu^{2+} (2) centers. All this indicates that the new ESR spectrum in Fig. 1b belongs to an exchange-coupled pair of Cu^{2+} ions occupying neighboring tantalum sites, the z axis of the center being directed along the $\langle 100 \rangle$ axis of the crystal. We simulated the ESR spectrum of a $Cu^{2+} - Cu^{2+}$ pair center for $B \parallel z$; this spectrum is presented in Fig. 1c. The agreement between the experimental and computed spectra is good.

The Hamiltonian of an exchange-coupled pair, including an isotropic exchange interaction of two spins $S_i = S_j = 1/2$ and the Zeeman interaction, has the form[5]

$$H = j\mathbf{S_i} \cdot \mathbf{S_j} + \frac{1}{2}\mu_B \mathbf{B} \cdot (\mathbf{g_i} + \mathbf{g_j}) \cdot (\mathbf{S_i} + \mathbf{S_j}) + \frac{1}{2}\mu_B \mathbf{B} \cdot (\mathbf{g_i} - \mathbf{g_j}) \cdot (\mathbf{S_i} - \mathbf{S_j}), \qquad (2)$$

where J is the isotropic exchange constant, μ_B is the Bohr magneton, and g_i and g_j are the g tensors of two ions in a pair. Since the isotropic exchange constant $J \gg (g_i + g_j)\mu_B B$, the two spins can form states with total spin 0 and 1. For an axial system with spin $\mathbf{S} = 1$ the ESR spectrum is described by the spin Hamiltonian

$$H = g_\parallel \mu_B B_z S_z + g_\perp \mu_B (B_x S_x + B_y S_y) + D_s\left[S_z^2 - \frac{1}{3}S(S+1) \right] + \mathbf{S} \cdot \mathbf{A} \cdot \mathbf{I}, \qquad (3)$$

where the first two terms are the Zeeman interaction, $g_\parallel = \frac{1}{2}[g_{1\parallel} + g_{2\parallel}]$ and $g_\perp = \frac{1}{2}[g_{1\perp} + g_{2\perp}]$, and the third terms describes the interaction due to the symmetric part of the anisotropic exchange and the magnetic dipole–dipole interaction.[5] The fourth term describes the hyperfine structure of the pair spectrum. This structure is related with the parameters of the hyperfine interaction for the two ions in a pair:

$$\mathbf{S} \cdot \mathbf{A} \cdot \mathbf{I} = \frac{1}{2}\mathbf{S} \cdot (\mathbf{A}_1 \cdot \mathbf{I}_1 + \mathbf{A}_2 \cdot \mathbf{I}_2), \quad I_1 = I_2 = \frac{3}{2}, \quad I = I_1 + I_2.$$

The computed and measured angular dependences of the ESR spectrum of the pair centers are presented in Fig. 2. Calculations of the angular dependence were performed using a program developed by Grachev.[4]

The parameters of the spin Hamiltonian for a $Cu^{2+} - Cu^{2+}$ center in a $K_{1-x}Li_xTaO_3$:Cu crystal at 300 K are: $|D_s| = 455 \times 10^{-4}$ cm^{-1}, $g_\parallel = 2.195$, $g_\perp = 2.04$, $A_\parallel = 90 \times 10^{-4}$ cm^{-1}, and $A_\perp \approx 10 \times 10^{-4}$ cm^{-1}. In the KTaO$_3$:Cu crystal $|D_s| = 420 \times 10^{-4}$ cm^{-1}, which is somewhat less than in $K_{1-x}Li_xTaO_3$:Cu.

Investigation of the temperature dependence of the ESR signal showed that as the temperature decreases to 3.5 K the amplitude of the signal from copper pair centers increases, although the signal saturates somewhat in the interval 10–3.5 K. This behavior indicates that the isotropic exchange is most likely ferromagnetic, i.e., the triplet spin state has a lower energy than the singlet state.

DISCUSSION OF THE RESULTS

The spectra of pair centers were observed in potassium tantalate crystals in a wide range of copper concentrations. Their relative intensity increases with the impurity concentration. It was noted that the observed spectrum is more intense in samples with close concentrations of Cu^{2+} (1) and Cu^{2+} (2) centers. The presence of a single vacancy in the
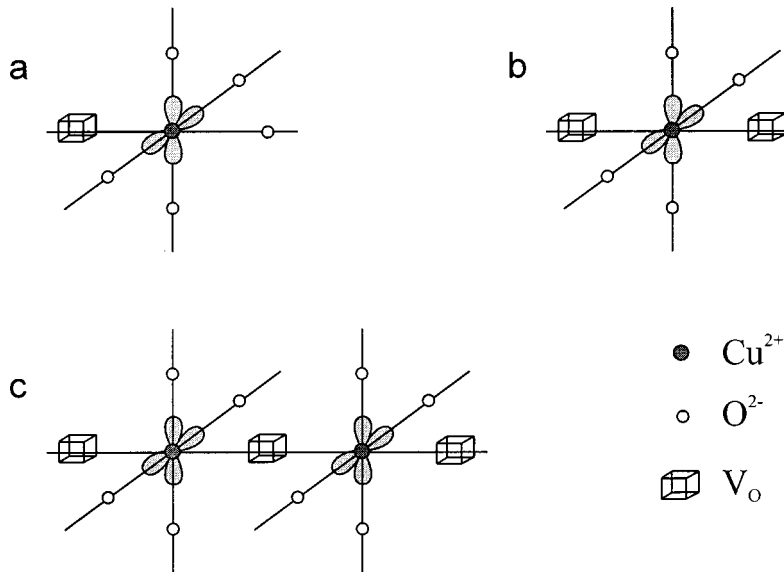
FIG. 3. Proposed models of single Cu^{2+} centers (a, b) and a $Cu^{2+}-Cu^{2+}$ pair center (c).

nearest-neighbor environment of Cu^{2+} (see Fig. 3a) is not sufficient for complete neutralization of the charge. Complete neutralization can be achieved in this case by the presence of an oxygen vacancy far enough from the site occupied by the Cu^{2+} ion that this can be observed in the ESR spectrum. At the same time, single Cu^{2+} centers can form with two nearest-neighbor vacancies lying along the $\langle 100 \rangle$ axis (Fig. 3b). In this case an excess positive charge appears. Two such centers Cu^{2+} (1) and Cu^{2+} (2) completely meet the condition of electrical neutrality, even if they are separated by a large distance. If the two Cu^{2+} ions occupy neighboring tantalum sites, then a pair center is formed. A model of such a center is shown in Fig. 3c. It consists of two single Cu^{2+} (1) and Cu^{2+} (2) centers, shown in Figs. 3a,b. Complete neutralization is attained. Since $g_{\parallel} > g_{\perp} > 2$, the Cu^{2+} ions are mainly in the (x^2-y^2) state. Therefore exchange coupling in a pair cannot occur via the p_z orbital of the oxygen ion; this also favors the proposed model.

The parameters obtained for the various interactions in copper pair centers could be of special interest for clarifying the nature of the interactions in high-T_c cuprate superconductors, which also possess the perovskite structure and have been observed[6] to exhibit magnetic resonance associated with copper clusters.

*⁾e-mail: D. Azamat@pop.ioffe.rssi.ru

[1] M. M. Abraham, L. A. Boatner, D. N. Olson, and U. T. Hoechli, J. Chem. Phys. **81**, 2528 (1984).
[2] I. P. Bykov, V. V. Laguta, M. D. Glinchuk *et al.*, Fiz. Tverd. Tela (Leningrad) **27**, 1908 (1985) [Sov. Phys. Solid State **27**, 1149 (1985)].

[3] V. A. Trepakov, M. Savinov, V. Vikhnin *et al.*, *Abstracts of the 8th Europhysics Conference on Defects in Insulating Materials*, Keele Staffs, 1998, p. 16; *Radiation Effects and Defects in Solids* (1999), in press.

[4] http://www.physik.uni-osnabrueck.de/resonanz/Grachev.

[5] J. Owen and E. A. Harris, in *Electron Paramagnetic Resonance*, edited by S. Geschwind (Plenum, New York, 1972), p. 427.

[6] P. G. Baranov and A. G. Badalyan, in *Phase Separation in Cuprate Superconductors*, edited by E. Sigmund and K. A. Mueller (Berlin, 1994), p. 118.

Translated by M. E. Alferieff

Colossal magnetoresistance of $Fe_xMn_{1-x}S$ magnetic semiconductors

G. A. Petrakovskiĭ,[*)] L. I. Ryabinkina, N. I. Kiselev, D. A. Velikanov, and A. F. Bovina

L. V. Kirenskiĭ Institute of Physics, Siberian Branch of the Russian Academy of Sciences, 660036 Krasnoyarsk, Russia

G. M. Abramova

Krasnoyarsk State University, 660041 Krasnoyarsk, Russia

The magnetic, electric, magnetoresistive, and structural properties are investigated in the sulfide solid solutions $Fe_xMn_{1-x}S$, which are based on the antiferromagnetic semiconductor α-MnS (the fcc NaCl lattice). Colossal negative magnetoresistance ($\delta_H \sim -83\%$ at 160 K for $x \sim 0.29$), comparable to that observed in La–Ca–Mn–O polycrystals and films ($\delta_H \sim -90\%$ at 100 K and 40 kOe), is observed in compounds with intermediate concentrations $0.26 < x < 0.4$, corresponding to the region of incipient ferromagnetism. © *1999 American Institute of Physics.* [S0021-3640(99)01212-8]

PACS numbers: 75.30.Vn, 75.50.Pp, 72.80.Ga

The compounds $Re_{1-x}Me_xMnO_3$ with perovskite structure, where Re are trivalent La, Pr, Y, Nd, and other ions, and Me are divalent Pb, Sr, Ca, and Ba ions, are under intensive investigation.[1] The interest in these materials is due to the observation of colossal magnetoresistance (CMR) in them under certain technological conditions and doping levels. The practical significance of this effect and the importance of studying its mechanism are stimulating the search for new compounds with CMR and the experimental investigation of the transport properties in materials of different structural types.

It is known[2] that manganese monosulfide α-MnS, similarly to $LaMnO_3$ (cubic perovskite structure), has a peculiar antiferromagnetic order with a characteristic ferromagnetic orientation of the spins in alternating planes and a lattice distortion wherein the cubic lattice is protracted along one of the diagonals of the cube.[2,3] In α-MnS, in contrast to $LaMnO_3$ ($T_s \sim 900$ K, $T_N \sim 140$ K), the structural transition temperature T_s is comparable to the Néel temperature ($T_N \sim 148$ K). The band structure and the nonactivational conductivity for high values of the resistivity ($\sim 10^8$ $\Omega \cdot$cm) at $T < T_N$ in α-MnS,[4] just as in $LaMnO_3$,[5] are characteristic for a band insulator. In the paramagnetic state $LaMnO_3$ and α-MnS are semiconductors. Just as in $LaMnO_3$-based systems,[1] concentration transitions from an antiferromagnetic semiconductor state into a ferromagnetic metallic state are produced in cation-substituted manganese sulfides $Me_xMn_{1-x}S$ as the dopant concen-

tration changes.[4,6] It is important to clarify the possibility of CMR in materials based on manganese monosulfide.

We report in the present letter the results of an investigation of the structural, electric, magnetic, and magnetoresistive properties of sulfide compounds of the system $Fe_xMn_{1-x}S$ synthesized on the basis of α-MnS.

Polycrystalline samples of $Fe_xMn_{1-x}S$ ($0 < x \leqslant 0.5$) were obtained from pure iron, manganese, and sulfur by the ampul method.[6,7] Investigations of the physical properties were performed as a function of concentration x, temperature T, and magnetic field H. The resistivity measurements were performed by the potentiometric method using dc current in a zero magnetic field and in transverse magnetic fields up to 10 kOe in the temperature range 77–300 K. A SQUID was used to measure the magnetic properties of the samples in the temperature range 4.2–300 K in fields up to 100 Oe. X-ray diffraction analysis (XDA) was performed with a DRON-2.0 diffractometer and monochromatized CuK_α radiation in the temperature range 77–300 K.

The XDA data showed the synthesized $Fe_xMn_{1-x}S$ samples at room temperature to be single-phase solid solutions with the fcc NaCl lattice that is characteristic for manganese monosulfide. As the degree x of cationic substitution increases, the cubic cell is compressed and the lattice parameter decreases from 5.222 Å ($x = 0$) to 5.165 Å ($x \sim 0.5$). Near the Néel temperature the $Fe_xMn_{1-x}S$ samples possess a structural distortion similar to the orthorhombic distortion of the lattice in α-MnS at $T_N = 148$ K.[3]

The SQUID data show that as the iron concentration in $Fe_xMn_{1-x}S$ increases, the antiferromagnetic transition temperature increases from 148 K ($x = 0$) to 196 K ($x = 0.25$). A concentration transition from an antiferromagnetic to a ferromagnetic state is observed in the concentration range $0.25 < x < 0.29$. The transition is accompanied by a sharp (two orders of magnitude) increase in the magnetic susceptibility from $\chi_{4.2\,K} = 8.56 \times 10^{-5}$ cm³/g ($x \sim 0.25$) to $\chi_{4.2\,K} = 2.43 \times 10^{-3}$ cm³/g ($x \sim 0.29$) (Fig. 1) and a field dependence of the magnetization that is characteristic of a ferromagnet.[6] The Curie temperature of the ferromagnetic samples is $T_C \sim 800$ K. As an illustration, the temperature dependence of the magnetization for the composition $x = 0.3$ is displayed in the inset in Fig. 1. Anomalous behavior of the susceptibility was observed in the experimental samples in weak fields ($H \sim 100$ Oe) at low temperatures ($T \sim 30$–40 K).

According to the resistivity measurements, the increase in the magnetic susceptibility of samples with $0.25 \leqslant x \leqslant 0.29$ due to the appearance of ferromagnetic order is accompanied by a decrease in the resistivity measured in a zero magnetic field. For example, $\rho_{77\,K} = 49.5 \times 10^6$ $\Omega \cdot$cm for samples with $x \sim 0.25$, while $\rho_{77\,K} = 32.1 \times 10^2$ $\Omega \cdot$cm for $x \sim 0.29$. As x is increased further, a semiconductor–semimetal concentration transition is observed (Fig. 2), and $\rho_{77\,K} = 8.88$ $\Omega \cdot$cm for $x = 0.4$.

Investigations of the magnetoresistive properties established that samples with $x \leqslant 0.25$, being antiferromagnetic semiconductors, and do not show a strong magnetic field dependence of the resistivity in the temperature range 77–300 K in magnetic fields up to 10 kOe.

In $Fe_xMn_{1-x}S$ samples with intermediate concentration $0.25 < x < 0.4$ the temperature dependence and the magnitude and sign of the magnetoresistance were found to depend on the magnetic field. It is seen in Fig. 3a, which shows the temperature dependence of the magnetoresistance in fields of 5 and 10 kOe for composition $x \sim 0.29$, that
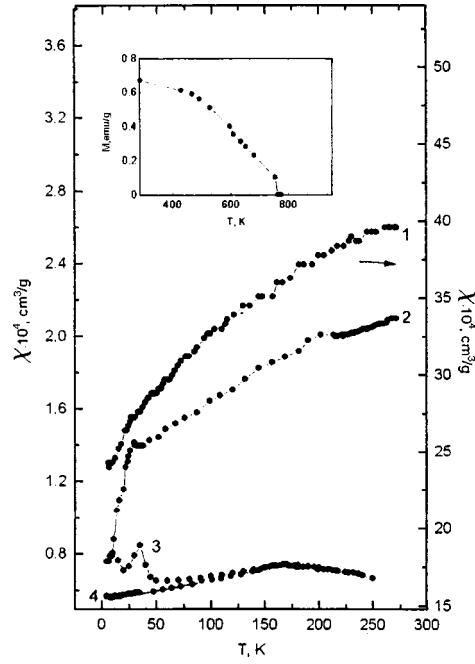
FIG. 1. Temperature dependences of the magnetic susceptibility of the sulfides $Fe_xMn_{1-x}S$ in the range 4.2–300 K for compositions x: 0.29 (*1*), 0.25 (*2*), 0.05 (*3*), and 0 (*4*). Inset: Temperature dependence of the magnetization of $Fe_xMn_{1-x}S$ with $x \sim 0.3$ in the temperature range 300–800 K in a field $H = 700$ Oe.
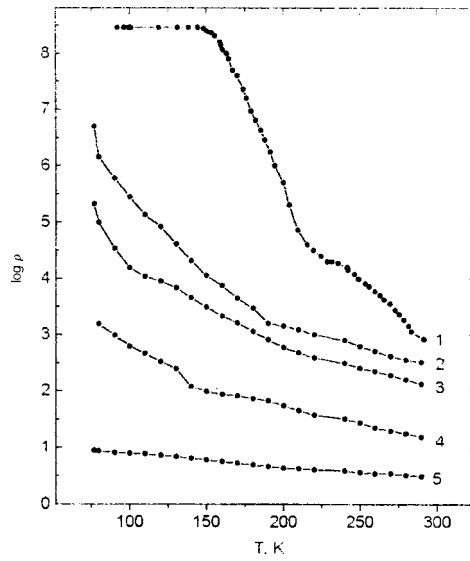

FIG. 2. Temperature dependences of the resistivity of the sulfides $Fe_xMn_{1-x}S$ for compositions $x = 0$ (*1*), 0.15 (*2*), 0.25 (*3*), 0.29 (*4*), and 0.4 (*5*).
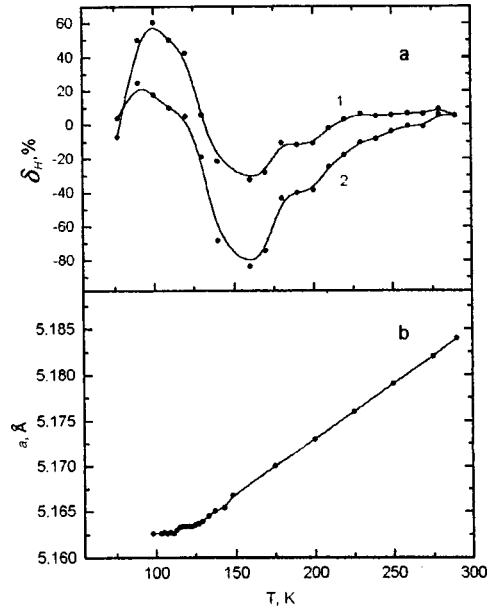
FIG. 3. Temperature dependence of the magnetoresistance δ_H (a) and lattice parameter (b) for $Fe_xMn_{1-x}S$ ($x \sim 0.29$); $H = 5$ kOe (*1*) and 10 kOe (*2*).

the negative CMR increases with decreasing temperature and reaches a maximum (for given temperature and field ranges) value $\delta_H = (\rho_H - \rho_0)/\rho_H = -83\%$ at $T \sim 160$ K in a 10 kOe field. Below ~ 150 K, in the region of the structural distortion (Fig. 3b), the magnetoresistance becomes positive and δ_H reaches $\sim 60\%$ at 90 K in a 5 kOe field and 20% in a 10 kOe field. As temperature decreases further, the positive magnetoresistance decreases, and δ_H once again becomes negative near liquid-nitrogen temperature.

As the iron concentration x increases, the negative magnetoresistance decreases, and $\delta_H = -40\%$ for $x \sim 0.3$ at 77 K in a 10 kOe field. In ferromagnetic samples with $x \geqslant 0.4$, corresponding to the semiconductor–semimetal concentration transition range, the negative magnetoresistance does not exceed 10%.

In summary, the results presented above attest to the presence of the CMR effect in materials based on manganese monosulfide.

In Nagaev's paper[1] it is conjectured that the CMR mechanism in lanthanides is due to the formation of the magnetically two-phase state and attendant electronic stratification with preservation of a homogeneous crystal lattice.

All of the currently available experimental results on the physical properties of the sulfides $Fe_xMn_{1-x}S$, specifically, calculations of the magnetic phase diagram, measurements of the magnetization in weak (up to 100 Oe) and strong (up to 20 kOe) fields,[6] and Mössbauer investigations[8] suggest that a possible mechanism for CMR in the magnetic semiconductors $Fe_xMn_{1-x}S$ could be magnetic and electronic phase separation. A characteristic feature of the sulfide compounds $Fe_xMn_{1-x}S$ investigated in the present work is their two-phase nature over a wide temperature range (at least in the range 77–300 K). According to Mössbauer data,[8] the ferromagnetic samples with $x \geqslant 0.3$ at room tempera-

ture consist of a collection of paramagnetic and ferromagnetic phases, and at 77 K the samples consist of two magnetically ordered phases. It can be concluded on the basis of these data that as the temperature decreases, the paramagnetic part of the material passes into a magnetically ordered state. One can see from Fig. 3 that the negative CMR increases with decreasing temperature (in the range 150–300 K). Since the magnetic state of the samples changes with decreasing temperature, it can be inferred that for effective magnetic and electronic percolation to appear a definite ratio of the volumes of the magnetic phases for a given magnetic field is required. The change in sign of the magnetoresistance at $T < 150$ K is probably due to changes in the crystal lattice, since a structural distortion is observed in this temperature range.

In summary, new compounds $Fe_xMn_{1-x}S$ which have a colossal negative magnetoresistance and crystallize in the cubic NaCl structure have been found. The observed behavior of the magnetic and electric properties of the compounds $Fe_xMn_{1-x}S$ shows that it would be promising to study materials based on manganese monosulfide.

*)e-mail: gap@cc.krascience.rssi.ru

[1] É. L. Nagaev, Usp. Fiz. Nauk **166**, 833 (1996).

[2] J. Goodenough, *Magnetism and the Chemical Bond* (Interscience, New York, 1963) [Russian original, Metallurgiya, Moscow, 1968].

[3] H. H. Heikens, G. A. Wiegers, and C. F. van Bruggen, Solid State Commun. **24**, 205 (1977).

[4] G. V. Loseva, S. G. Ovchinnikov, and L. I. Ryabinkina, Fiz. Tverd. Tela (Leningrad) **28**, 2048 (1986) [Sov. Phys. Solid State **28**, 1145 (1986)].

[5] L. P. Gor'kov, Usp. Fiz. Nauk **168**, 665 (1998).

[6] G. A. Petrakovskiĭ, S. S. Aplesnin, G. V. Loseva *et al.*, Fiz. Tverd. Tela (Leningrad) **33**, 406 (1991) [Sov. Phys. Solid State **33**, 233 (1991)].

[7] G. A. Petrakovskii, G. V. Loseva, L. I. Ryabinkina, and S. S. Aplesnin, J. Magn. Magn. Mater. **140−144**, 146 (1995).

[8] G. V. Loseva, L. I. Ryabinkina, S. G. Ovchinnikov, and O. A. Bayukov, Fiz. Tverd. Tela (Leningrad) **25**, 3717 (1983) [Sov. Phys. Solid State **25**, 2142 (1983)].

Translated by M. E. Alferieff

Fractal–percolation model of the stability of foam

Yu. V. Pakharukov*) and T. E. Shevnina

Tyumen State Oil and Gas University, 625000 Tyumen, Russia

A fractal–percolation model describing the stability of foam is studied. In this model, a correspondence is established between the system of branched channels and a fractal tree. In the proposed model, the foam breaks down by a scale-invariant load-transfer mechanism. A formula is obtained for calculating the height of the nth level of the fractal tree. The critical height of a foam column is determined. The results are compared with experimental data. © *1999 American Institute of Physics.* [S0021-3640(99)01312-2]

PACS numbers: 82.70.Rr, 47.53.+n, 64.60.Ak

The investigation of gas–liquid foams as dynamic media with a finite number of degrees of freedom is of great practical value. Despite this, a theoretical model that satisfactorily describes all properties of foams is still lacking. We believe that such a model should based on parameters that reflect the structure of foams.

In the present letter we consider a fractal–percolation model describing the stability of a foam. The model is based on the polyhedral model,[1] in which polyhedral bubbles are separated by thin films, channels, and nodes, the volume of liquid at the nodes being negligibly small. In the proposed model a correspondence is established between a system of branched channels and a fractal tree,[2] where two edges (the junctions of films), making an angle $\theta = 120°$, leave each vertex (node). At the nth level there are 2^n edges connecting each vertex of order $n-1$ with two vertices of order n. The height at the nth level is $h_n = h_1/2^{n-1}$, and the height of the entire tree will be

$$H = \sum_{n=1}^{\infty} h_n = 2h_1 .$$

The average load on each edge at the nth level is $P_n = P\cos(\theta/2)/2^n$, where P is the vertical load applied to the level $n=0$.

The breakdown of foam is ordinarily attributed to the outflow of liquid in a process consisting of percolation along random nodes. The geometry of the fractal tree fixes the average number of nodes per unit volume. Therefore the breakdown of the foam will coincide with the probability $\rho^{(b)}$ of an infinite number of nodes being wetted in a percolation problem.[3,4] The probability $\rho^{(b)}$ is obtained from the probability $\rho_n^{(b)}$ of wetting of at least n nodes by passing to the limit $\rho^{(b)} = \lim_{n\to\infty} \rho_n^{(b)}$. The probability $\rho_n^{(b)}$ can be determined by calculating the fraction of the volume falling within a sphere of radius $h/2$ at the percolation threshold.
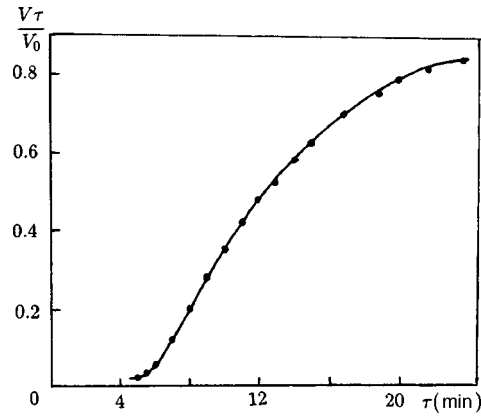
FIG. 1. Curve of fluid outflow from a foam column.[1]

The breakdown of foam in the proposed model develops by a scale-invariant load-transfer mechanism: If liquid breaks through the nth node, then the applied load is transferred to the neighboring node at the $(n-1)$th level. This makes it possible to obtain a recurrence relation for the probability of breakdown of the foam by analogy to the distribution of the load over a fractal tree:

$$\rho_{n-1} = 2\rho_n[1-(1-\rho_n)^{2m}] - \rho_n^2, \tag{1}$$

where m is the order of the distribution. The result is an S-shaped dependence characteristic for percolation processes. An experimental curve describing outflow of liquid from foam has been obtained in Ref. 1 (Fig. 1). As one can see, this curve is indeed S-shaped. The results of the model and the experimental data of Ref. 1 permit determining the critical pressures at which the breakdown process develops:

$$P_c = \left[\frac{\ln 2}{2^2-1}\right]^{1/2} P_{0n} = 0.48 P_{0n}. \tag{2}$$

Here P_{0n} is the load on the edge at the nth level and equals

$$P_{0n} = P_b - \frac{K_1 \sigma}{2.5 r_0 \sqrt{\gamma}}, \tag{3}$$

where $P_b = 2\sigma/r_0$ is the gas pressure in an adjoining bubble, r_0 is the radius of an equivalent bubble, σ is the surface tension, K_1 is a coefficient determined by the model of the foam structure (for the pentagon–dodecahedron model $K_1 = 1.53$), and γ is the volume density of the foam.

The process of redistribution of liquid in foams (syneresis) has been widely studied in a number of works.[1,5–7] It has been shown that the onset time τ_n of fluid outflow can depend on the height of the foam column only up to a definite value (Fig. 2). There is still no satisfactory theoretical explanation for this experimental result. Figure 3 shows the same experimental results, but they are plotted differently. The probability of onset of
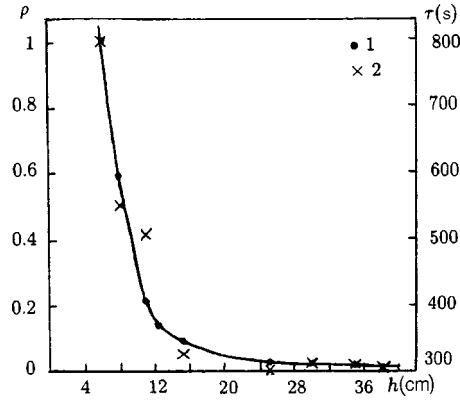
FIG. 2. Probability of breakdown (●) and onset time of fluid outflow (×) versus the height of the foam column.

fluid outflow $\rho \sim \tau_0 / \tau_n$ is studied as a function of the height of the foam column (τ_0 is the time determining the moment of outflow of the liquid irrespective of the height of the foam column). The plot is of a clearly percolation nature:[3,4]

$$\rho \sim (P - P_c(h))^\beta, \tag{4}$$

where P is the pressure in the foam channel, $P_c(h)$ is the critical pressure (percolation threshold), and β is the percolation critical exponent.

We shall determine the percolation threshold h_c for a loaded fractal tree. If the degree of dispersion remains constant in the entire volume of the foam, then the radius r_0 of the bubbles and the gas pressure P_b in them are constant and are independent of the coordinate z (we assume that the z axis is directed vertically upwards). Let the liquid in the foam channels at the level n be stationary. That is, hydrostatic equilibrium determined by the condition
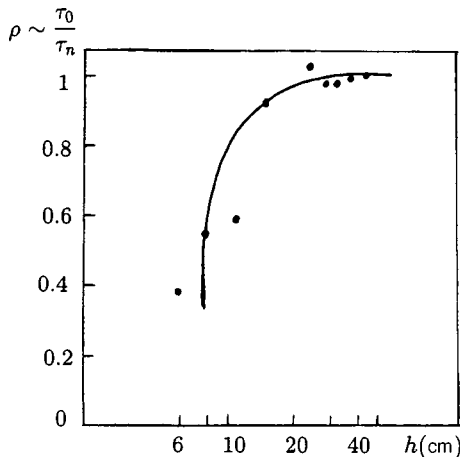

FIG. 3. Onset probability of fluid outflow versus the height of the foam column on a semilogarithmic scale.

$$\partial P_{0n}/\partial z + \rho g = 0, \tag{5}$$

where ρ is the density of the liquid, has been established. Substituting expression (3) into Eq. (5), we obtain the differential equation

$$\frac{K_1 \sigma}{5 r_0 \gamma^{3/2}} \frac{\partial \gamma}{\partial z} + \rho g = 0, \tag{6}$$

whose solution is the dependence of the volume density of the foam on the height of the nth level:

$$\gamma_n = \left(\frac{1}{\sqrt{\gamma_{n+1}}} - \frac{\rho g h_n \cdot 2.5 r_0}{K_1 \sigma} \right)^{-2}, \tag{7}$$

where γ_{n+1} is the volume density at the $(n+1)$th level.

Expressions for calculating the pressure in a foam channel at the nth level and the height of the nth level can be obtained from the condition (7) using Eq. (3):

$$P_{0n} = P_b - \frac{K_1 \sigma}{2.5 r_0} \left[\frac{1}{\sqrt{\gamma_{n+1}}} - \frac{\rho g h_n \cdot 2.5 r_0}{K_1 \sigma} \right], \tag{8}$$

$$h_n = \frac{K_1 \sigma}{2.5 r_0 \rho g} \frac{1}{\sqrt{\gamma_{n+1}}} - \frac{1}{\rho g} [P_b - P_{0n}]. \tag{9}$$

Let us assume that the applied load on the edge at the nth level equals the critical load:

$$P_c = \frac{P \cos(\Theta/2)}{2^n}. \tag{10}$$

Using expressions (2) and (10), we can write the pressure P_{0n} in the form

$$P_{0n} = \frac{P \cos(\theta/2)}{0.48 \cdot 2^n}, \quad P = 2 \frac{\sigma}{r_0}. \tag{11}$$

This makes it possible to obtain a formula for calculating the height of the nth level:

$$h_n = \frac{K_1 \sigma}{2.5 r_0 \rho g} \frac{1}{\sqrt{\gamma_{n+1}}} - \frac{2\sigma}{\rho g r_0} \left[1 - \frac{\cos(\theta/2)}{0.48 \cdot 2^n} \right]. \tag{12}$$

We shall now estimate the critical height of a foam column, taking into account that the total height of a loaded fractal tree is

$$H = \sum_{n=1}^{\infty} h_n = 2 h_1.$$

For foam with $r_0 = 2 \times 10^{-4}$ m, $\rho = 10^3$ kg/m^3, $g = 9.8$ m/s^2, $K_1 = 1.53$, $\theta = 120°$, and average multiplicity $K = 1/\gamma = 70$, the height of the first level is $h_1 = 0.064$ m. Then the critical height of the foam column is $H = 0.128$ m. This result agrees well with the experimental data (Fig. 3).

In summary, the fractal–percolation model gives an adequate description of the redistribution of liquid in foam and explains the existence of a critical height as a percolation threshold.

*⁾e-mail: pakharukov@mailcity.com

[1] K. B. Kann, *Capillary Hydrodynamics of Foams* [in Russian] (Nauka, Novosibirsk, 1989).

[2] S. Solla, in *Fractals in Physics*, edited by L. Pietronero and E. Tosatti (North-Holland, Amsterdam, 1986) [Russian translation, Mir, Moscow, 1988, p. 255].

[3] E. Feder, *Fractals* (Plenum Press, New York, 1988) [Russian translation, Mir, Moscow, 1991].

[4] B. I. Shklovskiĭ and A. L. Éfros, *Electronic Properties of Doped Semiconductors* (Springer-Verlag, New York, 1984) [Russian original, Nauka, Moscow, 1979].

[5] A. G. Vetoshkin, Teor. Osnovy Khim. Tekhnol. **29**, 463 (1995).

[6] E. I. Vasil'ev, S. Yu. Mitichkin, V. G. Testov *et al.*, Zh. Tekh. Fiz. **76**(11), 1 (1997) [Tech. Phys. **42**, 1241 (1997)].

[7] V. A. Kulikovskiĭ, S. Yu. Mitichkin, V. G. Testov *et al.*, Zh. Tekh. Fiz. **66**(12), 1 (1996) [Tech. Phys. **41**, 1199 (1996)].

Translated by M. E. Alferieff